

ABSTRACT

Title of Dissertation: ACTIVE CONTROL OF SOUND TRANSMISSION
INTO THREE-DIMENSIONAL ENCLOSURES

Moustafa Al-Bassyiouni, Doctor of Philosophy, 2004

Dissertation directed by: Professor B. Balachandran
Department of Mechanical Engineering

The aim of this dissertation work is to understand active control of sound fields inside a three-dimensional rectangular enclosure into which noise is transmitted through a flexible boundary. To this end, analytical and numerical studies have been conducted. In the modeling efforts, a spherical wave excitation, which is generated by a noise source located in the near field of the flexible panel, is considered. Piezoelectric patches, which are bonded symmetrically to the top and bottom surfaces of the panel, are used as actuators. Microphones located inside and outside the enclosure serve as pressure sensors. The efforts account for panel interactions with both the external sound field and the enclosed sound field, and this feature makes it appealing for model-based active control schemes.

The feasibility of implementing two *zero spillover schemes* for active structural-acoustic control systems has been studied through analysis and experiments. These schemes have

been developed to ensure that spillover does not occur outside the control bandwidth. The numerical results are found to be in good agreement with the corresponding experimental observations; attenuations ranging up to 18.1 dB are experimentally obtained for narrowband disturbances and an attenuation of 8.3 dB is obtained for broadband excitation in the frequency range of $40 \text{ Hz} \leq f \leq 230 \text{ Hz}$.

The following contributions have resulted from this work: i) an analytical model capable of predicting the external pressure fields due to both the noise source and structural-acoustic interactions and that accounts for the general case of spherical wave propagation, ii) development of zero spillover, active structural-acoustic control schemes for controlling three-dimensional sound fields, and iii) a new *relaxed zero spillover control scheme* to ensure that the controlled response is bounded over the entire frequency range.

**ACTIVE CONTROL OF SOUND TRANSMISSION INTO
THREE-DIMENSIONAL ENCLOSURES**

By

Moustafa Al-Bassyiouni

Dissertation submitted to the Faculty of the Graduate School of the
University of Maryland, Collage Park in partial fulfillment
of the requirements for the degree of
Doctor of Philosophy
2004

Advisory Committee

Professor B. Balachandran, Mechanical Engineering, Chairman/Advisor
Professor A. Baz, Mechanical Engineering
Professor I. Chopra, Aerospace Engineering
Assistant Professor D. Robbins, Mechanical Engineering
Associate Professor N. Wereley, Aerospace Engineering

© Copyright by
Moustafa Al-Bassyouni
2004

DEDICATION

To my parents, my wife, and my children

ACKNOWLEDGEMENTS

First of all, I would like to thank ALLAH, who has given the knowledge and the ability to observe, think, and develop. All praise and thanks are due to Him.

I am grateful to my advisor, Professor Balakumar Balachandran, for the continuous support and encouragement that he provided during my research and study at the University of Maryland. To mention the least of his supporting efforts, Professor Balachandran has offered me research and teaching opportunities and opportunities to participate in conferences, among many other valuable things that constantly enhanced my academic and research qualifications. His insightful guidance and advice that he has given me were not only of great significance during my doctoral work, but it will also help me in my future career.

My appreciation goes also to my doctoral committee members: Professor Baz, Professor Chopra, Professor Robbins, and Professor Wereley. I thank them for their guidance, teaching, and assistance they provided when I sought them, as well as for their willingness to serve on my committee. My special thanks are to Professor Baz for introducing me to the program at the University of Maryland. I also thank Professor Darryll Pines for the many suggestions he provided throughout the course of this work.

I would like to extend my sincere thanks to Professor Sayed Dosouki; Cairo University, because of whom I loved the science of Control Systems. I will never forget his genuine efforts during my undergraduate study and Masters work.

Last but not the least, I am forever indebted to my parents. Their love, dedication, and help were always the foundation of my work and patience during this long course of learning. I also want to express my thanks to my wife for her endless understanding, patience, and support when it was most needed. My special thanks to my children, who suffered from not having much time and fun with their dad, especially during the last stage of the doctoral work.

Partial support received for this work from the U.S. Army Research Office (ARO) through Contract No. DAAH 049610334 is gratefully acknowledged. Drs. Tom Doligalski and Gary Anderson were the technical monitors for the ARO contract.

TABLE OF CONTENTS

LIST OF TABLES	viii
LIST OF FIGURES.....	ix
1. Introduction and Background.....	1
1.1. Previous Work.....	3
1.2. Objectives and Scope of Dissertation Work	9
1.3. Organization of Dissertation	9
2. Experimental Arrangement	11
3. System Modeling.....	18
3.1. Analytical Model.....	19
3.1.1. Panel-Enclosure System.....	21
3.1.2. Piezoelectric Actuator-Panel System	26
3.1.3. Integrated Piezo-Panel-Enclosure System	37
3.1.4. Panel-External Sound Field System.....	45
3.1.5. Equations of the Complete System	48
3.1.6. Numerical Results	52
3.2. Experimentally Identified Model	64

TABLE OF CONTENTS

3.3.	Limitations of Analytical and Experimentally Identified Models	66
3.4.	Comparisons with Experimental Results	71
4.	Control Approaches.....	80
5.	Control Design and Implementation: PQZ Controller	85
5.1.	PQZ Control Design.....	85
5.2.	PQZ Controller Justifications.....	80
5.2.1.	Analysis of Inherent Acoustic Feedback.....	92
5.2.2.	Analysis of Stability and Performance.....	96
5.3.	Experimental Implementation of Control Scheme.....	100
5.4.	Simulation and Experimental Results	111
5.4.1.	Experimentally Identified Model Based PQZ Controller	111
5.4.2.	Analytical Model Based PQZ Controller	115
6.	Control Design and Implementation: RZS Controller	125
6.1.	RZS Control Design.....	125
6.2.	Simulation and Experimental Results	127
6.3.	Sensitivity Analysis.....	132
7.	Conclusions and Suggestions for Future Work.....	134
	Appendix I. Numerical Values of Constants, Parameters, and Dimensions	138
	Appendix II. Numerical Results.....	140
	Appendix III. Frequency-Response Function Comparisons	144

TABLE OF CONTENTS

Appendix IV. Entries of F_a 148

Appendix V. Experimental Results of PZT strain..... 158

Appendix VI. Matlab Program Codes..... 161

References 169

LIST OF TABLES

Table 2.1. Small signal PZT 5H characteristics [Morgan Electro Ceramics].	14
Table 2.2. Characteristics of different microphones used in the experimental setup.....	15
Table 3.1. Values of the constants $\lambda_1(i)$ and $\lambda_2(i)$ used in equation (3.42) [Blevins, 1979].	37
Table 3.2. Coefficients in approximate formulae for clamped rectangular plate [Blevins, 1979].....	53
Table 3.3. Numerical predictions of the first few undamped natural frequencies (in Hz) of the panel and enclosure in the uncoupled and coupled cases.....	58
Table 3.4. Percentage values of the measured capacitance constants of the PZT pairs relative to the nominal value.	68
Table 3.5. First few structural and acoustic resonance frequencies (in Hz): Comparisons of the numerical predictions with the experimental data.	77
Table 5.1. Characteristics of near-collocated microphones.	100
Table V.1. Applied Positive (DC) Voltage and PZT free strain: Analytical predictions and experimental measurements.	159
Table V.2. Applied Negative (DC) Voltage and PZT free strain: Analytical predictions and experimental measurements.	160

LIST OF FIGURES

Figure 1.1. Adapted figures from Lueg’s patent; United States Patent and Trademark Office, http://www.uspto.gov	4
Figure 2.1. Photograph of the experimental arrangement; setup located in Vibrations Laboratory.	12
Figure 2.2. Experimental setup: (a) locations of structural actuators and sensors on the flexible panel and (b) panel-PZT patch geometry, electrical wiring, and principal axes for a PZT patch.....	13
Figure 2.3. Locations of microphones inside the enclosure.....	13
Figure 2.4. Photograph of the dSPACE interface system connected to a PIII-450 MHz PC; setup located in Vibrations Laboratory.	15
Figure 2.5. Schematic of the experimental setup, showing all the external peripherals and their interconnections with the different elements of the experiment.....	16
Figure 3.1. Schematic of the panel-enclosure system used for the analytical model.....	20
Figure 3.2. Schematic showing the locations of the noise source and the observation point with respect to the flexible panel.....	46
Figure 3.3. Numerical predictions of the first six mode shapes of the flexible panel.....	54
Figure 3.4. Numerical predictions of the first four acoustic mode shapes of the enclosure.	55
Figure 3.5. Percentage differences in resonance frequencies among the uncoupled and coupled cases.....	57

LIST OF FIGURES

Figure 3.6. Comparisons between the 8th order Padé approximation of Eq. (3.86) (straight line) and the numerical results of $C_i^{(op)}$, which are calculated for odd×odd modes with the first 17 vibrations modes; the numerical results are normalized to have an average magnitude of unity (dotted line). 62

Figure 3.7. Overall system block diagram. 63

Figure 3.8. Photograph of the loudspeaker-panel-enclosure arrangement showing the various transfer functions. 65

Figure 3.9. Measurements of capacitance constants for the PZT pairs as percentages of the nominal value. Each pair is defined by its x and y indices; e.g., A1, B2, etc..... 67

Figure 3.10. A PZT actuator patch with a strain gage used in the experiments..... 69

Figure 3.11. Analytical predictions and experimental measurements for the PZT-5H free strain. 69

Figure 3.12. Frequency-response plot of the transfer function $G_{Mic1,A2}$ 70

Figure 3.13. Frequency-response plot of the transfer function $G_{Mic3,A2}$ 72

Figure 3.14. Frequency-response plot of the transfer function $G_{Mic3,A2}$ 73

Figure 3.15. Frequency-response plot of the transfer function $G_{Mic1,B2}$ 74

Figure 3.16. Frequency-response plot of the transfer function $G_{RefMic,B2}$ 75

Figure 3.17. Frequency-response plot of the transfer function G_{Mic1,a_s} 75

Figure 3.18. Frequency-response plot of the transfer function G_{Mic3,a_s} 76

Figure 3.19. Transfer function G_{Mic3,a_s} : Comparison of the analytical plane-wave model result (continuous lines) with experimental data (dotted lines). 78

Figure 3.20. Transfer function G_{Mic2,a_s} : Model result from spherical wave analysis (continuous lines) versus model result from plane wave analysis (dotted lines). 78

LIST OF FIGURES

Figure 3.21. Experimental identification of the transfer function between the PZT patch B2 and the reference microphone..... 79

Figure 4.1. Typical ANC block diagram..... 83

Figure 5.1. Simplified ANC block diagram where inherent feedback is zero (or negligible)..... 87

Figure 5.2. Block diagram for ASAC system with near-located microphone while the IAF is neglected. 88

Figure 5.3. Simplified block diagram of ASAC system with near located microphone. 88

Figure 5.4. Reconstructed zero spillover controller for ASAC system..... 90

Figure 5.5. (a) Reconstructed zero spillover controller for ASAC system for stability and performance analysis and (b) simplified version. 96

Figure 5.6. Performance test: Graphical representation of Eq. (5.25). 99

Figure 5.7. Photograph showing near-located microphones. 100

Figure 5.8. Experimental identification of the transfer function G_{MU} 101

Figure 5.9. Sound pressure level measured at the located microphone when individually excited by noise source and piezo patch. 102

Figure 5.10. Photograph showing the reference microphone in horizontal and vertical arrangements. 103

Figure 5.11. Amplitude of the pressure component $Y_1(\omega)$: (a) vertical versus horizontal orientations and (b) magnitude difference. 104

Figure 5.12. Amplitude of the pressure component $Y_2(\omega)$: (a) vertical versus horizontal orientations and (b) magnitude difference. 105

LIST OF FIGURES

Figure 5.13. Amplitudes of the pressure components $Y_1(\omega)$ and $Y_2(\omega)$ measured at the reference microphone when individually excited by the noise source and piezo patch. 106

Figure 5.14. Magnitude of the PQZ controller frequency-response function along with the magnitudes determined from Eqs. (5.11) and (5.21). The bounds given by (5.11) and (5.21) are shown by broken lines. 107

Figure 5.15. Acoustical path from the noise source to collocated microphone: G_{MW} versus G_{MY} G_{YW} 108

Figure 5.16. Acoustical path from noise source to error microphone: G_{ZW} versus G_{ZM} G_{MY} G_{YW} 109

Figure 5.17. Performance test for different values of ξ (first argument) and δ (second argument). 109

Figure 5.18. Simulation diagram used to simulate the loudspeaker-panel-enclosure model. 110

Figure 5.19. Simulation results: Pressure response at the error microphone Mic.1 obtained through simulations in the uncontrolled and controlled cases. In case (a), inherent feedback is neglected, and in case (b), this feedback is considered. 111

Figure 5.20. Simulation results: Differences between the pressure responses in the uncontrolled and controlled cases, at the error microphone location. 112

Figure 5.21. Experimental results: Pressure response, at the error microphone (Mic.1) location, measured experimentally in uncontrolled and controlled cases. Non-acoustic sensor was used as reference sensor. 113

Figure 5.22. Experimental results: Differences between the pressure responses in the uncontrolled and controlled cases at the error microphone (Mic.1) location. 114

Figure 5.23. Control voltage inputs to the PZT pair B2 at different frequencies. 115

LIST OF FIGURES

Figure 5.24. Simulation results for magnitudes of frequency-response functions in uncontrolled and controlled cases: (a) noise source, error microphone Mic.1, (b) noise source, performance microphone Mic.2, and (c) noise source, performance microphone Mic.3. 116

Figure 5.25. Simulation results for pressure attenuation inside the enclosure: (a) broadband excitation, (b) tonal excitation at modal frequency of (1,1) mode, (c) tonal excitation at modal frequency of (3,1) mode, and (d) tonal excitation at modal frequency of (1,3) mode. 117

Figure 5.26. Tonal excitation: (a) SPL at error microphone (Mic.1) location measured in uncontrolled and controlled cases and (b) SPL difference. 118

Figure 5.27. White noise excitation: (a) SPL at error microphone (Mic.1) location measured in uncontrolled and controlled cases and (b) SPL difference. 120

Figure 5.28. White noise excitation: SPL difference between the uncontrolled and controlled cases (a) at the performance microphone (Mic. 2) and (b) at the performance microphone (Mic.3). 122

Figure 5.29. Difference between PZT patch strains in the uncontrolled and controlled cases for white noise excitation: (a) PZT patch A1 and (b) PZT patch B3. 124

Figure 6.1. Representation of the control domain D_c 127

Figure 6.2. Frequency response and pole zero map of RZSC. 128

Figure 6.3. Comparison of frequency responses from the controlled and uncontrolled cases. Identified transfer functions are used. 129

Figure 6.4. Sound pressure levels at the microphone Mic.1 location in uncontrolled (dotted line) and controlled (continuous line) cases. 130

Figure 6.5. Control voltage signal fed to the PZT pair B2. 131

LIST OF FIGURES

Figure 6.6. Changes in noise attenuation at the fundamental frequency with variations in ξ / δ 132

Figure 6.7. Changes in noise attenuation at the fundamental frequency with variations in phase delay..... 132

1. Introduction and Background

Control of noise and vibration is important for many civil, industrial, and defense applications. The specific problem of controlling interior noise levels in enclosures has received considerable interest in the engineering research community, since there are numerous examples of inhabited vehicles that combine actuation and transmission units within enclosed spaces, such as automobiles, aircraft, and spacecraft. The noise control problem has been broadly attacked by two different control techniques — passive-control and active-control techniques. Passive-control techniques typically include reactive devices, such as Helmholtz resonators, and dissipative devices, such as porous materials like foam and rubber [Nashif, Jones, and Henderson, 1985; Munjal, 1987; Huang and Fuller, 1998; Pierce, 1989; Chapnik and Currie, 2000; Ahmadian, Jeric, and Inman, 2001]. They are effective at high frequencies and they usually do not achieve the desired attenuation at low frequencies. Although the implementation of passive-control techniques is simple, they usually result in a large increase in the overall system weight and size, and moreover, one may require expensive system redesign. On the other hand, active-control techniques are effective solutions for low-frequency applications. They can be grouped under *Active Noise Control* (ANC) and *Active Vibration Control* (AVC) categories. It is common in all active control schemes to use external energy sources to

absorb, or redirect, the undesired energy from the controlled system. Special considerations are needed when implementing active-control schemes, but they typically do not increase either the size or the weight of the controlled system. Examples of ANC and AVC schemes can be found in the efforts of Bai and Lin (1998); Heck, Olkin, and Naghshineh (1998); Beauvilain, Bolton, and Gardner (2000); Yoon and Kim (2000); and Yuan (2000).

In implementing an ANC scheme, one is interested in reducing sound by combining the primary field with a negative replica (sound field with an opposite phase and same amplitude) so that there is destructive interference, resulting in an acoustic shadow (quiet zone) covering the spatial area of interest. This *control* (or *secondary*) *sound* field is typically generated by loudspeakers placed at specific locations. Since the 1930s, when Paul Lueg (1936) proposed the use of a feedforward control scheme to globally attenuate periodic noise propagating inside a duct, feedforward approaches have been used in problems ranging from spatially one-dimensional systems to spatially three-dimensional systems. From the 1950s, spurred by the work of Olsen and May (1953) who proposed a feedback control scheme to locally attenuate the three dimensional sound field around a head seat, feedback approaches have been used extensively in many practical problems. ANC schemes have already been implemented on an industrial scale in applications such as HVAC duct systems, aircraft cabin noise control systems, and head seats. New schemes based on adaptive control and least mean square (LMS) algorithms have also been included in ANC systems to enhance noise reduction under varying conditions. Furthermore, ANC techniques have developed a new dimension with the relatively recent use of “active” materials such as piezoelectric, magnetostrictive, and electrostrictive

materials. The various advances in active noise control methodologies and applications made in this regard are well documented in the literature (e.g., Fuller and Von Flotow, 1995; Hernandez, 1995; Bai and Lin, 1998; Sun and Hirsch, 1998; Beauvilain *et al.*, 2000; Nelson and Elliott, 1992; Parkins, Sommerfeldt, and Tichy, 2000; Yoon and Kim, 2000; Yuan, 2000).

1.1. Previous Work

In Lueg's work (1936), a *reference microphone* was placed at a distance $\lambda/2$ upstream of a *control speaker* (or a *secondary noise source*) to control a noise tone with frequency $f = c/\lambda$, where λ is the wavelength of the tone and c is the speed of sound in air (please see Figure 1.1). The separation $\lambda/2$ causes a phase shift of 180° from the phase of the primary noise signal, and this results in destructive interference between the primary and secondary noise signals at the speaker location. In this work, the idea of a reference microphone, which senses the noise signal before it reaches the controller region, is introduced. Through this work, the basic principle of superposition in acoustic noise control is also introduced; a concept that is still commonly used nowadays in active control systems. The idea of using a control speaker to generate the control signal (or *secondary noise signal*) is central to active noise control systems (a control speaker is sometimes called the *secondary noise source*). The drawback of this system is the *inherent acoustic feedback* (IAF) path from the control speaker to the reference microphone. Such a feedback can cause a system instability.

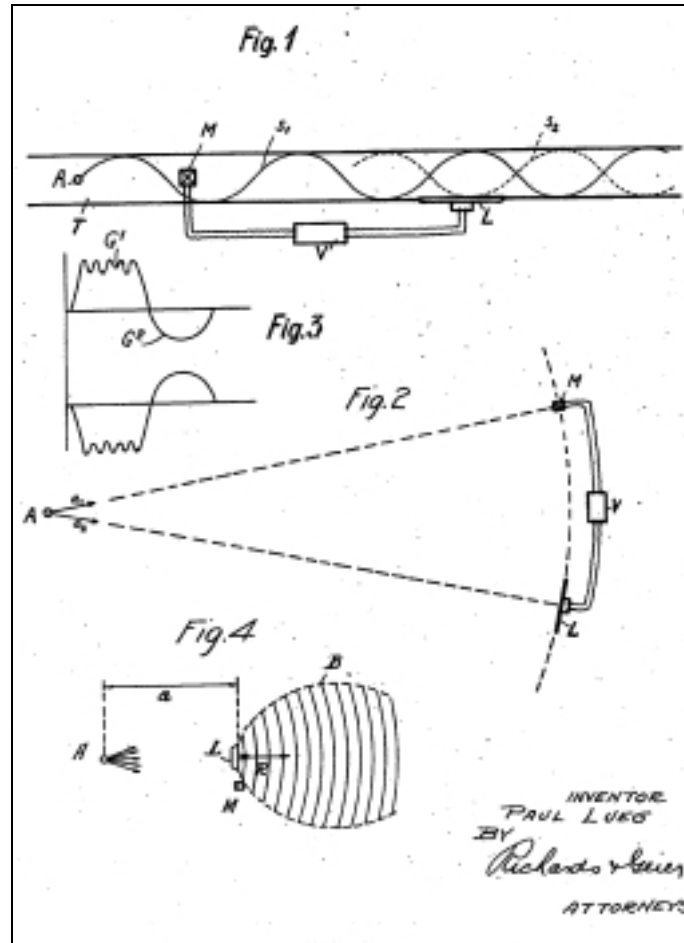


Figure 1.1. Adapted figures from Lueg's patent; United States Patent and Trademark Office, <http://www.uspto.gov>.

Jessel and Mangiante (1972) attempted to eliminate the IAF by using three control speakers to form a cardioid directivity pattern. In such a case, the feedback signal picked by the reference microphone and the standing waves can be cancelled.

In the work of Olsen and May (1953), a feedback control scheme is used. An error microphone was set in the proximity of a control speaker. The feedback signal from the microphone to the speaker was inverted to obtain negative feedback. The problem with such feedback control schemes is the possibility for the feedback to result in a

constructive noise interference instead of a destructive noise interference. Olsen and May overcame this problem by limiting the open loop gain at high frequencies to be below unity, when positive feedback occurred; this helped avoid an instability in the system. However, because of phase delays associated with wave propagation, for such a controller, as well as all feedback controllers, one can only realize localized regions of silence [Parkins, 1998].

Recently, Hong and Bernstein (1998) applied the so-called *zero spillover controller*, based on the early work of Roure (1985), to actively attenuate noise propagated through a one-dimensional duct by using a control speaker. In the literature, control spillover is associated with the excitation of unmodeled plant dynamics, while the observation spillover is associated with the sensing of unmodeled plant dynamics. However, in the present work, the definition, used by Hong and Bernstein (1998), is used. This definition is as follows: *Spillover occurs at a frequency ω , if the closed-loop transfer function magnitude is greater than the open-loop transfer function magnitude.* With this definition, spillover can occur whether or not the plant possesses unmodeled dynamics. In the present context, for a zero spillover control scheme, one attempts to keep the acoustic pressure, and hence the acoustic potential energy, of the controlled system below that of the uncontrolled system over and beyond the frequency range of interest. Hong and Bernstein pointed out that the following conditions must exist in order to realize a zero spillover controller: (1) the disturbance (primary) source and the control (secondary) sources are noncollocated and (2) the reference microphone and the error microphones are noncollocated. They showed that a feedforward zero spillover controller has a structure similar to that of an *H_2 -optimal feedback* controller. Although they did not

completely address the benefits of taking advantage of this similarity, they have shown through a numerical example that a zero spillover controller gives good broadband noise attenuation, which is typically difficult to achieve using many other feedforward schemes. These broadband attenuation characteristics make zero spillover control schemes attractive for complex problems such as control of three-dimensional enclosed sound fields.

Since the initial attempts of Lueg (1936) and Olsen and May (1953), and through the many research efforts that have followed, the ANC technique has been shown to be effective for attenuating noise levels that result from radiation into open acoustic fields as well as reverberant enclosed fields. However, in systems involving structural-acoustic interactions, the ANC scheme with control speakers has been shown to have physical limitations in controlling low-frequency noise associated with structural modes. This is basically due to the unacceptable size of the control speaker needed to generate low-frequency sound fields.

Active Structural-Acoustic Control (ASAC) which can be considered a modified version of ANC, takes advantage of vibrating structural elements as secondary noise sources to cancel the sound fields generated by a primary noise source (e.g., Fuller and Von Flotow, 1985; Sampath and Balachandran, 1997 and 1999; Balachandran and Zhao, 2000; Gibbs, Clark, Cox, and Viperman, 2000; Al-Bassiyouni and Balachandran, 2001; and Hong, Shin, Lee, and Oh, 2001). It appears that a ASAC scheme requires a fewer number of actuators and sensors than an ANC scheme in order to achieve widely distributed spatial noise reduction, especially in the low-frequency range. Furthermore, it has been shown that controlling the vibration levels of flexible enclosure panels does not necessarily

result in noise reduction inside an enclosure [Ahmadian *et al.*, 2001; Al-Bassyiouni and B. Balachandran, 2004; and Sampath, 1997]; a result that may suggest why a ASAC scheme is preferable over ANC scheme, since a ASAC system can address control of both structural vibrations and the associated sound fields. However, to develop model based ASAC schemes, one needs a good understanding of the structural-acoustic interactions in the considered system.

Considerable effort has been devoted to the modeling of structural acoustics, in particular, for enclosures with flexible boundaries. The efforts of Dowell and Voss (1963) and Lyon (1963) represent some of the early investigations into modeling of vibrations of plates backed by a cavity. Guy (1979) developed a model for the steady-state transmission of oblique sound waves through a thin panel backed by a rectangular room. In his work, the oblique incident wave was considered as a combination of a normally incident wave and a wave with grazing incidence. Balachandran, Sampath, and Park (1996) have developed a mechanics-based analytical model to address the interactions between a panel and the sound field inside a rectangular enclosure. In this work, piezoelectric patches bonded to the panel are used as actuators, which are also included in the modeling. Geng, Roa, and Han (2003) extended the work of Balachandran *et al.* (1996) to the case of an irregular enclosure with two flexible panels. In the efforts of Ro and Baz (1999), finite element models are constructed for similar problems, while Nefske Wolf, and Howell (1982) used a finite-element technique to model an automobile passenger compartment with flexible boundaries. Kim and Kim (2001) developed a mass-damper-spring system to address the case of a thin panel that partially covers a “small” rectangular cavity. Due to the low number of degrees of freedom used in this model, the

model's range of applicability is limited to the low-frequency range. Kim and Brennan (1999, 2000) used the impedance-mobility approach for modeling structural-acoustic coupling, and they applied that approach to a rectangular enclosure with a flexible panel. Their work has been extended by Lau and Tang (2003) to investigate the effect of the strength of the structural-acoustic coupling. As in the work of Balachandran *et al.* (1996), Chang and Nicholas (1992) used Green's functions to study the frequency response of structural-acoustic systems. This approach is suitable for frequency-response analysis, but not convenient for control designs that require time-domain models.

All of the previously mentioned studies are restricted to the interaction between the structure and cavity, and they do not consider the sound radiation from the panel into the external field; this aspect is important for feedforward control schemes where the IAF can cause a system instability. In addition, in all of the previous studies, the case where the panel-enclosure system is located in the near field of the noise source has not been considered; in these cases, the sound pressure field acting on the panel is not uniform. In systems such as a helicopter cabin, the noise source is "close" to the enclosure that the assumption of plane wave incidence may not be a good approximation for low-frequency ranges, which are the main targets of active control techniques. For the case of a spherical wave, the air particle velocity is no longer in phase with the acoustic pressure, and in addition, the pressure distribution on the flexible panel is neither constant nor linear, as it is for a plane wave with normal or oblique incidence.

1.2. Objectives and Scope of Dissertation Work

The overall objective of this work is to develop a ASAC feedforward controller for narrowband and broadband attenuation of enclosed three-dimensional sound fields, and to investigate the viability of using a zero spillover control scheme for this case. Specific objectives of the dissertation work are as follows:

- a) Develop an analytical model for three-dimensional enclosures with a flexible boundary located in the near field of an external noise source. The model should be able to predict the following: i) the internal sound fields, ii) the external sound fields, and iii) the structural-acoustic interactions
- b) Develop zero spillover control schemes to carry out spatially local control of sound fields in three-dimensional enclosures by using structural vibrations for generating the secondary noise signals
- c) Investigate the feasibility, effectiveness, and limitations of using the developed zero spillover schemes in three-dimensional enclosed ASAC systems through simulations and experiments

1.3. Organization of Dissertation

The rest of this dissertation is organized as follows. In the next chapter, the experimental arrangement is described, and in the third chapter, system models are developed through analytical and experimental efforts. In the fourth chapter, the control strategies used are introduced, and in the fifth and sixth chapters, two control schemes are developed and analyzed with the aid of simulations and experiments. In the following chapter, a

summary is presented along with suggestions for future work. References are included at the end. Detailed numerical results and experimental results and measurements are included in the six appendices at the end of the dissertation, including numerical and experimental results and the MATLAB codes used in this work.

2. Experimental Arrangement

In setting up the experimental arrangement, it was aimed to simulate the case of a helicopter cabin, which is exposed to noise from sources such as the helicopter rotor, gearbox, etc. Thus, the main elements in the experimental arrangement are a rectangular enclosure and a commercial three-way loudspeaker mounted above the enclosure that is used to simulate an external noise source [Balachandran *et al.*, 1996; Sampath and Balachandran, 1999]. The rectangular enclosure has five rigid walls made from 25.4 mm (1.0") thick acrylic sheets, and a flexible, top wall, which is made from 1.588 mm (1/16") thick aluminum material. This aluminum panel, which is clamped along all four edges, has the dimensions $L_{xp}=660.4$ mm (26.0") and $L_{yp}=508.0$ mm (20.0"). The inner dimensions of the enclosure are 609.6 mm \times 457.2 mm \times 508.0 mm (24.0" \times 18.0" \times 20.0"). The speaker, which has a diaphragm of 381.0 mm diameter (15.0"), is driven by one of the channels of a stereo amplifier and it is mounted at a distance of 762.0 mm (30.0") from the top of the enclosure. The mounting of the speaker is isolated from the enclosure structure, so the speaker excites the enclosure through airborne excitation only. A photograph of the experimental arrangement is shown in Figure 2.1.

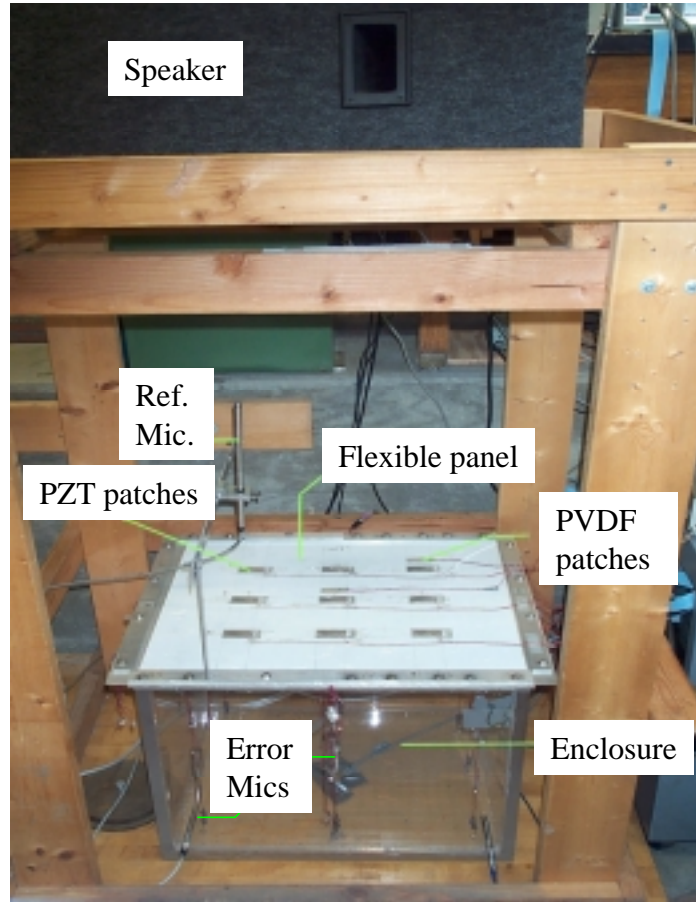


Figure 2.1. Photograph of the experimental arrangement; setup located in Vibrations Laboratory.

Piezoceramic Lead-Zirconate-Titanate (PZT-5H) patches, which are symmetrically mounted on the top and bottom surfaces of the panel, are used as actuators. The locations and geometry of the PZT patches are shown in Figure 2.2. The actuators are arranged in a grid with the column labels being {A, B, C} and the row labels being {1, 2, 3}. In the x - y coordinate system shown in Figure 2.2, the centers of the actuator pairs are located at $(0.25 L_{xp}, 0.25 L_{yp})$, $(0.25 L_{xp}, 0.50 L_{yp})$, $(0.25 L_{xp}, 0.75 L_{yp})$, $(0.50 L_{xp}, 0.25 L_{yp})$, $(0.50 L_{xp}, 0.50 L_{yp})$, $(0.50 L_{xp}, 0.75 L_{yp})$, $(0.75 L_{xp}, 0.25 L_{yp})$, $(0.75 L_{xp}, 0.50 L_{yp})$, and $(0.75 L_{xp}, 0.75 L_{yp})$. All actuators are identical, and each of them has the following dimensions:

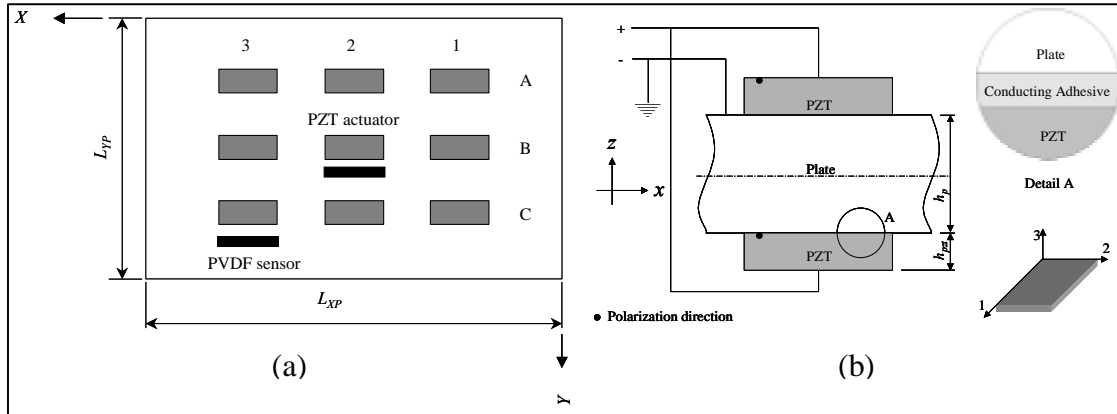


Figure 2.2. Experimental setup: (a) locations of structural actuators and sensors on the flexible panel and (b) panel-PZT patch geometry, electrical wiring, and principal axes for a PZT patch.

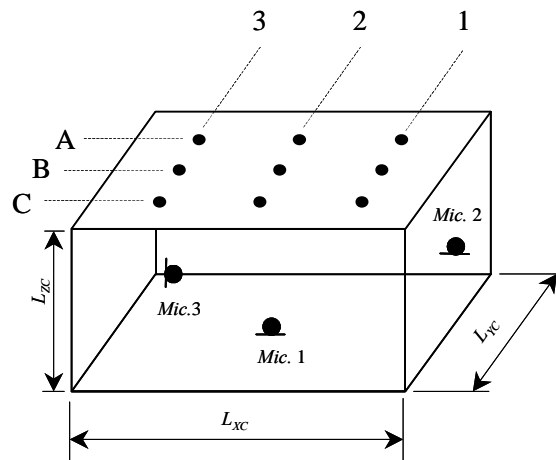


Figure 2.3. Locations of microphones inside the enclosure.

$L_{xpzt}=50.8$ mm, $L_{ypzt}=25.4$ mm, and thickness $h_{pzt}=0.3175$ mm ($2'' \times 1'' \times 0.0125''$). In each pair, the actuators are wired out of phase to cause extension in one patch and contraction in the other patch resulting in a “localized” bending moment at the edges of the pair, which represents the actuation effect (please see Figure 2.2(b) for electrical input and actuator pair geometry). Characteristics of the PZT patches are tabulated in Table 2.1.

Table 2.1. Small signal PZT 5H characteristics [Morgan Electro Ceramics].

d_{31} (10^{-12} m/V)	-274	Cure Point ($^{\circ}$ C)	193
d_{33} (10^{-12} m/V)	593	K_{11}^{σ}	3130
d_{15} (10^{-12} m/V)	741	K_{33}^{σ}	3400
s_{11}^E (10^{-12} m ² /V)	16.5	Compressive Strength (psi)	> 75,000
s_{33}^E (10^{-12} m ² /V)	20.7	Static Tensile Strength (psi)	11,000
s_{44}^E (10^{-12} m ² /V)	43.5	Poling Field (kV/cm)	12
s_{12}^E (10^{-12} m ² /V)	-4.78	Dielectric Breakdown (kV/cm)	20
s_{13}^E (10^{-12} m ² /V)	-8.45	Dipoling Field (kV/cm DC)	5.5
ρ (kg/m ³)	7500	Subscripts σ and E represent respectively constant stress and constant field conditions	

Polymer based piezoelectric (Polyvinylidene fluoride - PVDF) film sensors (DT2052 K/L) are bonded to the top surface of the plate close to the locations of the actuator pairs. The centers of the PVDF sensors, which are labeled P-B2 and P-C3 (the prefix P is used to denote PVDF), are located at (330.2 mm, 292.1 mm) and (495.3 mm, 414.0 mm), respectively.

Condenser microphones are used as sensors to measure pressure levels inside and outside the enclosure. The external microphone (referred to here as the *reference microphone*), which provides the reference signal to the control system, is placed at a height of 508.0 mm (20.0") above the panel-enclosure system. The internal microphones are arranged, so that all of the enclosure modes can be sensed. The microphones labeled Mic.1, Mic.2, and Mic.3 (please refer to Figure 2.3) are of special interest for the current

Table 2.2. Characteristics of different microphones used in the experimental setup.

Microphone (Brüel & Kjær)		Ref. Mic.	Mic.1	Mic.2	Mic.3
Model Number		B&K 4134	B&K 4145	B&K 4145	B&K 4133
Location (x, y, z)	inches	12,9,40	12,9,4 ½	1 ¼,4,9 ¼	22 ¾,1 ¾,1 ¼
	cm	30.5,22.9,101.6	30.5,22.9,10.8	3.2,10.2,23.5	57.8,4.4,3.2
Diameter	inches	½	1	1	½
	cm	1.3	2.5	2.5	1.3
Sensitivity (mV/Pa)		12.5	50	50	12.5
Polarization Voltage (V)		200	200	200	200
Frequency Range (Hz)		4 – 20k	2.6 – 18k	2.6 – 18k	4 – 40k
Dynamic Range (dB)		21 - 160	11 - 146	11 - 146	22 - 160



Figure 2.4. Photograph of the dSPACE interface system connected to a PIII-450 MHz PC; setup located in Vibrations Laboratory.

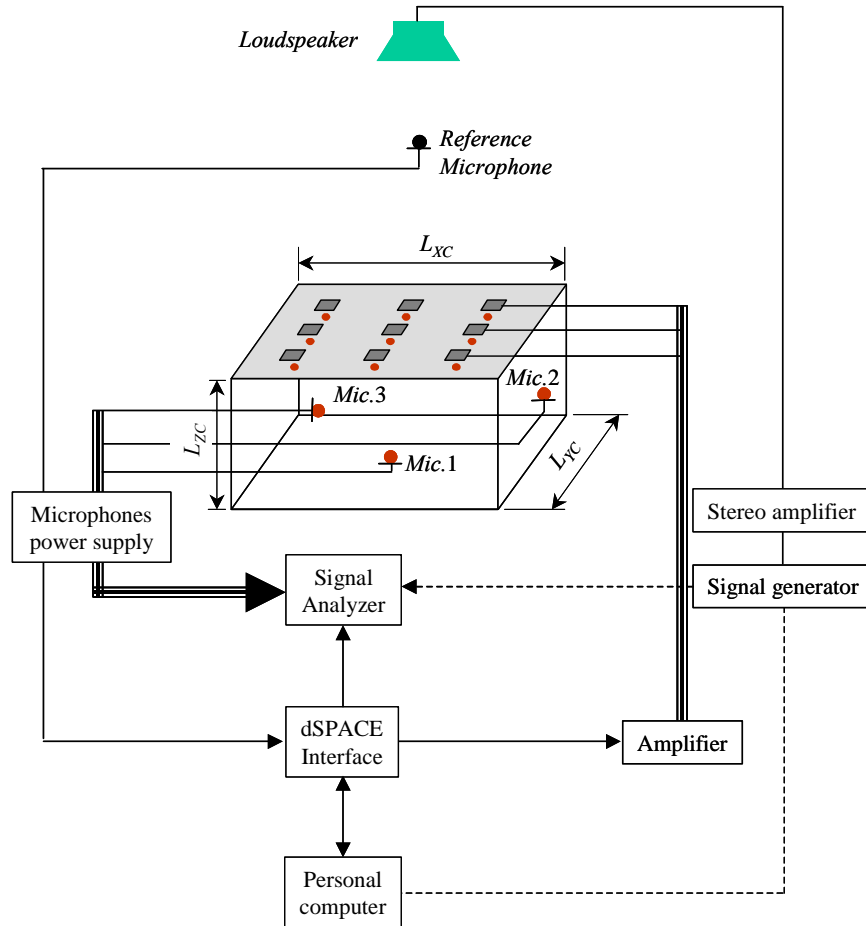


Figure 2.5. Schematic of the experimental setup, showing all the external peripherals and their interconnections with the different elements of the experiment.

work, and hence their characteristics are tabulated in Table 2.2.

The inputs to the actuators and the outputs from the sensors are realized through a personal computer (with a PIII-450 MHz processor) and a dSPACE interface with 32 input channels and 32 output channels. The interface system is shown in Figure 2.4. The dSPACE interface is programmed by using MATLAB-SIMULINK package and a Graphical User Interface (GUI) software called ControlDesk. The input and output

signals are also connected to a dynamic signal analyzer (HP 35665A) to perform frequency-response analysis.

A schematic representation of the experimental arrangement is shown in Figure 2.5, where the interconnections between the different elements along with the external peripherals are represented by lines and arrows. Arrows represent signal flow, while thick lines represent multiple signals. Broken lines represent temporary (offline) connections that are used only for experimental identification and calibrations. The reason that these connections are terminated when conducting real-time experiments is to ensure that the generated noise signal is totally independent of the rest of the system.

3. System Modeling

Analytical as well as experimental efforts have been pursued to develop a system model of the structural-acoustic system presented in Chapter 2. The purpose of the system model is to use it later in the control system design. Many modeling efforts have been documented in the literature. (Please, refer to Section 1.1 for more details.) One of the most comprehensive mechanics-based analytical development available in the literature is the work carried out by Sampath (1997), where different details are addressed at length. However, all of these efforts lack the following features: i) modeling of the external acoustics and their interactions with the enclosed acoustics; and ii) modeling of the system structural and acoustic interactions when placed in the near field of the noise source; that is, spatially close to the noise source or when subjected to low-frequency excitations. If the first feature is absent in the model, the effect of the inherent acoustic feedback cannot be predicted.

With the objective of designing a feedforward active structural-acoustic control scheme, which is very sensitive to system changes, a system model is needed to effectively capture the physical characteristics of the system, in particular, to predict the following: i) the internal sound fields, ii) the external sound fields, and iii) the structural-acoustic

interactions. Through these predictions, the pressure field at the reference microphone location due to the inherent acoustic feedback will be obtained here. Building on the work of Sampath (1997), an analytical model will be constructed in detail in the next section, followed by the construction of an experimentally identified model. It will be shown as to how these two models address the three points mentioned above. In order to enhance the control system functionality, the system models will also be used to identify the phase delays associated with the different transfer functions explicitly. Compared with the other efforts (e.g. the work of Yuan, 2000), when one explicitly identifies phase delays, this helps reduce the model dimensions needed to capture the various physical aspects of the system.

As will be shown later in Chapter 5, the analytical model is helpful in understanding the interconnections between the different parameters of the model and it can be used to predict the pressure fields over the entire enclosure; however, it cannot capture system variations that result from system non-uniformities and imperfect boundary conditions. It is also not applicable to enclosures with other shapes. The experimentally identified model can overcome these limitations, especially, when the enclosure shape is too complicated to analyze. However, an experimentally identified model cannot be realized except at the spatial locations of the sensors and actuators.

Comparisons between the experimental and analytical models in terms of the different system frequency-response measurements are also included in this chapter.

3.1. Analytical Model

In this section, a rectangular enclosure with one flexible panel at the top and five other

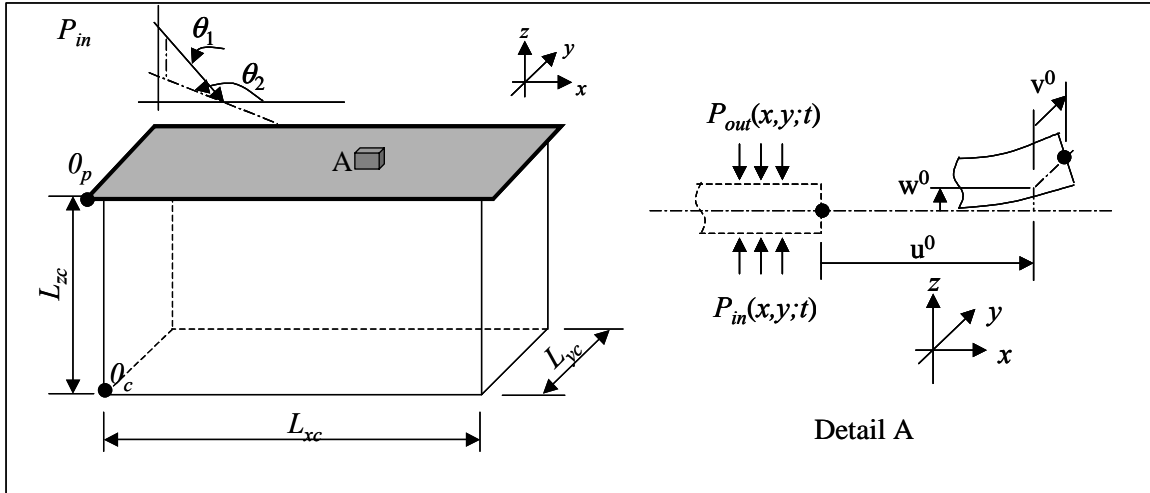


Figure 3.1. Schematic of the panel-enclosure system used for the analytical model.

fixed boundaries is considered. Efforts carried out to study the dynamics of this panel-enclosure system are described. PZT pair patches are considered to be bonded to the flexible panel, and each pair is assumed to produce a pure moment actuation, when an electric drive signal is used to excite patches that form this pair. The flexible panel is exposed to an external pressure excitation due to a spherical wave generated by a sound source mounted above the enclosure. The inner dimensions of the enclosure are L_{xc} , L_{ye} , and L_{zc} , in the x , y , and z directions, respectively, and the effective dimensions of the panel are L_{xp} and L_{yp} . As shown in the schematic of the panel-enclosure system (Figure 3.1), two coordinate systems are used to describe the system; the first one with the origin at θ_c is used for the enclosure, and the second one with the origin at θ_p is used for the panel. The panel may have larger dimensions than the enclosure, which is the case in the experimental arrangement discussed in Chapter 2.

Throughout the analysis, the bold notation is used to denote vector quantities and matrices and uniform ambient values are indicated with the subscript notation $(\bullet)_0$. For purposes of this chapter, the structural-acoustic system of interest is divided into the following subsystems: i) the panel-enclosure system, ii) the panel-piezo system, and iii) the panel-external sound field system.

3.1.1. Panel-Enclosure System

The two governing equations of this system are the mass conservation equation and the momentum conservation equation. In three-dimensional space, making use of linear approximations, the principle of mass conservation results in the equation

$$\frac{\partial \rho}{\partial t} + \rho_0 \nabla \cdot \mathbf{u} = 0, \quad (3.1)$$

where $\mathbf{u}(x,y,z;t)$ is the air particle velocity, ∇ is the divergence operator, and $\rho_0(x,y,z;t)$ is the ambient value of the air density. The momentum balance equation, after linearization, can be presented in the form

$$\rho_0 \frac{\partial \mathbf{u}}{\partial t} + \nabla p = 0, \quad (3.2)$$

where $p(x,y,z;t)$ is the air pressure inside the cavity. On eliminating the air-particle velocity from both equations, the homogenous wave equation for the sound pressure in the cavity can be obtained as

$$\nabla^2 p - \frac{\partial^2 p}{\partial t^2} = 0. \quad (3.3)$$

In this equation, the symbol ∇^2 represents the Laplace operator in the Cartesian coordinate system; in other words,

$$\nabla^2(\bullet) = \left(\frac{\partial^2}{\partial x^2} + \frac{\partial^2}{\partial y^2} + \frac{\partial^2}{\partial z^2} \right)(\bullet). \quad (3.4)$$

The speed of sound in a medium is defined as [Kinsler and Frey, 1962]

$$c = \sqrt{\frac{dp}{d\rho}}. \quad (3.5)$$

Assuming that the fluctuations in the pressure and density are small compared to their ambient values, then it can be shown that the pressure and density fluctuations are linearly related through the equation,

$$p = c_0^2 \rho. \quad (3.6)$$

Introducing a damping term with a damping coefficient γ_a , Eq. (3.3) can be modified to the form

$$\nabla^2 p - \frac{1}{c_0^2} \frac{\partial^2 p}{\partial t^2} - \gamma_a \frac{\partial p}{\partial t} = 0. \quad (3.7)$$

At a rigid boundary, the normal component of the air particle velocity is set to zero, and at a flexible boundary, it is set equal to the normal velocity of the flexible panel. Thus, the boundary conditions, with the aid of Eq. (3.2), can be stated as

$$\frac{\partial p}{\partial n} = \begin{cases} 0, & \text{at rigid boundary} \\ -\rho_0 \frac{\partial^2 w}{\partial t^2}, & \text{at flexible boundary} \end{cases} \quad (3.8)$$

where $w(x,y;t)$ is the normal displacement of the flexible boundary and n is the direction normal to the boundary. Since it is assumed here that the top panel is the only flexible one and that all of the other boundaries are rigid, the boundary conditions given in Eq. (3.8) can be written as

$$\left. \frac{\partial p}{\partial x} \right|_{x=0_c} = 0, \quad (3.9a)$$

$$\left. \frac{\partial p}{\partial x} \right|_{x=L_{xc}} = 0, \quad (3.9b)$$

$$\left. \frac{\partial p}{\partial y} \right|_{y=0_c} = 0, \quad (3.9c)$$

$$\left. \frac{\partial p}{\partial y} \right|_{y=L_{yc}} = 0, \quad (3.9d)$$

$$\left. \frac{\partial p}{\partial z} \right|_{z=0_c} = 0, \quad (3.9e)$$

and

$$\left. \frac{\partial p}{\partial z} \right|_{z=L_{zc}} = -\rho_0 \frac{\partial^2 w}{\partial t^2}. \quad (3.9f)$$

The separation of variables technique can be used to solve equation (3.7) with the

boundary conditions (3.9) and appropriate initial conditions. The pressure field inside the enclosure is assumed to have the form

$$\begin{aligned} p(x, y, z; t) &= \sum_{i=1}^{\infty} \Phi_i(x, y, z) q_i(t) \\ &= \sum_{i=1}^{\infty} \psi_i(x) \phi_i(y) \Gamma_i(z) q_i(t), \end{aligned} \quad (3.10)$$

where $\Phi_i(x, y, z)$ are used to describe the spatial field and $q_i(t)$ are used to describe the associated temporal part of the pressure response. The spatial functions $\psi_i(x)$, $\phi_i(y)$, and $\Gamma_i(z)$ are assumed to be orthogonal and satisfy the conditions

$$\int_{0c}^{L_{xc}} \psi_i \psi_j \, dx = \delta_{ij}, \quad (3.11a)$$

$$\int_{0c}^{L_{yc}} \phi_i \phi_j \, dy = \delta_{ij}, \quad (3.11b)$$

and

$$\int_{0c}^{L_{zc}} \Gamma_i \Gamma_j \, dz = \delta_{ij}, \quad (3.11c)$$

where

$$\delta_{ij} = \begin{cases} 0; & i \neq j \\ 1; & i = j \end{cases} \quad (3.12)$$

In terms of the spatial functions, the boundary conditions at the rigid boundaries can be now written as

$$\left. \frac{d\psi_i}{dx} \right|_{x=0c} = 0, \quad (3.13a)$$

$$\left. \frac{d\psi_i}{dx} \right|_{x=L_{xc}} = 0, \quad (3.13b)$$

$$\left. \frac{d\phi_i}{dy} \right|_{y=0c} = 0, \quad (3.13c)$$

$$\left. \frac{d\phi_i}{dy} \right|_{y=L_{yc}} = 0, \quad (3.13d)$$

and

$$\left. \frac{d\Gamma_i}{dz} \right|_{z=0c} = 0. \quad (3.13e)$$

Now, after substituting Eq. (3.10) into Eq. (3.7), integrating over the volume of the cavity, and making use of the orthogonality conditions given by Eqs. (3.11) and the boundary conditions given by Eqs. (3.13), the enclosure governing equations can be derived to have the following form

$$\frac{1}{c_0^2} \frac{d^2 q_i}{dt^2} + \gamma_a \frac{dq_i}{dt} + \left[k_i^2 - \left(\Gamma_i \frac{d\Gamma_i}{dz} \right) \Big|_{z=L_{zc}} \right] q_i = 0, \quad (3.14)$$

where

$$k_i^2 = \left[\int_{0c}^{L_{xc}} \left(\frac{d\psi_i}{dx} \right)^2 dx + \int_{0c}^{L_{yc}} \left(\frac{d\phi_i}{dy} \right)^2 dy + \int_{0c}^{L_{zc}} \left(\frac{d\Gamma_i}{dz} \right)^2 dz \right]. \quad (3.15)$$

Equation (3.14) will be used later on along with the panel-piezo equations to satisfy the boundary condition at the flexible panel.

3.1.2. Piezoelectric Actuator-Panel System

The piezoelectric actuator-panel system is treated here as a multi-laminated plate that consists of three plies in places where the piezo pair patches are bonded to the panel, and a single ply elsewhere. Plane stress theory is assumed. It is also assumed that all slope angles, as well as torsion effects, are “small”. Furthermore, it is assumed the tractions on surfaces parallel to the reference plane are negligible when compared to the in-plane stresses, and the in-plane displacements are linear functions of the normal coordinate z . Thus, the three displacement components u , v , and w defined respectively in the x , y , and z directions, can be expressed as

$$u(x, y, z; t) = u^0(x, y; t) - zw_{,x}^0, \quad (3.16a)$$

$$v(x, y, z; t) = v^0(x, y; t) - zw_{,y}^0, \quad (3.16b)$$

and

$$w(x, y, z; t) = w^0(x, y; t). \quad (3.16c)$$

In these equations, $(\bullet)^0$ indicates the displacement components at the neutral plane of the plate and $(\bullet)_{,i}$ is the derivative with respect to variable i . Here, since the plies are symmetrically distributed about the mid-plane, and with the assumption of homogeneous properties, the neutral plane is at the mid-plane of the plate. The strain equations can be written as

$$\boldsymbol{\varepsilon} = \boldsymbol{\varepsilon}^0 + z\boldsymbol{\kappa} + \boldsymbol{\Lambda}, \quad (3.17)$$

where

$$\boldsymbol{\varepsilon}^0 = \begin{pmatrix} \boldsymbol{\varepsilon}_x^0 \\ \boldsymbol{\varepsilon}_y^0 \\ \boldsymbol{\varepsilon}_{xy}^0 \end{pmatrix} = \begin{pmatrix} u_{,x}^0 \\ v_{,y}^0 \\ u_{,y}^0 + v_{,x}^0 \end{pmatrix}, \quad (3.18a)$$

$$\boldsymbol{\kappa} = \begin{pmatrix} \kappa_x \\ \kappa_y \\ \kappa_{xy} \end{pmatrix} = - \begin{pmatrix} w_{,xx} \\ w_{,yy} \\ 2w_{,xy} \end{pmatrix}, \quad (3.18b)$$

$$\boldsymbol{\Lambda} = \begin{pmatrix} d_{31}E_3 \\ d_{31}E_3 \\ 0 \end{pmatrix}, \quad (3.18c)$$

and

$$E_3 = \begin{cases} \frac{V}{h_{pzt}}; & \text{for PZT} \\ 0; & \text{for plate} \end{cases} \quad (3.18d)$$

In these equations, ε_i is the infinitesimal linear strain of an element in the i^{th} direction, $\boldsymbol{\varepsilon}$ is the strain tensor, κ_x , κ_y , and κ_{xy} are the plate curvatures, and $\boldsymbol{\Lambda}$ is the induced strain, which is dependent on the electric voltage V being fed into the piezo patches. This strain is non-zero only at the patch locations on the panel. Furthermore, E_3 is the electric field applied to a patch in the z -direction, and d_{31} and h_{pzt} are the dielectric constant and the thickness of the piezo patch, respectively. Nonlinear strain terms are not considered in

this analysis (for consideration of such terms, please see the work of Balachandran and Zhao, 2000).

Assuming isotropic properties, the constitutive relations for the piezoelectric material can be simplified to

$$\boldsymbol{\sigma} = \mathbf{C}_m \boldsymbol{\varepsilon}, \quad (3.19)$$

where

$$\boldsymbol{\sigma} = \begin{pmatrix} \sigma_x \\ \sigma_y \\ \sigma_z \end{pmatrix}, \quad (3.20a)$$

and

$$\mathbf{C}_m = \frac{E}{(1-\nu^2)} \begin{bmatrix} 1 & \nu & 0 \\ \nu & 1 & 0 \\ 0 & 0 & \frac{(1-\nu)}{2} \end{bmatrix}, \quad (3.20b)$$

where $\boldsymbol{\sigma}$ is the stress tensor, \mathbf{C}_m is the elastic stiffness tensor, and E and ν are respectively the Young's modulus and Poisson's ratios of the piezo or the panel materials, depending on where the relations are applied. The constitutive equations for the panel have the same form except that d_{31} for the panel is set to zero.

In calculating the forces N_i and moments M_i acting on the system, where the subscript i denotes here the action direction, the laminate plate theory is used, and the number of plies is set to *three* at the piezo patches locations and set to *one* elsewhere. This leads to

$$\mathbf{N} = \int_{-h/2}^{+h/2} \boldsymbol{\sigma} \, dz, \quad (3.21a)$$

and

$$\mathbf{M} = \int_{-h/2}^{+h/2} \boldsymbol{\sigma} \, z \, dz, \quad (3.21b)$$

where

$$\mathbf{N} = \begin{pmatrix} N_x \\ N_y \\ N_{xy} \end{pmatrix}, \quad (3.22a)$$

and

$$\mathbf{M} = \begin{pmatrix} M_x \\ M_y \\ M_{xy} \end{pmatrix}. \quad (3.22b)$$

In this equation, h is either the thickness of the panel only or the total thickness of the plate and the piezoelectric patches bonded to it, depending on where the relations are applied. Combining the force and moment equations for the piezoelectric actuator-panel system, the result obtained is

$$\begin{pmatrix} \mathbf{N} \\ \mathbf{M} \end{pmatrix} = \begin{bmatrix} \mathbf{A} & \mathbf{0} \\ \mathbf{0} & \mathbf{D} \end{bmatrix} \begin{pmatrix} \boldsymbol{\varepsilon} \\ \boldsymbol{\kappa} \end{pmatrix} + \begin{pmatrix} \mathbf{A}_\Lambda \\ \mathbf{D}_\Lambda \end{pmatrix} \Lambda. \quad (3.23)$$

This is a special form of the laminate plate equation, where the coupling stiffness terms are zero because of the symmetry of the panel and piezo patches about the neutral plane.

The matrix $\mathbf{A} \in \mathfrak{R}^{3 \times 3}$ is called the extension stiffness matrix while the matrix $\mathbf{D} \in \mathfrak{R}^{3 \times 3}$ is called the bending stiffness matrix. Both of these matrices, along with the induced coefficient matrices $\mathbf{A}_\Lambda \in \mathfrak{R}^{3 \times 3}$ and $\mathbf{D}_\Lambda \in \mathfrak{R}^{3 \times 3}$, are defined as follows

$$\mathbf{A} = \mathbf{A}_p + \mathbf{A}_{pzt}, \quad (3.24a)$$

$$\mathbf{D} = \mathbf{D}_p + \mathbf{D}_{pzt}, \quad (3.24b)$$

$$\mathbf{A}_\Lambda = 2 \sum_{i=1}^k h_{pzt} \chi_i C_{m_{pzt}}, \quad (3.24c)$$

and

$$\mathbf{D}_\Lambda = 2 \sum_{i=1}^k h_{pzt} (h_p + h_{pzt}) \chi_i C_{m_{pzt}}, \quad (3.24d)$$

where

$$\mathbf{A}_p = h_p C_{m_p}, \quad (3.25a)$$

$$\mathbf{A}_{pzt} = 2 \sum_{i=1}^k h_{pzt} \chi_i C_{m_{pzt}}, \quad (3.25b)$$

$$\mathbf{D}_p = \frac{h_p^3}{12} C_{m_p}, \quad (3.25c)$$

$$\mathbf{D}_{pzt} = 2 \sum_{i=1}^k \frac{h_p^3}{12} \alpha \chi_i C_{m_{pzt}}, \quad (3.25d)$$

$$\alpha = 6\zeta_h + 12\zeta_h^2 + 8\zeta_h^3, \quad (3.25e)$$

and

$$\zeta_h = \frac{h_{pzt}}{h_p}. \quad (3.25f)$$

In these equations, the subscripts p and pzt stand for the plate and piezo patch, respectively, the quantity $\chi_i = \chi(x_i, y_i)$ is unity where the i^{th} piezo patch pair is present, and it is zero elsewhere, and k is the total number of piezo patch pairs bonded to the panel. Here, the Poisson's ratios of the plate and patches are assumed to be the same [Sampath, 1997]. Based on Kirchhoff's hypothesis, the system equations can be written in the following form

$$N_{x,x} + N_{xy,y} + f_x = \rho_{pp} u_{,tt}^0 - I w_{,xtt}, \quad (3.26a)$$

$$N_{xy,x} + N_{y,y} + f_y = \rho_{pp} v_{,tt}^0 - I w_{,ytt}, \quad (3.26b)$$

$$N_x w_{,xx} + 2N_{xy} w_{,xy} + N_y w_{,yy} + Q_{x,x} + Q_{y,y} + w_{,x} (N_{x,x} + N_{xy,y}) + w_{,y} (N_{xy,x} + N_{y,y}) + f_z = \rho_{pp} w_{,tt}^0, \quad (3.26c)$$

and

$$M_{x,x} + M_{xy,y} - Q_x + m_x = I u_{,tt}^0 - J w_{,xtt}^0, \quad (3.26d)$$

$$M_{xy,x} + M_{y,y} - Q_y + m_y = I v_{,tt}^0 - J w_{,ytt}^0, \quad (3.26e)$$

where

$$\begin{pmatrix} \rho_{pp} \\ I \\ J \end{pmatrix} = \int_{-h/2}^{+h/2} \rho_p^{(k)} \begin{pmatrix} 1 \\ z \\ z^2 \end{pmatrix} dz, \quad (3.27)$$

and f_i , m_i , and Q_i are respectively the external forces and moments, and internal shear forces acting in the i^{th} direction, and $\rho_p^{(k)}$ is the mass density of the k^{th} laminate.

For thin plates, body forces and rotatory and in-plane inertia effects can be neglected. It is also assumed that there are no external in-plane forces acting on the plate system. Under these assumptions, the equations governing the shear forces can be simplified to the following forms

$$N_{x,x} + N_{xy,y} = 0, \quad (3.28a)$$

$$N_{xy,x} + N_{y,y} = 0, \quad (3.28b)$$

$$M_{x,x} + M_{xy,y} = Q_x, \quad (3.28c)$$

and

$$M_{xy,x} + M_{y,y} = Q_y. \quad (3.28d)$$

Applying these results to Eqs. (3.26), one gets

$$M_{x,xx} + 2M_{xy,xy} + M_{y,yy} + N_x w_{,xx} + 2N_{xy} w_{,xy} + N_y w_{,yy} + f_z = \rho_p h_p w_{,tt}. \quad (3.29)$$

Defining the differential operator matrix \mathbf{H} as

$$\mathbf{H} \cdot \mathbf{S} = \frac{\partial^2 \mathbf{S}}{\partial x^2} + \frac{\partial^2 \mathbf{S}}{\partial y^2} + 2 \frac{\partial^2 \mathbf{S}}{\partial x \partial y}, \quad (3.30)$$

where the dot notation is used to represent vector dot product, and using Eqs. (3.18b) and (3.22), one can represent Eq. (3.29) in the following compact form

$$\mathbf{H} \cdot \mathbf{M} - \mathbf{N} \cdot \boldsymbol{\kappa} + f_z = \rho_p h_p \ddot{w}, \quad (3.31)$$

where \ddot{w} is the second temporal derivative of $w(x,y;t)$. Making use of Eqs. (3.31), (3.23), and (3.24), and rearranging the terms, the result obtained is

$$\mathbf{H} \cdot \left[(\mathbf{D}_p + \mathbf{D}_{pzt}) \boldsymbol{\kappa} - \mathbf{D}_\Lambda \boldsymbol{\Lambda} \right] - f_z - \rho_p h_p \ddot{w} = (\mathbf{A} \boldsymbol{\varepsilon} - \mathbf{A}_\Lambda \boldsymbol{\Lambda}) \cdot \boldsymbol{\kappa}. \quad (3.32)$$

After substituting from Eq. (3.17) and neglecting the nonlinear terms and the in-plane displacements and passive stiffness terms due to the piezo patches, the right-hand side of the above equation becomes zero; the resulting equation is

$$D \nabla^4 w + \rho_p h_p \ddot{w} + \gamma_p \dot{w} = (p_{in} - p_{out}) - \sum_{i=1}^K \frac{(h_p + h_{pzt}) E_{pzt} d_{31}}{(1-\nu)} \nabla^2 \chi_i V_i(t), \quad (3.33)$$

where \dot{w} is the temporal first derivative of $w(x,y;t)$ and the panel stiffness constant D is given by

$$D = \frac{E_p h_p^3}{12(1-\nu^2)}. \quad (3.34)$$

In this equation, a damping term, with damping constant γ_p has been added to take panel damping into account. The external forcing term f_z is also substituted here with the pressure loading $(p_{in} - p_{out})$, where p_{out} is the external pressure loading on the panel and

p_{in} is the internal pressure loading on the panel (please refer to Figure 3.1). The external loading p_{out} consists of two pressure components, one due to the incident wave with pressure p_i , and the other due to the reflected wave with pressure p_r . In other words,

$$p_{out} = p_i + p_r, \quad (3.35)$$

where subscript “ i ” is used for the incident wave parameters and subscript “ r ” is used for the reflected wave parameters. The air-particle velocity in the z -direction right above and underneath the flexible panel is equal to the panel velocity. This is represented through the following relationship.

$$\mathbf{u}_i(x, y, L_{xc}) \cdot \hat{\mathbf{k}} + \mathbf{u}_r(x, y, L_{xc}) \cdot \hat{\mathbf{k}} = \mathbf{u}_{in}(x, y, L_{xc}) \cdot \hat{\mathbf{k}} = \frac{\partial w(x, y)}{\partial t}, \quad (3.36)$$

where $\hat{\mathbf{k}}$ is the unit vector in z -direction. The air-particle velocity is related to the pressure through the specific acoustic impedance \mathbf{z} . Harmonic wave analysis is used to derive this relationship.

Harmonic Wave Analysis

For spherical waves, the acoustic impedance is given by [Kinsler and Frey, 1962]

$$\mathbf{z} = \rho_0 c_0 \cos \theta e^{j\theta} \hat{\mathbf{e}}_r, \quad (3.37)$$

where

$$\theta = \cot^{-1}(kr), \quad (3.38)$$

$\hat{\mathbf{e}}_r$ is a unit vector along the radial direction from the source, and $\mathbf{r} = r \hat{\mathbf{e}}_r$ is the vector

from the sound source to a point (x,y) on the panel and k is the wave number, which is defined as the ratio of the driving frequency ω (in rad/s) to the speed of sound in air c_0 ; $k = \omega / c_0$. The acoustic impedance is a vector component, whose direction is coincident with the direction of $\hat{\mathbf{e}}_r$. Multiplying by the vertical component of \mathbf{z} , Eq. (3.36) becomes

$$p_i - p_r = -\rho_0 c_0 \frac{r_{sp}}{r} \cos \theta e^{j\theta} \frac{\partial w}{\partial t}; \quad (3.39)$$

where r_{sp} represents the vertical separation between the sound source and the panel. After substituting Eqs. (3.35) and (3.39) into (3.33), one obtains

$$D \nabla^4 w + \rho_p h_p \ddot{w} + \gamma_p \dot{w} + p_d = p_{in} - 2p_i - \sum_{i=1}^k \frac{(h_p + h_{pzl}) E_{pzl} d_{31}}{(1-\nu)} \nabla^2 \chi_i V_i(t). \quad (3.40)$$

In Eq. (3.40), p_d is a complex frequency and location dependent quantity, which is given by

$$p_d = \rho_0 c_0 \frac{r_{sp}}{r} \cos \theta e^{j\theta} \dot{w}. \quad (3.41)$$

As r increases, the reactive part approaches zero, while the resistive part approaches $\rho_0 c_0 \dot{w}$, which is the case of plane wave or far-field wave analysis. Thus, the term $(\gamma_p \dot{w} + p_d)$ is considered throughout this section as an effective damping term, and it illustrates how the cavity pressure field increases the damping of the panel vibration. In practice, the associated damping coefficient is usually experimentally determined, and this is also carried out here as discussed later in Section 3.1.6. Furthermore, to obtain Eq. (3.40), the wave transmitted through the flexible panel has been neglected in the

analysis. This approximation is reasonable for *acoustic rigid boundaries*, when the wave is incident on a medium that has a high characteristic impedance compared to that of the incident medium. In the present case, the specific acoustic impedance of air is roughly 0.003% of the specific acoustic impedance of aluminum.

The plate response is assumed to be of the form

$$w(x, y; t) = \sum_{i=1}^{\infty} \alpha_i(x) \beta_i(y) \eta_i(t), \quad (3.42)$$

where the $\eta_i(t)$ are temporal functions and, as shown in the work of Blevins (1979), the expressions for the spatial functions $\alpha_i(x)$ and $\beta_i(y)$ can be assumed to have the form

$$\begin{aligned} \alpha_i(x) = & \frac{1}{\sqrt{L_{xp}}} \left[\cosh\left(\lambda_1(i) \frac{x}{L_{xp}}\right) - \cos\left(\lambda_1(i) \frac{x}{L_{xp}}\right) \right] \\ & - \frac{\lambda_2(i)}{\sqrt{L_{xp}}} \left[\sinh\left(\lambda_1(i) \frac{x}{L_{xp}}\right) - \sin\left(\lambda_1(i) \frac{x}{L_{xp}}\right) \right] \end{aligned} \quad (3.43a)$$

and

$$\begin{aligned} \beta_i(y) = & \frac{1}{\sqrt{L_{yp}}} \left[\cosh\left(\lambda_1(i) \frac{y}{L_{yp}}\right) - \cos\left(\lambda_1(i) \frac{y}{L_{yp}}\right) \right] \\ & - \frac{\lambda_2(i)}{\sqrt{L_{yp}}} \left[\sinh\left(\lambda_1(i) \frac{y}{L_{yp}}\right) - \sin\left(\lambda_1(i) \frac{y}{L_{yp}}\right) \right] \end{aligned} \quad (3.43b)$$

In the above equations, $\lambda_1(i)$ and $\lambda_2(i)$ are real-valued constants for the i^{th} panel mode. The values of $\lambda_1(i)$ and $\lambda_2(i)$, as given by Blevins (1979), are tabulated in Table 3.1. Equation (3.40) will be integrated later with the panel-cavity equations to satisfy the

Table 3.1. Values of the constants $\lambda_1(i)$ and $\lambda_2(i)$ used in equation (3.42)

[Blevins, 1979].

	$i = 1$	2	3	4	5	> 5
$\lambda_1(i)$	4.73004074	7.85320462	10.9956079	14.1371655	17.2787597	$(2i+1)$ $\pi/2$
$\lambda_2(i)$	0.982502215	1.000777312	0.999966450	1.000001450	0.999999937	1.0

displacement boundary condition of the integrated system at the flexible panel.

3.1.3. Integrated Piezo-Panel-Enclosure System

In this section, the panel-cavity system is integrated with the piezoelectric actuator-panel system to obtain the governing equations for the integrated enclosure subsystem. The boundary condition at the flexible boundary is recalled from Eq. (3.9f) and rewritten below.

$$\left. \frac{\partial p}{\partial z} \right|_{z=L_{zc}} = -\rho_0 \frac{\partial^2 w}{\partial t^2} \quad (3.44)$$

Making use of this boundary condition along with Eqs. (3.10) and (3.42) and making use of the orthogonality property, one can get the following equation

$$\left. \frac{\partial \Gamma_j}{\partial z} \right|_{z=L_{zc}} q_j(t) = -\rho_0 \sum_{i=1}^{\infty} B_{ij}^{(c)}(x) B_{ij}^{(c)}(y) \ddot{\eta}_i(t), \quad (3.45)$$

where

$$B_{ij}^{(c)}(x) = \int_{0_c}^{L_{xc}} \alpha_i(x) \psi_j(x) dx, \quad (3.46a)$$

and

$$B_{ij}^{(c)}(y) = \int_{0_c}^{L_{yc}} \beta_i(x) \phi_j(x) dy. \quad (3.46b)$$

After substituting the above equations into Eqs. (3.14) and (3.15), one can get the equation governing a pressure-field mode as follows:

$$\frac{1}{c_0^2} \ddot{q}_j(t) + \gamma_a \dot{q}_j(t) + k_j^2 q_j(t) + \rho_0 \Gamma_j \left|_{z=L_{zc}} \sum_{i=1}^{\infty} B_{ij}^{(c)}(x) B_{ij}^{(c)}(y) \ddot{\eta}_i(t) = 0. \quad (3.47)$$

The last term on the left-hand side of Eq. (3.47) represents the structural-acoustic coupling in the system. At this stage, it is assumed that the spatial functions in Eq. (3.10) are given by rigid-body enclosure modes; that is [Kuttruff, 1981],

$$\psi_i(x) = \frac{A_i}{\sqrt{L_{xc}}} \cos\left(\frac{l_i \pi x}{L_{xc}}\right), \quad (3.48a)$$

$$\phi_i(y) = \frac{A_i}{\sqrt{L_{yc}}} \cos\left(\frac{m_i \pi y}{L_{yc}}\right), \quad (3.48b)$$

and

$$\Gamma_i(z) = \frac{A_i}{\sqrt{L_{zc}}} \cos\left(\frac{n_i \pi z}{L_{zc}}\right), \quad (3.48c)$$

where the indices l_i , m_i , and n_i are associated with the spatial functions of the i^{th} rigid enclosure mode, along the x , y , and z directions, respectively. The constants A_i are chosen to satisfy the orthogonality conditions given in Eqs. (3.11). It can be seen that for $A_i = \sqrt{2}$, the orthogonality conditions are satisfied for all values of $i \neq 0$, while for $A_i = 1$, the orthogonality conditions are satisfied for $i = 0$. Making use of Eqs. (3.15) and (3.48) in Eq. (3.47), it is found that

$$\begin{aligned} \frac{1}{c_0^2} \ddot{q}_j(t) + \gamma_a \dot{q}_j(t) + \left(\frac{l_j^2 \pi^2}{L_{xc}^2} + \frac{m_j^2 \pi^2}{L_{yc}^2} + \frac{n_j^2 \pi^2}{L_{zc}^2} \right) q_j(t) \\ + \rho_0 \frac{(-1)^j A_j}{\sqrt{L_{zc}}} \sum_{i=1}^{\infty} B_{ij}^{(c)}(x) B_{ij}^{(c)}(y) \dot{\eta}_i(t) = 0. \end{aligned} \quad (3.49)$$

The equations governing the panel modal amplitudes are obtained by making use of Eqs. (3.10), (3.40), (3.42), and (3.48). After approximating $p_d \approx \rho_o c_o \dot{w}$ and making use of the orthogonality properties and boundary conditions, the equation governing each panel modal amplitude is obtained as

$$\begin{aligned}
& \rho_p h_p \ddot{\eta}_j(t) + [\gamma_{pj} + \rho_0 c_0] \dot{\eta}_j(t) + D [I_j(x) + I_j(y)] \eta_j(t) + 2D \sum_{i=1}^{\infty} I_{ij}(x) I_{ij}(y) \eta_i(t) \\
&= \sum_{i=1}^{\infty} \frac{(-1)^i A_i}{\sqrt{L_{zc}}} B_{ij}^{(p)}(x) B_{ij}^{(p)}(y) q_i(t) - 2 \left[\int_{A_p} \alpha_j \beta_j p_i^s(x, y) dA_p \right] p_i^t(t) \\
&- \sum_{i=1}^k \left[\int_{A_p} \alpha_j \beta_j \frac{(h_p + h_{pz}) E_{pz} d_{31}}{(1-\nu)} \nabla^2 \chi(x_i, y_i) dA_p \right] V_i(t),
\end{aligned} \tag{3.50}$$

where the different spatial integrals are given by

$$B_{ij}^{(p)}(x) = \int_{0_c}^{L_{xc}} \psi_i(x) \alpha_j(x) dx, \tag{3.51a}$$

$$B_{ij}^{(p)}(y) = \int_{0_c}^{L_{yc}} \phi_i(y) \beta_j(y) dy, \tag{3.51b}$$

$$I_j(x) = \int_0^{L_{xp}} \alpha_j(x) \frac{d^4 \alpha_j(x)}{dx^4} dx, \tag{3.51c}$$

$$I_j(y) = \int_0^{L_{yp}} \beta_j(y) \frac{d^4 \beta_j(y)}{dy^4} dy, \tag{3.51d}$$

$$I_{ij}(x) = \int_0^{L_{xp}} \frac{d^2 \alpha_i(x)}{dx^2} \alpha_j(x) dx, \tag{3.51e}$$

and

$$I_{ij}(y) = \int_0^{L_{yp}} \frac{d^2 \beta_i(y)}{dy^2} \beta_j(y) dy. \tag{3.51f}$$

In Eq. (3.50), the incident pressure loading can be expressed as the product of spatial and

time domain functions; that is,

$$p_i(x, y; t) = p_i^s(x, y) p_i^t(t). \quad (3.52)$$

Noting that the panel extends beyond the enclosure size and the spatial functions $\psi_i(x)$ and $\phi_i(y)$ are not defined outside the x and y dimensions of the enclosure, the integration limits for $B_{ij}^{(p)}(x)$ and $B_{ij}^{(p)}(y)$ have been modified to take into account the size of the enclosure instead of the panel. This means that $B_{ij}^{(p)}(x) = B_{ji}^{(c)}(x)$ and $B_{ij}^{(p)}(y) = B_{ji}^{(c)}(y)$.

It is also mentioned that the orthogonality conditions can be used to simplify the terms I_j and I_{ij} to the following forms

$$I_j(x) = \int_0^{L_{xp}} \alpha_j(x) \frac{d^4 \alpha_j(x)}{dx^4} dx = \left(\frac{\lambda_{1j}}{L_{xp}} \right)^4, \quad (3.53a)$$

$$I_j(y) = \int_0^{L_{yp}} \beta_j(y) \frac{d^4 \beta_j(y)}{dy^4} dy = \left(\frac{\lambda_{1j}}{L_{yp}} \right)^4, \quad (3.53b)$$

$$\begin{aligned} I_{ij}(x) &= \int_0^{L_{xp}} \frac{d^2 \alpha_i(x)}{dx^2} \alpha_j(x) dx \\ &= \sqrt{I_j(x)} \left\{ \delta_{ij} + \frac{2}{\sqrt{L_{xp}}} \int_0^{L_{xp}} \left[\cos\left(\frac{\lambda_{1j}}{L_{xp}} x\right) - \lambda_{2j} \sin\left(\frac{\lambda_{1j}}{L_{xp}} x\right) \right] \alpha_j(x) dx \right\}, \end{aligned} \quad (3.53c)$$

and

$$\begin{aligned}
I_{ij}(y) &= \int_0^{L_{yp}} \frac{d^2 \beta_i(y)}{dy^2} \beta_j(y) dy \\
&= \sqrt{I_j(y)} \left\{ \delta_{ij} + \frac{2}{\sqrt{L_{yp}}} \int_0^{L_{xp}} \left[\cos\left(\frac{\lambda_{1j}}{L_{yp}} x\right) - \lambda_{2j} \sin\left(\frac{\lambda_{1j}}{L_{yp}} x\right) \right] \beta_j(y) dy \right\}.
\end{aligned} \tag{3.53d}$$

Now, equations (3.49) and (3.50) can be represented in matrix form, after truncating the infinite number of modes to the first M panel modes and N acoustic modes, as follows.

$$\begin{bmatrix} \mathbf{M}_{pp} & \mathbf{0} \\ \mathbf{M}_{cp} & \mathbf{M}_{cc} \end{bmatrix} \begin{bmatrix} \ddot{\mathbf{q}} \\ \ddot{\mathbf{q}} \end{bmatrix} + \begin{bmatrix} \mathbf{D}_{pp} & \mathbf{0} \\ \mathbf{0} & \mathbf{D}_{cc} \end{bmatrix} \begin{bmatrix} \dot{\mathbf{q}} \\ \dot{\mathbf{q}} \end{bmatrix} + \begin{bmatrix} \mathbf{K}_{pp} & \mathbf{K}_{pc} \\ \mathbf{0} & \mathbf{K}_{cc} \end{bmatrix} \begin{bmatrix} \boldsymbol{\eta} \\ \mathbf{q} \end{bmatrix} = \begin{bmatrix} \mathbf{F}_p & \mathbf{F}_V \\ \mathbf{0} & \mathbf{0} \end{bmatrix} \begin{bmatrix} p_i^t \\ \mathbf{v} \end{bmatrix}, \tag{3.54}$$

In these equations, $\{\mathbf{M}_{pp}, \mathbf{D}_{pp}, \mathbf{K}_{pp}\} \in \mathfrak{R}^{M \times M}$, $\{\mathbf{M}_{cc}, \mathbf{D}_{cc}, \mathbf{K}_{cc}\} \in \mathfrak{R}^{N \times N}$, $\mathbf{M}_{cp} \in \mathfrak{R}^{N \times M}$, $\mathbf{K}_{pc} \in \mathfrak{R}^{M \times N}$, $\mathbf{F}_p \in \mathfrak{R}^{M \times 1}$, and $\mathbf{F}_V \in \mathfrak{R}^{M \times k}$. The different quantities in the above equation are given by

$$\mathbf{M}_{pp} = \text{diag}[\rho_p h_p], \tag{3.55a}$$

$$\mathbf{M}_{cc} = \text{diag}\left[\frac{1}{c_0^2}\right], \tag{3.55b}$$

$$\mathbf{M}_{cp} = [M_{cp}(i, j)] = \rho_0 \left[\frac{(-1)^i A_i}{\sqrt{L_{zc}}} B_{ji}^{(c)}(x) B_{ji}^{(c)}(y) \right], \tag{3.55c}$$

$$\mathbf{D}_{pp} = \text{diag}[\gamma_{pj} + \rho_0 c_0] = \text{diag}[2\zeta_{pj} \omega_{pj} \rho_p h_p + \rho_0 c_0], \tag{3.55d}$$

$$\mathbf{D}_{cc} = \text{diag}[\gamma_{aj}] = \frac{1}{c_0^2} \text{diag}[2\zeta_{cj} \omega_{cj}], \tag{3.55e}$$

$$\mathbf{K}_{pp} = [k_{pp}(i, j)] = 2D [I_{ji}(x)I_{ji}(y)] + D \text{diag}[I_i(x) + I_i(y)], \quad (3.55f)$$

$$\mathbf{K}_{cc} = \text{diag} \left[\frac{l_i^2 \pi^2}{L_{xc}^2} + \frac{m_i^2 \pi^2}{L_{yc}^2} + \frac{n_i^2 \pi^2}{L_{zc}^2} \right], \quad (3.55g)$$

$$\mathbf{K}_{pc} = [k_{pc}(i, j)] = \left[-\frac{(-1)^j A_j}{\sqrt{L_{zc}}} B_{ji}^{(p)}(x) B_{ji}^{(p)}(y) \right], \quad (3.55h)$$

$$\mathbf{F}_p = \left(-2 \int_{A_p} \alpha_i \beta_i p_i^s \, dA_p \right), \quad (3.55i)$$

and

$$\mathbf{F}_V = [F_V(i, j)] = \left[- \int_{A_p} \alpha_i \beta_i \frac{(h_p + h_{pzt}) E_{pzt} d_{31}}{(1-\nu)} \nabla^2 \chi(x_j, y_j) \, dA_p \right]. \quad (3.55j)$$

The damping ratios ζ_{pi} and ζ_{cj} correspond to the i^{th} panel mode and j^{th} enclosure mode, respectively, in the case of the uncoupled system. Furthermore, the off-diagonal block matrices \mathbf{M}_{cp} and \mathbf{K}_{pc} describe the structural-acoustic coupling, while the off-diagonal entries in \mathbf{K}_{pp} represents the coupling between the different panel modes. (This coupling can be discerned from the definitions of $I_{ij}(x)$ and $I_{ij}(y)$ in Eqs. (3.51e) and (3.51f).) It is shown here that the coupling affects the damping associated with the panel vibrations but does not add to the damping associated with the enclosure. Investigations into the pressure forcing coefficients \mathbf{F}_p in Eq. (3.55i) show that for a plane wave incidence with a wave front parallel to the panel, vibration modes with even x and/or y indices will not be excited; in this case, p_i^s is unity or another constant value. Furthermore, the entries of the

coupling mass matrix \mathbf{M}_{cp} in Eq. (3.55c) and stiffness matrix \mathbf{K}_{pc} in Eq. (3.55h) show that the acoustic mode (0,0,1) is coupled only to the odd \times odd vibration modes, the acoustic mode (1,0,0) is coupled only to the even \times odd vibration modes, and the acoustic mode (0,1,0) is coupled only to the odd \times even vibration modes. This can also be understood from the spatial shapes of the different modes in the xyz coordinate system.

The integrations in the voltage forcing coefficients $F_V(i,j)$ can be calculated using the method of integration by parts; this leads to

$$F_V(i, j) = \frac{(h_p + h_{pzt})E_{pzt}d_{31}}{(1-\nu)} \left(\left. \frac{d}{dx} \alpha_i(x) \right|_{x=x_{1j}} - \left. \frac{d}{dx} \alpha_i(x) \right|_{x=x_{0j}} \right) \int_{y_{0j}}^{y_{1j}} \beta_i(y) dy + \frac{(h_p + h_{pzt})E_{pzt}d_{31}}{(1-\nu)} \left(\left. \frac{d}{dy} \beta_i(y) \right|_{y=y_{1j}} - \left. \frac{d}{dy} \beta_i(y) \right|_{y=y_{0j}} \right) \int_{x_{0j}}^{x_{1j}} \alpha_i(x) dx; \quad (3.56)$$

where x_{0j} and x_{1j} are the locations of the starting and ending edges of the j^{th} PZT patch in the x direction, and y_{0j} and y_{1j} are the locations of the starting and ending edges in the y direction.

Equations (3.54) represent the time-domain model developed for the system shown in Figure 3.1. After determining the modal amplitudes from these equations, the panel displacements $w(x,y;t)$ and the pressure fields inside the enclosure $p(x,y,z;t)$ can be obtained from the following relations

$$\begin{pmatrix} w(x, y; t) \\ p(x, y, z; t) \end{pmatrix} = \begin{bmatrix} \mathbf{C}^{(w)}(x, y) & \mathbf{0} \\ \mathbf{0} & \mathbf{C}^{(p)}(x, y, z) \end{bmatrix} \begin{pmatrix} \boldsymbol{\eta}(t) \\ \mathbf{q}(t) \end{pmatrix}, \quad (3.57)$$

where

$$\mathbf{C}^{(w)} = [\alpha_i(x) \beta_i(y)] \quad (3.58a)$$

and

$$\mathbf{C}^{(p)} = [\psi_i(x) \phi_i(y) \Gamma_i(z)]. \quad (3.58b)$$

3.1.4. Panel-External Sound Field System

In this section, the system equations (3.54) are extended to consider the pressure field at an observation point located at a distance $r_{op,s}$ from the noise source, as shown in Figure 3.2. Spatially, this point is located in between the noise source and the enclosure. For ASAC feedforward schemes, such an analysis is needed for modeling the reference microphone sensor signal. In the following development, the pressure source outside the enclosure is assumed to generate a harmonic excitation.

The acoustic pressure at the considered observation point is treated as a superposition of pressures generated by the following two sources: (1) the acoustic pressure $p_{op1}(t)$ generated by the external or primary (noise) source and (2) the acoustic pressure $p_{op2}(t)$ reflected back from the flexible panel as well as that generated by the panel vibrations when excited by the noise source and/or by providing inputs into the PZT patches. The external noise source is considered as a circular “unbaffled simple” sound source, with radius r_s and uniform surface velocity $u(t)$; this source is located at an arbitrary location above the panel and it is assumed to transmit sound downwards only. Then, for a harmonic excitation, the surface velocity is

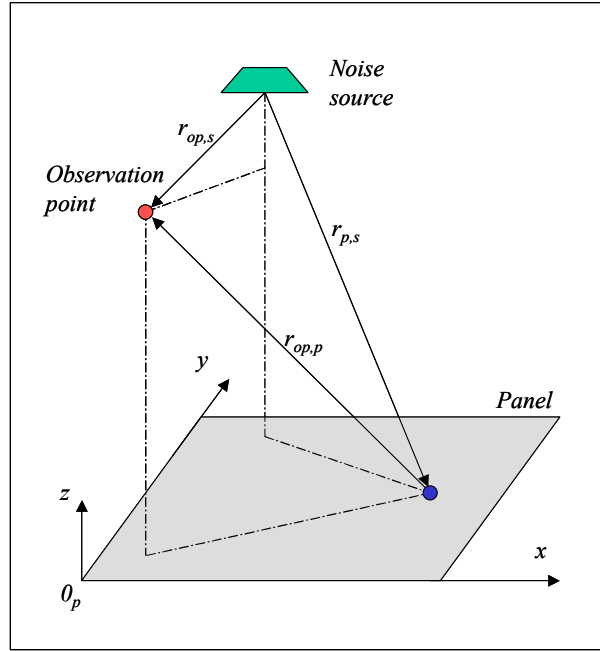


Figure 3.2. Schematic showing the locations of the noise source and the observation point with respect to the flexible panel.

$$u(t) = U e^{j\omega t}, \quad (3.59)$$

and the source strength can be written as

$$Q = \pi r_s^2 U. \quad (3.60)$$

Thus, the equation describing $p_{op1}(t)$ is of the form [Kinsler and Frey, 1962]

$$p_{op1}(t) = \frac{1}{2} j\rho_0 c_0 \left[\frac{Q}{\lambda r_{sr}} \right] e^{j(\omega t - k r_{op,s})}, \quad (3.61)$$

where λ is the wave length of the excitation noise and k is the wave number. Equation (3.61) can be expressed in terms of the baffle surface acceleration $a_s(t) = j\omega U e^{j\omega t}$, as follows

$$\begin{aligned}
p_{op1}(t) &= \frac{\rho_0 r_s^2}{4 r_{op,s}} e^{-jk r_{op,s}} a_s(t) \\
&= \frac{\rho_0 r_s^2}{4 r_{op,s}} e^{-j\omega T_{op1}} a_s(t).
\end{aligned} \tag{3.62}$$

The time delay constant T_{op1} in the above equation is given by

$$T_{op1} = \frac{r_{op,s}}{c_0}. \tag{3.63}$$

The pressure $p_{op2}(t)$ generated from the panel motions can be determined by dividing the panel into infinitesimal elements of area dA , each of which is considered as a ‘‘baffled simple’’ source of strength

$$dQ = \dot{w}(x, y; t) dA. \tag{3.64}$$

This pressure component is given by

$$p_{op2}(t) = \frac{\rho_0}{2\pi} \iint_{A_p} \dot{w}(x, y, t) \frac{e^{-jkr_{op,p}}}{r_{op,p}} dA, \tag{3.65}$$

where $r_{op,p}(x, y)$ is the location of the observation point relative to point (x, y) on the panel.

Making use of Eq. (3.42), $p_{op2}(t)$ can be put in the form

$$p_{op2}(t) = \sum_{i=1}^M C_i^{(op)} \ddot{\eta}_i(t), \tag{3.66}$$

where

$$C_i^{(op)} = \frac{\rho_0}{2\pi} \iint_{A_p} \alpha_i(x) \beta_i(y) \frac{e^{-jk r_{op,p}}}{r_{op,p}} dA. \quad (3.67)$$

Then, the acoustic pressure at the observation point can be determined as the sum of Eqs. (3.62) and (3.66), or, in other words,

$$p_{op}(t) = \frac{\rho_0 r_s^2}{4 r_{op,s}} e^{-j\omega T_{op1}} a_s(t) + \sum_{i=1}^M C_i^{(op)} \ddot{\eta}_i(t). \quad (3.68)$$

Following a similar procedure, the pressure field $p_i(x,y;t)$ at a point (x,y) just above the panel surface can be determined as a function of $a_s(t)$. With the aid of Figure 3.2, the pressure field at a point adjacent to the panel can be determined as

$$p_i(x, y; t) = \frac{\rho_0 r_s^2}{4} \frac{e^{-jk r_{p,s}}}{r_{p,s}} a_s(t), \quad (3.69)$$

where $r_{p,s}(x,y)$ is the distance from the noise source to the point (x,y) on the panel.

3.1.5. Equations of the Complete System

Making use of Eq. (3.69) in Eqs. (3.54) and (3.55), the overall system equations will have the following form, where the pressure input in that equation is now replaced by the acceleration of the speaker diaphragm; that is,

$$\begin{bmatrix} \mathbf{M}_{pp} & \mathbf{0} \\ \mathbf{M}_{cp} & \mathbf{M}_{cc} \end{bmatrix} \begin{bmatrix} \ddot{\boldsymbol{\eta}} \\ \ddot{\mathbf{q}} \end{bmatrix} + \begin{bmatrix} \mathbf{D}_{pp} & \mathbf{0} \\ \mathbf{0} & \mathbf{D}_{cc} \end{bmatrix} \begin{bmatrix} \dot{\boldsymbol{\eta}} \\ \dot{\mathbf{q}} \end{bmatrix} + \begin{bmatrix} \mathbf{K}_{pp} & \mathbf{K}_{pc} \\ \mathbf{0} & \mathbf{K}_{cc} \end{bmatrix} \begin{bmatrix} \boldsymbol{\eta} \\ \mathbf{q} \end{bmatrix} = \begin{bmatrix} \mathbf{F}_a & \mathbf{F}_V \\ \mathbf{0} & \mathbf{0} \end{bmatrix} \begin{bmatrix} a_s \\ \mathbf{v} \end{bmatrix}, \quad (3.70)$$

where

$$\mathbf{F}_a = \left(-\frac{\rho_0 r_s^2}{2} \iint_{A_p} \alpha_i \beta_i \frac{e^{-jk r_{p,s}}}{r_{p,s}} dA_p \right). \quad (3.71)$$

After solving Eq. (3.70) for the modal amplitudes in the frequency domain, the total pressure at an observation point above the enclosure can be determined from

$$p_{op}(t) = -[\bar{\mathbf{C}}^{(op)} \mathbf{K}_{pp} + j\omega \bar{\mathbf{C}}^{(op)} \mathbf{D}_{pp}] \boldsymbol{\eta} - [\bar{\mathbf{C}}^{(op)} \mathbf{K}_{pc}] \mathbf{q} + [\bar{\mathbf{C}}^{(op)} \mathbf{F}_V] \mathbf{V} + (\bar{\mathbf{C}}^{(op)} \mathbf{F}_p + D^{(op)}) a_s, \quad (3.72)$$

where

$$\bar{\mathbf{C}}^{(op)} = \mathbf{C}^{(op)} \mathbf{M}_{pp}^{-1} = \left[\frac{C_i^{(op)}}{\rho_p h_p} \right], \quad (3.73a)$$

and

$$D^{(op)} = \frac{\rho_0 r_s^2}{4 r_{op,s}} e^{-j\omega T_{op1}}. \quad (3.73b)$$

After using equations (3.57) and (3.72), the panel displacement $w(x,y;t)$, the pressure inside the enclosure $p(x,y,z;t)$, and the pressure at the observation point $p_{op}(t)$ can be determined from

$$\begin{aligned}
\begin{pmatrix} w(x, y, z, t) \\ p(x, y, z, t) \\ p_{op}(t) \end{pmatrix} &= \begin{bmatrix} \mathbf{C}^{(w)} & \mathbf{0} & \mathbf{0} & \mathbf{0} \\ \mathbf{0} & \mathbf{C}^{(p)} & \mathbf{0} & \mathbf{0} \\ -\bar{\mathbf{C}}^{(op)}\mathbf{K}_{pp} & -\bar{\mathbf{C}}^{(op)}\mathbf{K}_{pc} & -\bar{\mathbf{C}}^{(op)}\mathbf{D}_{pp} & \mathbf{0} \end{bmatrix} \begin{pmatrix} \boldsymbol{\eta} \\ \mathbf{q} \\ \dot{\boldsymbol{\eta}} \\ \dot{\mathbf{q}} \end{pmatrix} \\
&+ \begin{bmatrix} \mathbf{0} & \mathbf{0} \\ \mathbf{0} & \mathbf{0} \\ \bar{\mathbf{C}}^{(op)}\mathbf{F}_a + D^{(op)} & \bar{\mathbf{C}}^{(op)}\mathbf{F}_V \end{bmatrix} \begin{pmatrix} a(t) \\ \mathbf{V} \end{pmatrix}.
\end{aligned} \tag{3.74}$$

Since this model is mainly required for the control system designs described in Chapter 4, the model equations are rearranged to fit into a state space form as follows.

$$\dot{\mathbf{X}}(t) = \mathbf{A} \mathbf{X}(t) + \mathbf{B} \mathbf{U}(t), \tag{3.75}$$

where $\mathbf{X} \in \mathfrak{R}^{(2M+2N) \times 1}$ is the system state vector, $\mathbf{U} \in \mathfrak{R}^{(k+1) \times 1}$ is the input vector, $\mathbf{A} \in \mathfrak{R}^{(2M+2N) \times (2M+2N)}$ is the system matrix, and $\mathbf{B} \in \mathfrak{R}^{(2M+2N) \times (M+N+k+1)}$ is the input matrix. The different matrices in Eq. (3.75) have the following forms:

$$\mathbf{X} = \begin{pmatrix} \boldsymbol{\eta}(t) \\ \mathbf{q}(t) \\ \dot{\boldsymbol{\eta}}(t) \\ \dot{\mathbf{q}}(t) \end{pmatrix}, \tag{3.76a}$$

$$\mathbf{U} = \begin{pmatrix} p_s(t) \\ \mathbf{V}(t) \end{pmatrix}, \tag{3.76b}$$

$$\mathbf{A} = \begin{bmatrix} \mathbf{0} & \mathbf{I} \\ -\mathbf{M}^{-1}\mathbf{K} & -\mathbf{M}^{-1}\mathbf{D} \end{bmatrix}, \tag{3.76c}$$

and

$$\mathbf{B} = \begin{bmatrix} \mathbf{0} \\ \mathbf{M}^{-1}\mathbf{F} \end{bmatrix}. \quad (3.76d)$$

Furthermore, the inverse of the mass matrix defined in Eq. (3.54) will have the following form [Sánchez-Peña and M. Sznaier, 1998]

$$\mathbf{M}^{-1} = \begin{bmatrix} \mathbf{M}_{pp}^{-1} & \mathbf{0} \\ -\mathbf{M}_{cc}^{-1}\mathbf{M}_{cp}\mathbf{M}_{pp}^{-1} & \mathbf{M}_{cc}^{-1} \end{bmatrix}. \quad (3.77)$$

Then, the system and input matrices can be rewritten as follows:

$$\mathbf{A} = \begin{bmatrix} \mathbf{0}_{M \times M} & \mathbf{0}_{M \times N} & \mathbf{I}_{M \times M} & \mathbf{0}_{M \times N} \\ \mathbf{0}_{N \times M} & \mathbf{0}_{N \times N} & \mathbf{0}_{N \times M} & \mathbf{I}_{N \times N} \\ -\frac{1}{\rho_p h_p} \mathbf{K}_{pp} & -\frac{1}{\rho_p h_p} \mathbf{K}_{pc} & -\text{diag}[2\zeta_i \omega_{pi} + \rho_0 c_0] & \mathbf{0}_{M \times N} \\ \frac{c_0^2}{\rho_p h_p} \mathbf{M}_{cp} \mathbf{K}_{pp} & \frac{c_0^2}{\rho_p h_p} \mathbf{M}_{cp} \mathbf{K}_{pc} - c_0^2 \mathbf{K}_{cc} & c_0^2 \mathbf{M}_{cp} \text{diag}[2\zeta_i \omega_{pi} + \rho_0 c_0] & -\text{diag}[2\zeta \omega_c] \end{bmatrix} \quad (3.78a)$$

$$\mathbf{B} = \begin{bmatrix} \mathbf{0}_{M \times 1} & \mathbf{0}_{M \times k} \\ \mathbf{0}_{N \times 1} & \mathbf{0}_{N \times k} \\ \frac{1}{\rho_p h_p} \mathbf{F}_a & \frac{1}{\rho_p h_p} \mathbf{F}_V \\ \frac{c_0^2}{\rho_p h_p} \mathbf{M}_{cp} \mathbf{F}_a & \frac{c_0^2}{\rho_p h_p} \mathbf{M}_{cp} \mathbf{F}_V \end{bmatrix} \quad (3.78b)$$

Compared with the work of Sampath (1997), and the other efforts in the literature, the system matrices of this current analytical model have the following features:

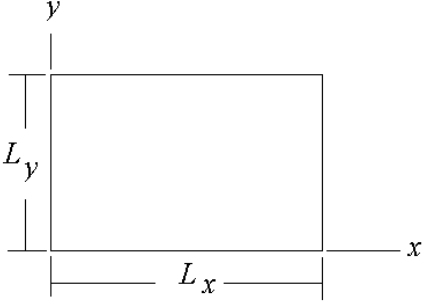
- *The model takes into account the effects of the general case of spherical wave incidence at the flexible panel, for example, through the matrix \mathbf{F}_a in Eq. (3.71). Although it has not been used here for this purpose, the model can also be used to analyze plane wave incidence with wavelengths much less than the dimensions of the flexible boundary. In this case, the term $p_i(x,y)$ will describe the distribution of the incident wave as it hits the flexible panel.*
- *The model takes into account the damping effects of the panel-external sound interactions, which is achieved by the insertion of the term $\rho_0 c_0$ in Eq. (3.78a).*
- *The model can predict the external pressure field, as shown in Eq. (3.74), in the presence of non-uniform panel vibrations as well as near-field loudspeaker excitations; this feature is used in the control design to determine the inherent acoustic feedback.*

However, the analytical model has some limitations, which are discussed in detail in Section 3.3. Because of these limitations, it is important that an effort be pursued to obtain a system model based on experimental identification as well. This effort is detailed in Section 3.2. The analytical model will still be used, along with the experimentally identified model, in designing the control schemes and to understand the pressure field distributions in the uncontrolled and controlled cases. It is also used as a starting point for the experimental identification efforts presented in Section 3.2.

3.1.6. Numerical Results

Here, the numerical results obtained from the analytical model developed in this chapter

Table 3.2. Coefficients in approximate formulae for clamped rectangular plate [Blevins, 1979].

Mode Index	G	H	 <p>$G=G_1$, $H=H_1$, and mode index=i when boundary conditions are applied to sides of length L_y. $G=G_2$, $H=H_2$, and mode index=j when boundary conditions are applied to sides of length L_x.</p>
1	1.506	1.248	
2	2.500	4.658	
3	3.500	10.02	
$n (n > 1)$	$n + \frac{1}{2}$	$\left(n + \frac{1}{2}\right)^2 \left[1 - \frac{2}{\left(n + \frac{1}{2}\right)\pi}\right]$	

are presented. In order to generate the results, the numerical values shown in Appendix I are used.

The natural frequencies of the clamped panel have been calculated, by using the following approximate formula, which is based on an energy (Raleigh) technique [Blevins, 1979].

$$f_{ij} = \frac{\pi}{2} \sqrt{\frac{D}{\rho_p t_p} \left[\frac{G_i^4}{L_{xp}^4} + \frac{G_j^4}{L_{yp}^4} + \frac{2H_i H_j}{L_{xp}^2 L_{yp}^2} \right]}, \quad i = 1, 2, 3, \dots, \quad j = 1, 2, 3, \dots \quad (3.79)$$

where the dimensionless parameters G and H , given in Table 3.2; these parameters are functions of the indices i (in x direction) and j (in y direction) and the boundary

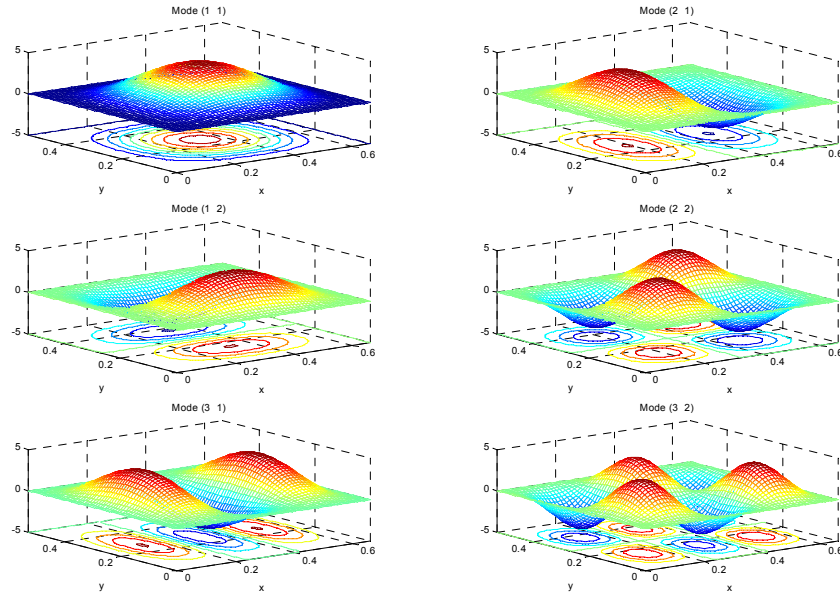


Figure 3.3. Numerical predictions of the first six mode shapes of the flexible panel.

conditions of the plate. The enclosure natural frequencies are calculated through the following equation.

$$f_{ijk} = \frac{c_0}{2\pi} \sqrt{\left(\frac{l_i\pi}{L_{xc}}\right)^2 + \left(\frac{m_j\pi}{L_{yc}}\right)^2 + \left(\frac{n_k\pi}{L_{zc}}\right)^2}, \quad (3.80)$$

$$i = 0,1,2,\dots, \quad j = 0,1,2,\dots, \quad k = 0,1,2,\dots,$$

where the indices l_i , m_j , and n_k are associated with the spatial functions of the i^{th} rigid enclosure mode, along the x , y , and z directions, respectively. Based on Eqs. (3.79) and (3.80), the first few natural frequencies of the “uncoupled” panel and enclosure systems are tabulated in the second and third columns of Table 3.3. In addition, based on Eqs. (3.10), (3.42), (3.43), and (3.48), the determined graphical representations for the

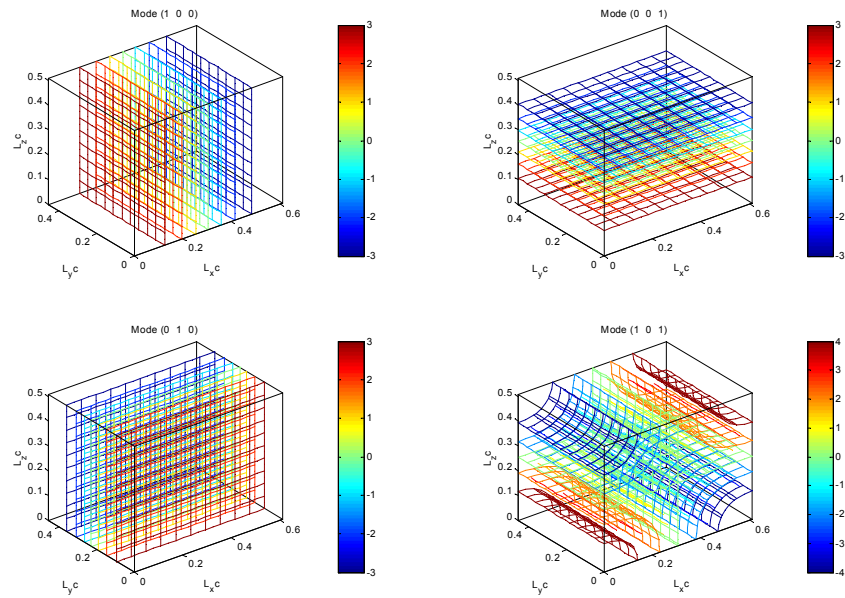


Figure 3.4. Numerical predictions of the first four acoustic mode shapes of the enclosure.

first few vibration mode shapes of the flexible panel and acoustic mode shapes of the enclosure are shown in Figure 3.3 and Figure 3.4, respectively.

Numerical results obtained for the mass and stiffness matrices of the coupled system (Eq. (3.54)) show how the vibration and acoustic fields interact with each other. Consideration of the first five (uncoupled) vibration modes and the first three (uncoupled) acoustic modes results in the following mass matrix

$$\mathbf{M} = \left[\begin{array}{ccccc|ccc}
4.4 & 0 & 0 & 0 & 0 & 0 & 0 & 0 \\
0 & 4.4 & 0 & 0 & 0 & 0 & 0 & 0 \\
0 & 0 & 4.4 & 0 & 0 & 0 & 0 & 0 \\
0 & 0 & 0 & 4.4 & 0 & 0 & 0 & 0 \\
0 & 0 & 0 & 0 & 4.4 & 0 & 0 & 0 \\
\hline
0 & -1.8 & 0 & 0 & 0 & 9 \times 10^{-6} & 0 & 0 \\
1.9 & 0 & 0 & 0.8 & 0 & 0 & 9 \times 10^{-6} & 0 \\
0 & 0 & -1.8 & 0 & 0 & 0 & 0 & 9 \times 10^{-6}
\end{array} \right] \quad (3.81)$$

$\begin{matrix} \uparrow & \uparrow & \uparrow & \uparrow & \uparrow & \uparrow & \uparrow & \uparrow \\ (1,1) & (2,1) & (1,2) & (3,1) & (2,2) & (1,0,0) & (0,0,1) & (0,1,0) \end{matrix}$

An important feature in the mass matrix is that the vibration mode (2,2) is uncoupled from all the included acoustic modes (please refer to the entries of the fifth column in Eq. (3.81)). The stiffness matrix also has the form shown in Eq. (3.82). The numerical values obtained for another case are shown in Appendix II.

$$\mathbf{K} = \left[\begin{array}{ccccc|ccc}
2.3E5 & 0 & 0 & -5.4E4 & 0 & 0 & -3.00 & 0 \\
0 & 9.4E5 & 0 & 0 & 0 & 2.82 & 0 & 0 \\
0 & 0 & 1.8E6 & 0 & 0 & 0 & 0 & 2.86 \\
-5.4E4 & 0 & 0 & 2.7E6 & 0 & 0 & -1.30 & 0 \\
0 & 0 & 0 & 0 & 2.9E6 & 0 & 0 & 0 \\
\hline
0 & 0 & 0 & 0 & 0 & 25.56 & 0 & 0 \\
0 & 0 & 0 & 0 & 0 & 0 & 38.24 & 0 \\
0 & 0 & 0 & 0 & 0 & 0 & 0 & 47.22
\end{array} \right] \quad (3.82)$$

$\begin{matrix} \uparrow & \uparrow & \uparrow & \uparrow & \uparrow & \uparrow & \uparrow & \uparrow \\ (1,1) & (2,1) & (1,2) & (3,1) & (2,2) & (1,0,0) & (0,0,1) & (0,1,0) \end{matrix}$

Here in the stiffness matrix as well, the vibration mode (2,2) is uncoupled from all the included acoustic modes (please refer to the entries of the fifth row in Eq. (3.82)). As shown in Figure 3.3, the effect of this mode may be explained as if there were four piston speakers distributed over the panel quarters and vibrating in opposing phase. This generates a dipole effect, resulting in destructive sound fields inside the enclosure.

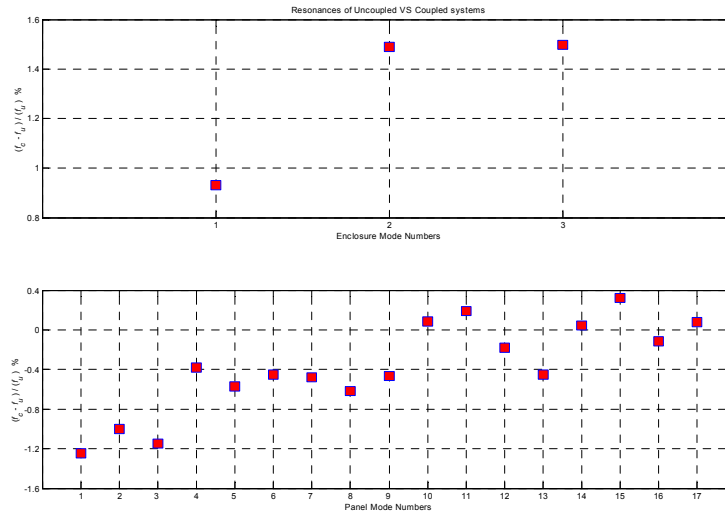


Figure 3.5. Percentage differences in resonance frequencies among the uncoupled and coupled cases.

Through further investigations into the mass and stiffness matrices of Eqs. (3.81) and (3.82) as well as in Appendix II, one can determine to the following:

- The acoustic fundamental mode (1,0,0) is affected only by the even \times odd panel vibration modes, such as mode (2,1).
- The acoustic mode (0,1,0) is affected only by the odd \times even panel vibration modes, such as mode (1,2).
- The acoustic mode (0,0,1) is affected only by the odd \times odd panel vibration modes, such as mode (1,1).

Plots of the vibration mode shapes given in Figure 3.3 can also be used to understand these correlations.

Table 3.3. Numerical predictions of the first few undamped natural frequencies (in Hz) of the panel and enclosure in the uncoupled and coupled cases.

Mode	Uncoupled System		Coupled system	Percentage Difference
	Panel	Enclosure		
(1,1)	41.6	–	40.9	1.7
(2,1)	73.7	–	72.4	1.8
(1,2)	95.0	–	93.3	1.8
(2,2)	124.6	–	123.1	1.2
(1,0,0)	–	281.3	282.6	-0.5
(0,0,1)	–	337.6	342.3	-1.4
(0,1,0)	–	375.1	380.5	-1.4
(1,0,1)	–	439.5	440.2	-0.2
(1,1,0)	–	468.9	472.2	-0.7
(0,1,1)	–	504.7	507.2	-0.5
(1,1,1)	–	577.8	580.3	-0.4

The natural frequencies of the undamped, coupled system can be calculated from the free undamped version of Eq. (3.70), that is,

$$\omega = (\text{Eigenvalues}[M^{-1}K])^{1/2} \quad (3.83)$$

The natural frequencies of the coupled panel-enclosure system, calculated using Eq. (3.83), are also tabulated in Table 3.3 along with the percentage differences among the resonance frequencies of the uncoupled and coupled cases. Due to the complexity of the structural-acoustic coupling of this system, the effect of the stiffness coupling matrix \mathbf{K}_{pc} and the inertia coupling matrix \mathbf{M}_{cp} on the coupled natural frequencies cannot be easily seen. In fact, the entries of \mathbf{M}_{cp} increase the values of the first three acoustic resonance frequencies above their uncoupled values, hence, contributing a “mass reduction” effect, whereas the entries of \mathbf{K}_{pc} decrease the values of the low (vibration) resonance frequencies below their uncoupled values, hence, contributing a “stiffness reduction” effect. In Figure 3.5, the percentage changes in resonance frequencies are graphically shown for the first three acoustic modes and seventeen vibration modes.

The spatial integrations in Eqs. (3.67) and (3.71) are frequency dependent. Numerical values of these integrations can be obtained by considering the Taylor series expansion of the term $[e^{-jkr}/r]$ about the nominal value $r \approx R$. This leads to

$$\begin{aligned} \frac{e^{-jkr}}{r} &\approx \frac{e^{-jkr}}{R} \left\{ \left[3 + 2jkR - \frac{1}{2}(kR)^2 \right] + \left(\frac{r}{R} \right) \left[-3 - 3jkR + (kR)^2 \right] \right. \\ &\quad \left. + \left(\frac{r}{R} \right)^2 \left[1 + jkR - \frac{1}{2}(kR)^2 \right] \right\} + O(r-R)^3. \end{aligned} \quad (3.84)$$

It is noticed here that when the separation $|r-R|$ approaches zero, which is the acoustic far field condition, this term reduces to $[e^{-jkR}/R]$, which can be also obtained by considering a plane wave instead of a spherical wave. In Eq. (3.84), the frequency-dependent terms enclosed in the square brackets have high-pass filter structures; that is, they filter the spatial integrations in Eqs. (3.67) and (3.71) based on the proximity of the flexible panel to the reference microphone and the noise source. This shows why the wave propagation resulting from the vibrations of the panel cannot be accurately analyzed as a plane wave if the spatial separations between the panel, the observation point, and the noise source are not “far” enough.

For more accurate results, the values in Eq. (3.67) and (3.71) are obtained by first performing numerical integrations over the area of the flexible panel at discrete frequencies along the frequency span $0 \leq f \leq 1000$ Hz, and later using an identification algorithm to approximate the frequency response. It has been noticed that the spatial coefficients $C^{(op)}$ can be approximated to the form

$$C_i^{(op)} \approx A_{pri} e^{-j\omega T_{pri}}, \quad (3.85)$$

where A_{pri} are the magnitudes of the response at the observation point with respect to the second temporal derivative of the i^{th} modal coordinate of the panel, and T_{pri} are the associated time delays (please refer to Eq. (3.66)).

For the numerical results given here, the observation point is located at the reference microphone, which is located along a vertical line passing through the mid point of the flexible panel. At this location, the only modes contributing to the pressure field at the

observation point are the odd×odd modes, and the effect of other modes is almost negligible, again, because of the dipole effect of the odd×even and even×odd vibration modes at all points along that vertical line. From the numerical results, it turns out that the phase delays T_{pri} in sensing the different modal functions have almost the same value, with a difference less than $\pm 40^\circ$ over the frequency span mentioned above. The values of A_{pri} vary significantly from one mode to another. However, each of the magnitude values is nearly independent of frequency; a maximum change of ± 1.5 dB is predicted over the frequency range of $0 \leq f \leq 1000$ Hz. In Figure 3.6, a comparison among the numerical results of $C_i^{(op)}$ of the odd×odd modes within the first 17 vibrations modes are shown; each value is normalized to have an average magnitude of unity, and the 8th order Padé approximation is used for the time delay function of the form

$$C_0^{(op)} \approx e^{-j\omega T_{pr}}, \quad T_{pr} = 1.7 \text{ ms.} \quad (3.86)$$

This function is plotted in Figure 3.6 with a straight line. It can be seen from the figure that this delay function approximates the numerical results well. Based on the system identification procedure, the row vector $\mathbf{C}^{(op)}$ has been chosen to be

$$\mathbf{C}^{(op)} = e^{-0.0017j\omega} \begin{bmatrix} 49.068 & 0.000 & 0.000 & 21.266 \\ 0.000 & 0.000 & 20.955 & 0.000 \\ 0.000 & 0.000 & 9.065 & 0.000 \\ 0.000 & 0.000 & 0.000 & 0.000 \end{bmatrix} \quad (3.87)$$

In comparison to a plane wave propagation, the time delay T_{pr} corresponds to a distance of 56.61 cm, which is 5.81 cm longer than the vertical separation between the observation

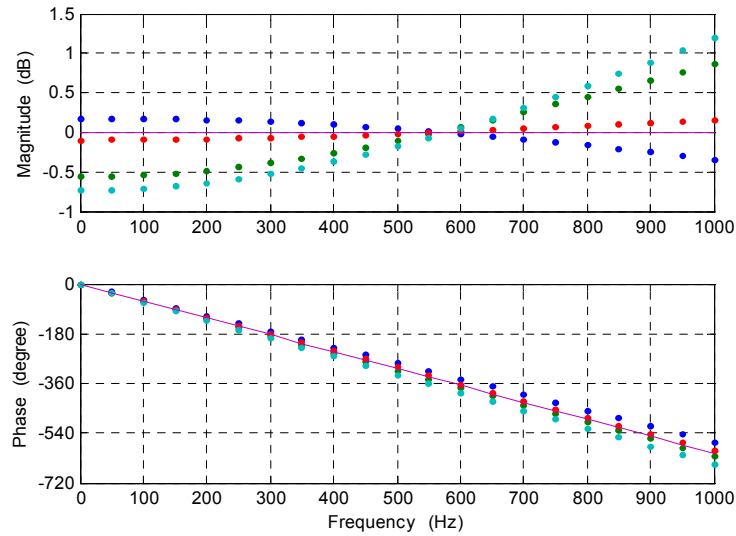


Figure 3.6. Comparisons between the 8th order Padé approximation of Eq. (3.86) (straight line) and the numerical results of $C_i^{(op)}$, which are calculated for odd×odd modes with the first 17 vibrations modes; the numerical results are normalized to have an average magnitude of unity (dotted line).

point and the panel. It is mentioned here that the time delay associated with the vertical separation between the observation point and the panel is 1.5 ms, compared to 1.7 ms predicted by the current model.

The excitation of the panel due to the noise source is also obtained by first numerically carrying out the spatial integration in Eq. (3.71) at discrete frequencies along the frequency span $0 \leq f \leq 1000$ Hz, and later by using an identification algorithm to approximate the frequency response. As was discussed earlier for Eq. (3.84), each entry in the frequency-dependent vector \mathbf{F}_a is expected to be a time-delay effect filtered

through a high pass filter and multiplied by a constant that depends on the spatial location of the panel with respect to the noise source. From the definition of \mathbf{F}_p in Eq. (3.55i), only the odd \times odd modes can be excited by plane wave excitations. As the excitation frequency increases, the plane wave approximation is no longer valid and, hence, the even \times odd modes also get excited. Therefore, the entries of \mathbf{F}_a that correspond to the even \times odd modes are expected to have high-pass-filter transfer functions, and the entries that correspond to the odd \times odd modes are expected to have pure delays with different magnitudes. The frequency-dependent entries of \mathbf{F}_a , which correspond to the first seventeen vibration modes, are compared with the analytically identified ones and represented graphically in Appendix IV. Based on the numerical results, the time delay in \mathbf{F}_a equals 2.6 ms, which corresponds to 89.91 cm distance; 2.28 cm longer than the physical separation r_{sp} .

The overall system can be now represented in the block diagram shown in Figure 3.7.

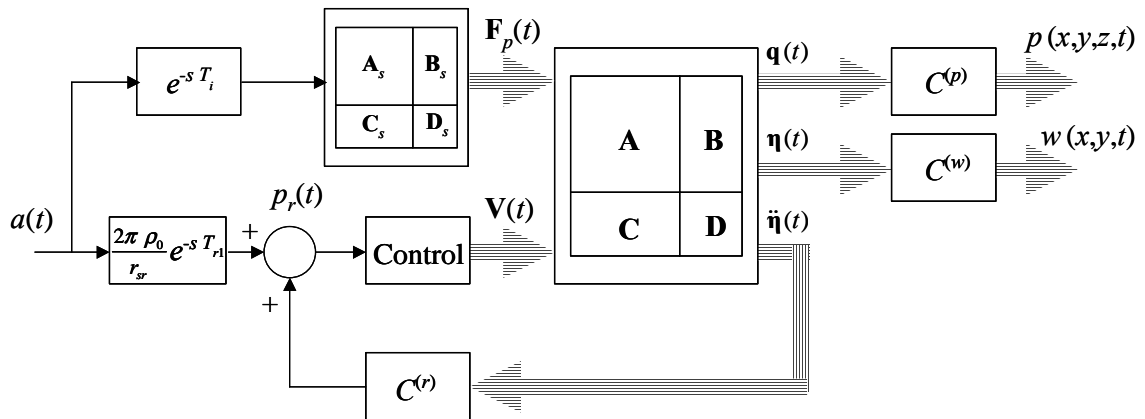


Figure 3.7. Overall system block diagram.

The numerical value for T_{op1} , according to Eq. (3.62), is 1.1 ms.

The numerical results are compared to the experimental measurements. It has been noticed that there are two main sources of phase delays, namely, a) the phase delays associated with the acoustic wave propagation inside and outside the enclosure and b) the phase delays associated with the microphones' acoustic chambers and electronics. While the former source is taken into account in the model developed here, the later one has to be identified experimentally and included in the corresponding analytical transfer functions.

3.2. Experimentally Identified Model

Here, unlike the analytical study presented in Section 3.1, an experimental approach is used to develop the system model by determining the various system transfer functions. The input signals, which are the voltage inputs to the loudspeaker and the nine PZT patch pairs, were applied to the system individually, and then, the experimental output signals from the various microphones and PVDF sensors were acquired and conditioned. These measurements are used as a basis to determine a state space model. Locations and orientations of collocated and error microphones are also examined in order to find an arrangement that is best suited for implementing the control schemes.

The *ARX SMART ID*TM software is used to predict the model state space matrices from the experimental frequency-response data. This software allows use of an *initial* state-space model as a starting point, and here, the analytical model developed in Section 3.1 is used for the starting point. It has been noticed that a state space model with 34 states effectively captures the dynamics of the system in the frequency range $100 \leq f \leq 200$ Hz

compared with a 48-state model with no pre-defined starting point. Therefore, the identification software was constrained to this maximum number of states. It is important to mention that this number of states is more than twice the number of states needed by the analytical model over the same frequency range. (The analytical model needs 16 states to address this frequency range.) As shown later in Section 3.4, the analytical model can predict the system dynamics in the frequency range $0 \leq f \leq 400$ Hz with 54 states.

Before proceeding further, the different functions and signals are assigned labels. The acoustic output signal of the loudspeaker (noise source) is labeled as $w(t)$, and the acoustic signals at the reference microphone and error microphones are labeled as $y(t)$

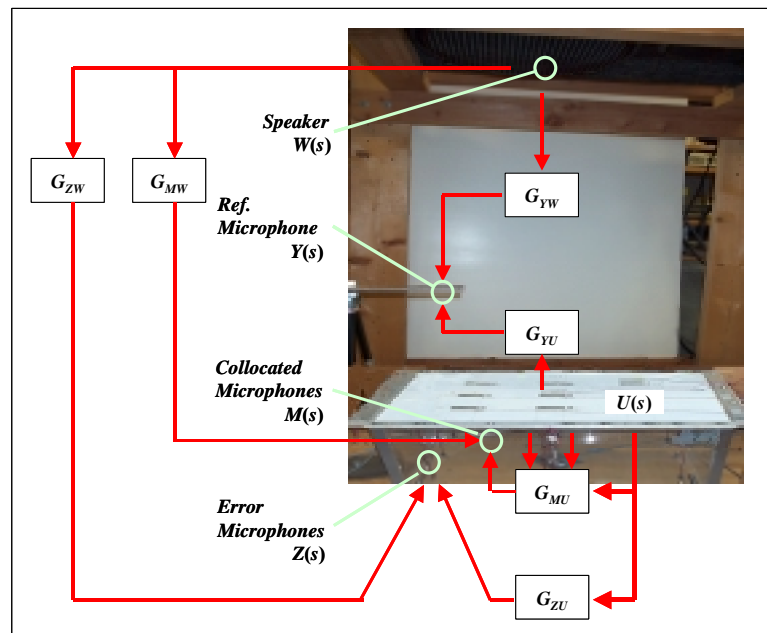


Figure 3.8. Photograph of the loudspeaker-panel-enclosure arrangement showing the various transfer functions.

and $z(t)$, respectively. The voltage signal fed to a PZT patch pair is labeled as $u(t)$. The different transfer functions are labeled as G_{ij} , where the index i indicates the output associated with the transfer function and j indicates the input associated with the transfer function. For example, the transfer function from the loudspeaker to the reference microphone will be referred to as G_{YW} . Recalling Figure 2.1 and making use of the various transfer functions defined, the overall system may be represented as shown in Figure 3.8. The concept of the collocated microphones, mentioned in this figure, will be discussed later in the next chapter.

3.3. Limitations of Analytical and Experimentally Identified

Models

As was mentioned above, the analytical model developed in Section 3.1 is capable of handling the wave distribution inside the three-dimensional enclosure, and it can also be used to study the cases where the pressure distribution on the flexible panel is not uniform, which is the case for spherical waves as well as for plane waves with incident angles. However, this model has the following limitations. The modeled acoustic pressure field inside the enclosure does not depend directly on the piezo-actuator induced vibrations as well as the direct transmission of external pressure waves through the panel. These two sources can have a significant influence on the internal pressure field at very high frequencies [Yi, Ling, and Ying, 2001]

In the analytical model, it is also assumed that all of the PZT patches have exactly the same characteristics; hence, for a symmetric patch pair, the actuation is in the form of pure bending only. The manufacturer's data for the PZT patches used in the experiments

indicates that the characteristics can vary within a range of $\pm 20\%$ of the nominal value [Morgan Electro Ceramics, Inc.], meaning that the difference between a PZT and the other in the same pair can be as large as 40%, resulting not only in bending effects, but shear effects as well. To investigate this point, experimental measurements were conducted to test the capacitance constant of each of the PZT pairs and compare it with the nominal value (based on the characteristics given by the manufacturer and tabulated in Table 2.1). To calculate the nominal value, the following equation was used [Chopra, 2000].

$$C = 2 \frac{(K_{33}^{\sigma}) e_0 L_{xpzt} L_{ypzt}}{h_{pzt}}, \quad (3.88)$$

where C represents the capacitance constant of the PZT pair, and the factor of 2 is used to calculate for the actuator pair and for the drive input arrangement shown in Figure 2.2(b); the PZT patches in a pair are connected in parallel. These experimental measurements are

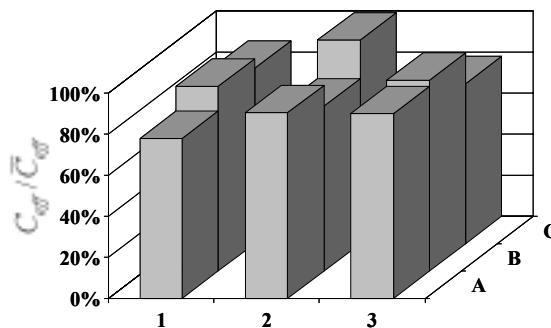


Figure 3.9. Measurements of capacitance constants for the PZT pairs as percentages of the nominal value. Each pair is defined by its x and y indices; e.g., A1, B2, etc.

Table 3.4. Percentage values of the measured capacitance constants of the PZT pairs relative to the nominal value.

A1	77.95%	A2	90.26%	A3	90.03%
B1	89.95%	B2	80.25%	B3	92.91%
C1	85.53%	C2	99.30%	C3	78.03%

plotted in Figure 3.9 and tabulated in Table 3.4. The capacitance values change by about 22% from the nominal value, and this change is not included in the analytical model.

The analytical model considers the induced strain of a PZT-5H patch to be linearly dependent on the input voltage. Experiments have been conducted to examine the strain behavior of a PZT patch identical to these patches used in the experimental arrangement. In these experiments, a strain gage was bonded to the surface of a free PZT patch to measure the surface strain while a DC voltage was input into the PZT patch quasi-statically from +0 to +120V and then from -0 to -120V. In Figure 3.10, a picture of a PZT patch with the strain sensor is shown, and in Figure 3.11, the strain measured by the strain gage is plotted versus the voltage input into the PZT patch. These values are also tabulated in Appendix V. The experimental results show that the free-strain at the PZT surface is linear for “small” range of voltages and it starts to deviate from a linear behavior at higher voltages, where the difference between the measured to the analytical values exceeds 16% at voltage magnitudes higher than 80 volts. Since all control algorithms presented in this work deal with the system as a linear system, it needs to be

noted that the control voltage needs to be restricted to be below an upper bound, in order to consider the PZT patches as linear actuators. (For studies about the nonlinear behavior of the PZT patches, please refer to Balachandran and Zhao (2000).)

The model needs to be modified to handle another enclosure system that does not fit exactly the geometric considerations and boundary conditions of the enclosure analyzed here. It is obvious that the more complicated the enclosure geometry is, the more difficult the analytical effort would be.

On the other hand, there are two main disadvantages of the experimentally identified model: first, the interconnections between the different elements of the system cannot be predicted, as is the case with the analytical model, except at the physical locations of the sensors and actuators; and second, as was mentioned earlier in Section 3.2, the experimentally identified model needs more number of modes to capture the system dynamics. Therefore, the analytical model is easier to implement for a real-time control

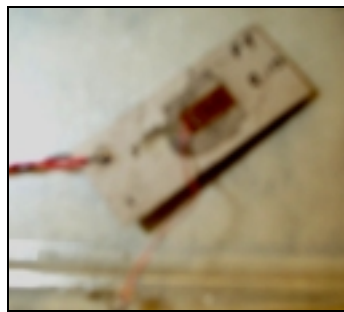


Figure 3.10. A PZT actuator patch with a strain gage used in the experiments.

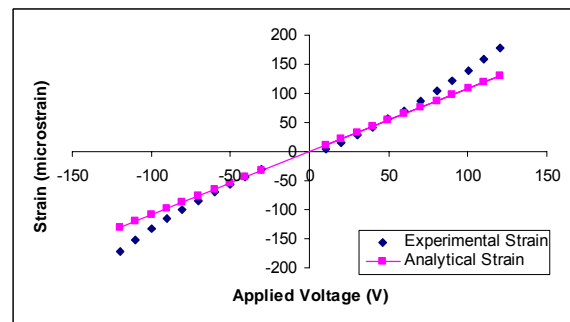


Figure 3.11. Analytical predictions and experimental measurements for the PZT-5H free strain.

scheme, especially when the time needed to run the control calculations is critical for the system performance, as in the case of feedforward ASAC systems.

However, there are three main benefits of this approach: first, the approach does not depend on the geometry and boundary conditions of the enclosure, hence, this approach can be useful for implementing the controller on full-scale sophisticated systems that are too difficult to analyze analytically, such as helicopter cabins; second, the developed experimental model can take into account setup and manufacturing imperfections that the analytical model cannot; and third, the experimentally identified system captures the (linear) dynamics of all the components of the experiment, such as the power supplies,

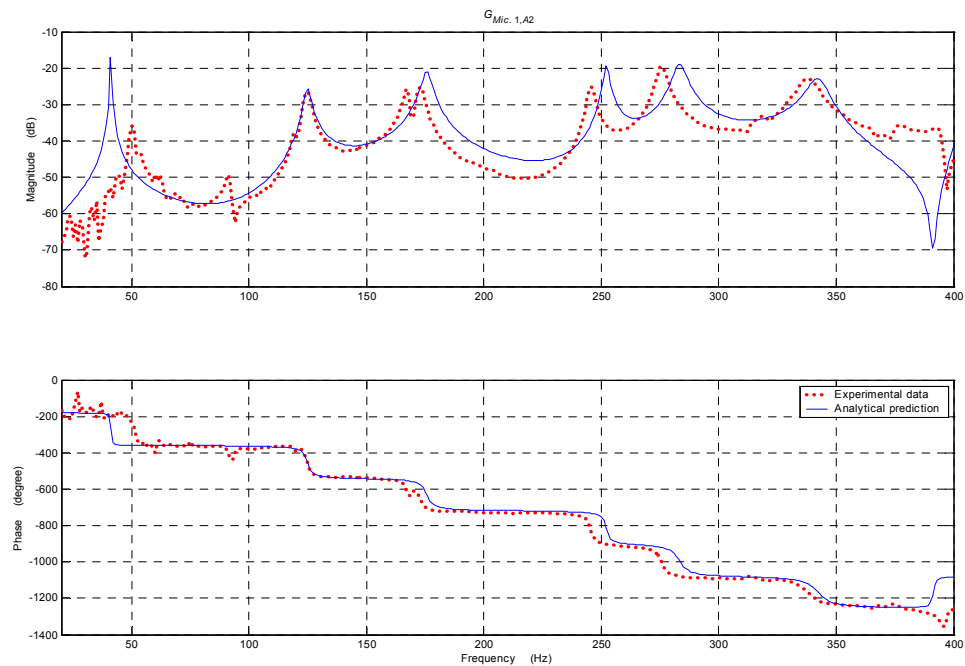


Figure 3.12. Frequency-response plot of the transfer function $G_{Mic_1,A2}$.

amplifiers, and signal conditioners. For these reasons, this approach is expected to give good results as long as the nonlinear effects are negligible.

3.4. Comparisons with Experimental Results

In this section, the numerical results obtained from the analytical model and the experimentally identified model are compared with the experimental results. In Table 3.5, the numerical values of the natural frequencies of the first 14 system modes are compared with the experimental data. These modes include twelve structural modes and two acoustic modes. The numerical results from the analytical model show good agreement with the experimental results. Furthermore, the numerical results obtained from the analytical model are compared to the experimentally obtained frequency-response functions in Figure 3.12 through Figure 3.18, where the analytical model result are illustrated by solid lines and the experimental data are illustrated by dashed lines. In each case, the nomenclature $G_{y,x}$ is used to represent the transfer function between the output y and the input x . The inputs in these figures are either the acceleration of the speaker diaphragm, a_s , or the voltage input to one of the PZT patch pairs; the labels are as explained in Chapter 2. The outputs are the pressure signal at the reference microphone and the pressure signals at the microphones Mic.1 and Mic.3.

To generate the analytical predictions, the first 27 modes were considered. These modes include 22 panel modes and 5 enclosure modes. The resonance frequencies associated with these modes lie in a frequency span extending up to 500 Hz, with the highest resonance frequency being 495.75 Hz. To obtain the experimental data, white noise voltage signal was used as the excitation signal and the results obtained are shown over a 400 Hz bandwidth. Since the highest resonance frequency of the included modes is 495.75 Hz, the contribution of the unmodeled modes is insignificant in this frequency range. The frequency-response values for frequencies less than 20 Hz could not be realized due to the limitations of the equipment used in the experimental arrangement.

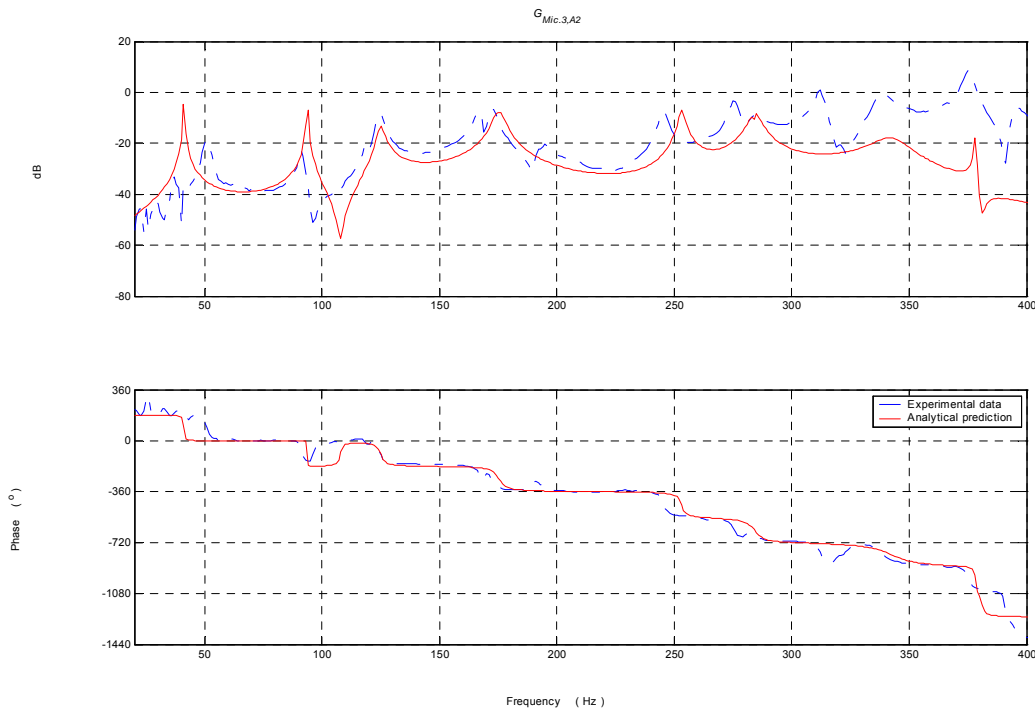


Figure 3.13. Frequency-response plot of the transfer function $G_{Mic3,A2}$.

While the results shown in Figure 3.12 through Figure 3.14 illustrate the panel interactions with the enclosed sound fields, the results shown in Figure 3.15 illustrate the panel interaction with the external sound field and the results shown in Figure 3.16 through Figure 3.18 illustrate the interactions between the three system components: the external sound fields, the panel, and the enclosed sound fields. The graphs indicate a good match between the experimental and numerical results. From the comparisons, it is clear that the derived analytical model does not perfectly capture the stiffness contribution at the frequency associated with the resonance of the first mode. It is believed that this difference may arise due to the assumption of weak structural acoustic coupling considered in the mathematical model, which may not be valid in the low frequency range. The differences at the other resonance frequencies are within 5%, which is in the accuracy range of the approximated clamped plate equations [Blevins, 1979].

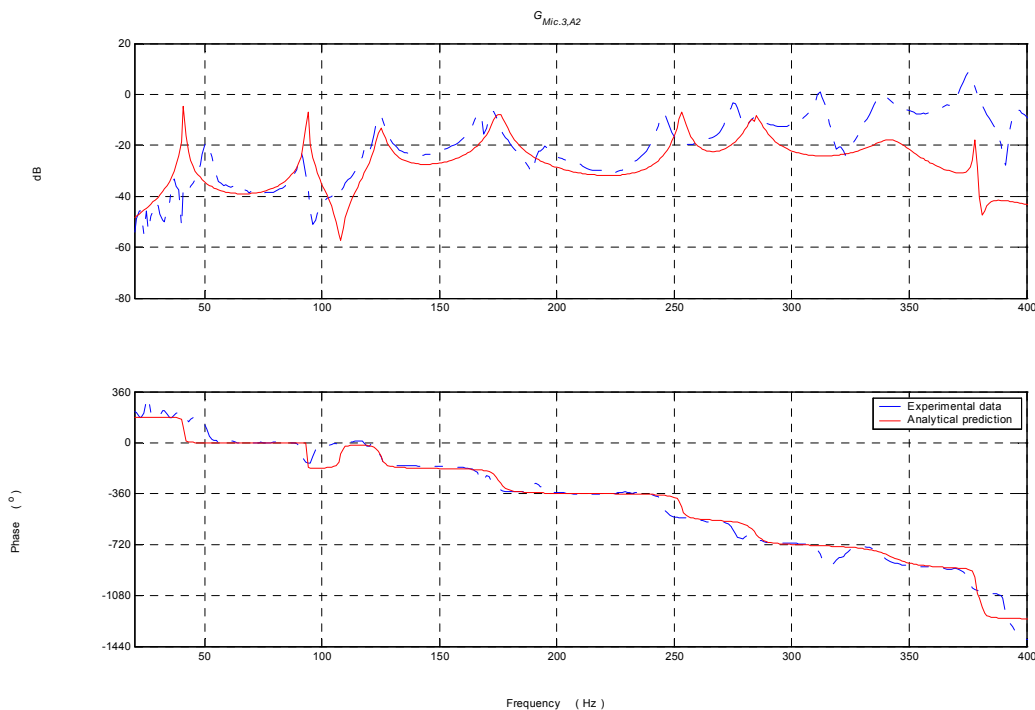


Figure 3.14. Frequency-response plot of the transfer function $G_{Mic3,A2}$.

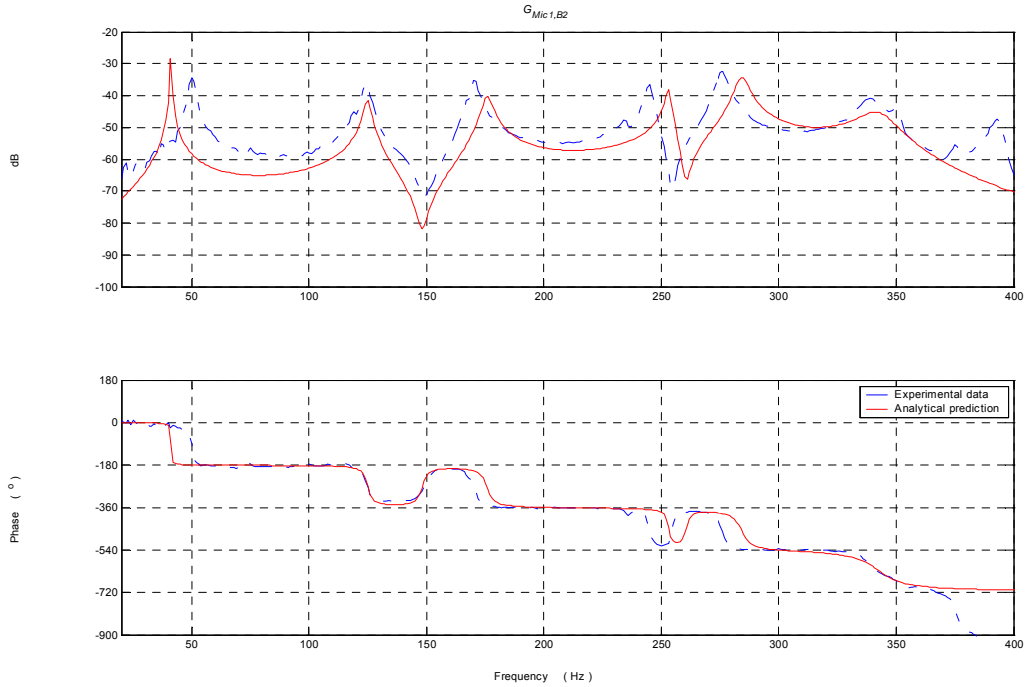


Figure 3.15. Frequency-response plot of the transfer function $G_{Mic1,B2}$.

For the different frequency-response functions considered, the model captures the phase information well. This indicates that the model developed here is suitable for model based feedforward control schemes, where phase information is important.

The effect of the spherical wave propagation is clear when comparing the pressure field results at the microphone location Mic.3 for the cases of plane wave and spherical wave incidence; these results are shown in Figure 3.18 and Figure 3.19. In Figure 3.18, the excitation of the vibration modes with even indices (such as mode (2,1) at 73.7 Hz and mode (4,3) at 319.5 Hz) and the acoustic modes with nonzero x and y indices (such as mode (1,0,0) at 281.3 Hz and mode (0,1,0) at 375.1 Hz) is predicted. As was mentioned before in Section 3.1.3, these modes cannot be excited by plane wave incidence; this is illustrated by the results shown in Figure 3.19.

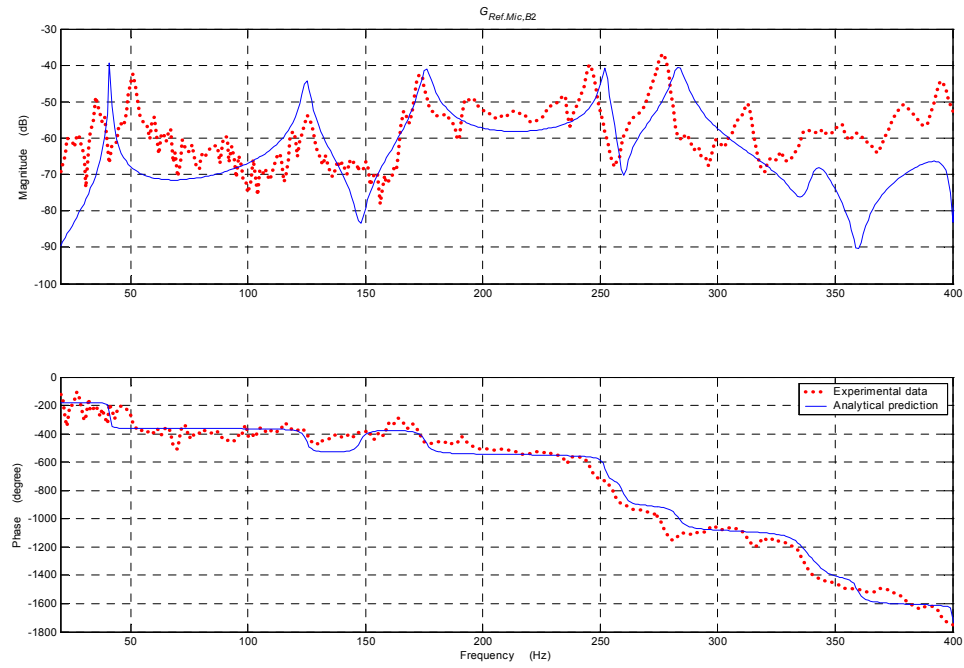


Figure 3.16. Frequency-response plot of the transfer function $G_{RefMic,B2}$.

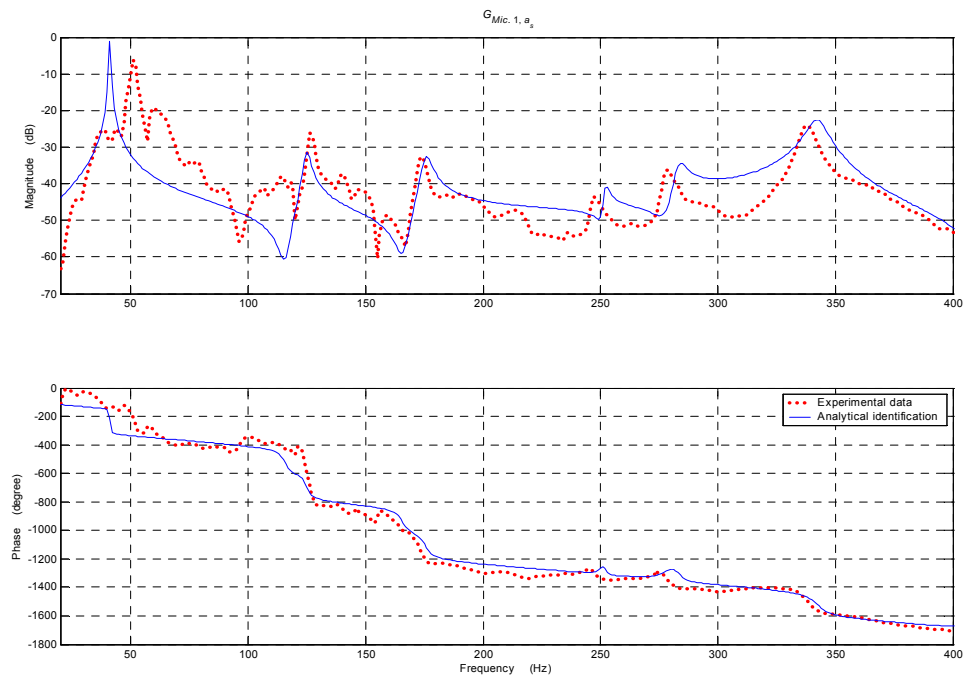


Figure 3.17. Frequency-response plot of the transfer function G_{Mic1,a_s} .

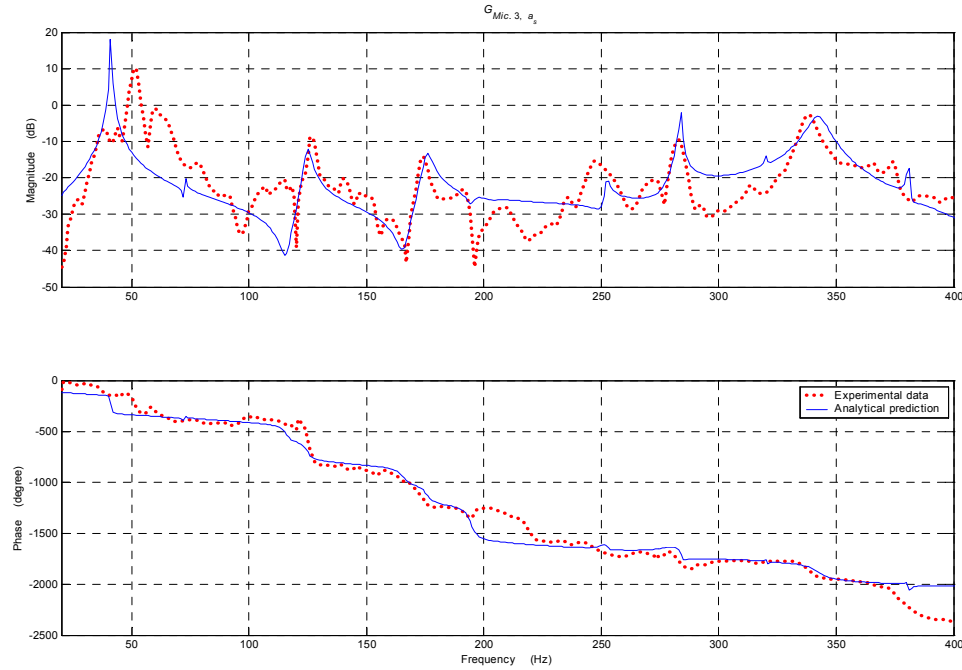


Figure 3.18. Frequency-response plot of the transfer function G_{Mic3,a_s} .

Comparing with the experimental results, one can see that the spherical wave modeling is essential to predict the phase changes. As seen in Figure 3.17, the even-indexed vibration modes are not predicted at the location of the microphone Mic.1, due to its symmetric location with respect to the panel; however, the vibration mode (1,0,0) is predicted as a result of taking the spherical wave modeling into account.

It is also mentioned here that the time delays associated with these predictions in both Figure 3.17 and Figure 3.18 are different from those associated with plane wave incidence, as the nominal values for R in Eq. (3.84) are different from the vertical separations among the sound source, panel, and observation point. For example, the time delay associated with Eq. (3.71) is 2.6 ms, corresponding to a separation of 89.91 cm,

Table 3.5. First few structural and acoustic resonance frequencies (in Hz):

Comparisons of the numerical predictions with the experimental data.

Mode	Numerical Prediction	Experimental Data	Percent
(1,1)	40.9	51.0	-22.2
(2,1)	72.4	74.0	-2.2
(1,2)	93.3	91.5	1.9
(2,2)	123.1	119.5	2.9
(3,1)	124.1	124.5	0.3
(1,3)	174.7	172.0	1.5
(4,1)	194.4	192.0	1.2
(2,3)	203.3	194.5	4.3
(4,2)	241.8	235.0	2.8
(3,3)	251.2	245.0	2.5
(5,1)	283.3	275.5	2.8
(4,3)	319.5	313.0	2.0
(0,0,1)	342.3	338.0	1.3
(3,4)	359.0	352.0	1.9
(0,1,0)	380.5	374.0	1.7
(5,3)	405.1	395.5	2.4

which is 2.28 cm larger than the vertical separation between the loudspeaker and the panel. This time delay difference cannot be predicted by using a plane wave approximation.

In Figure 3.20, the analytical prediction of the pressure field at the microphone location Mic.2 is shown in the cases of spherical wave modeling and plane wave modeling. It is clear from this figure that with plane wave modeling one cannot predict the participation of many vibration and acoustic modes, as reflected by both the magnitude and the phase results.

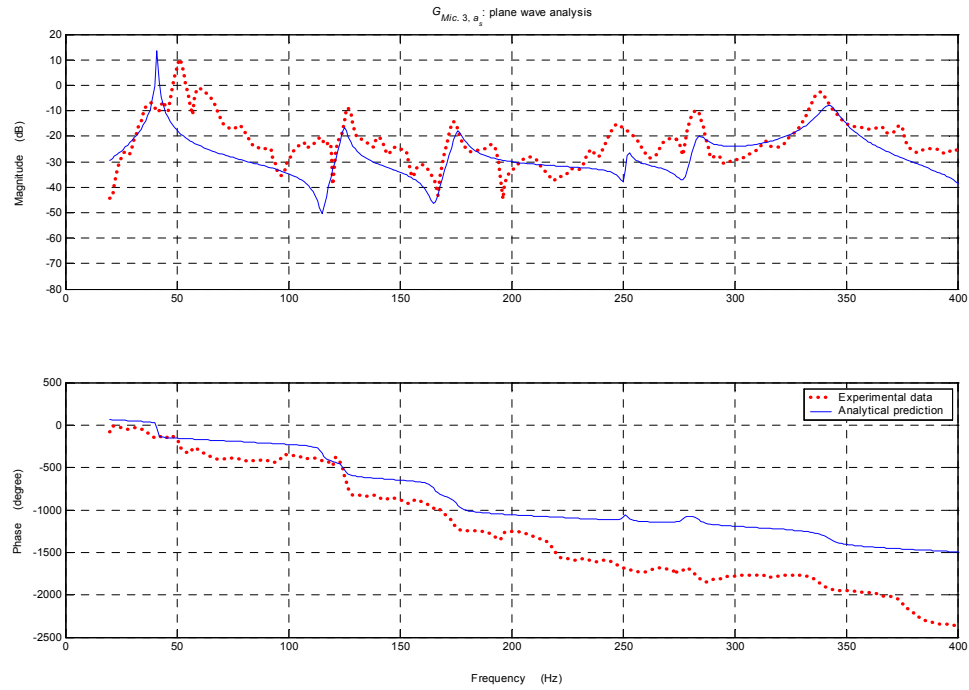


Figure 3.19. Transfer function $G_{Mic3,as}$: Comparison of the analytical plane-wave model result (continuous lines) with experimental data (dotted lines).

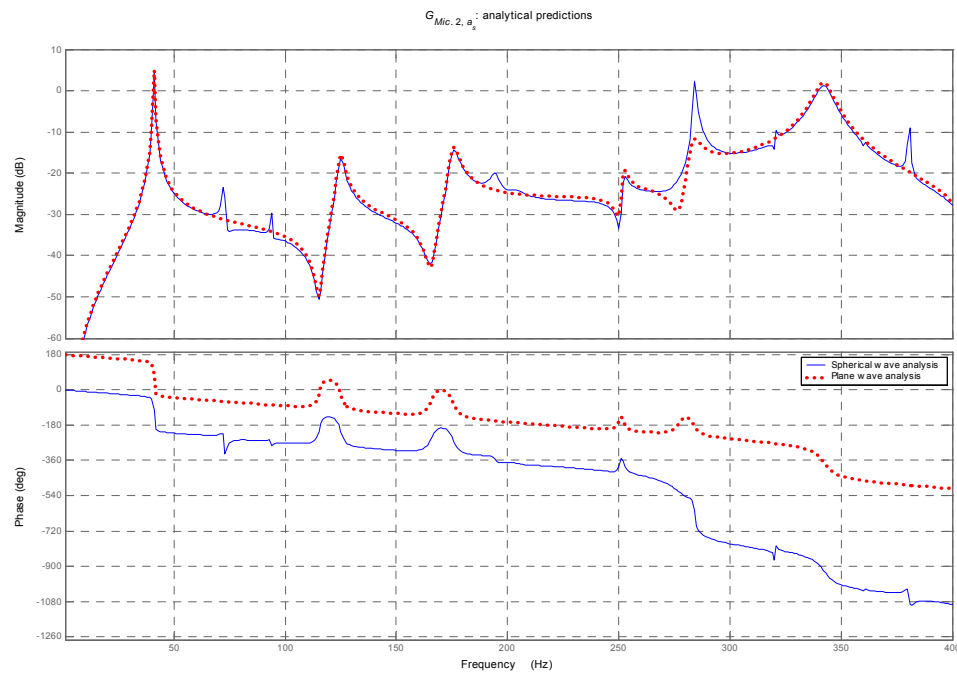


Figure 3.20. Transfer function G_{Mic2,a_s} : Model result from spherical wave analysis (continuous lines) versus model result from plane wave analysis (dotted lines).

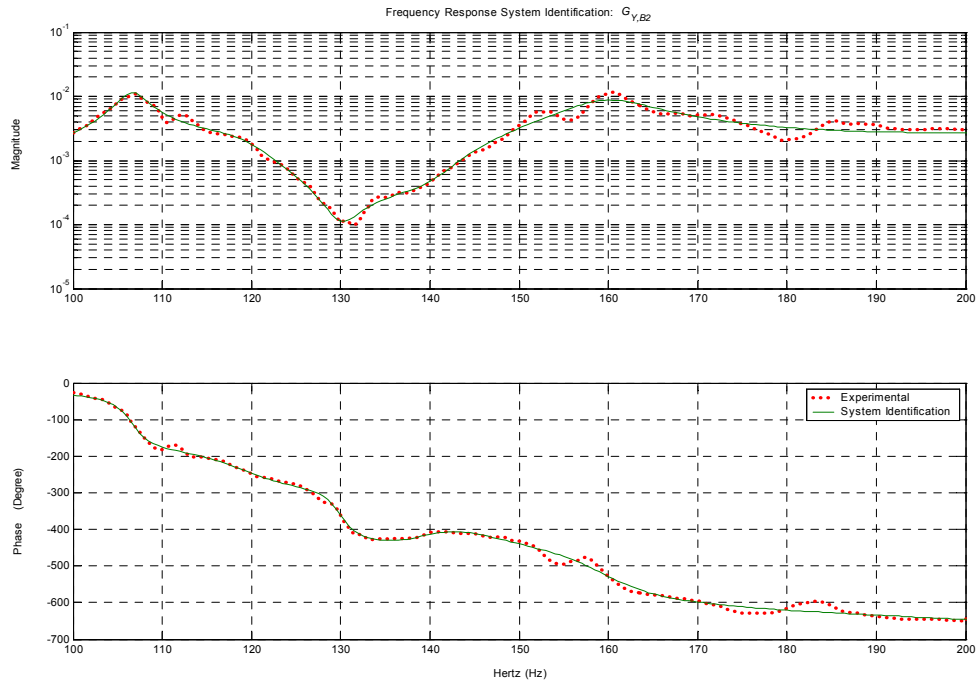


Figure 3.21. Experimental identification of the transfer function between the PZT patch B2 and the reference microphone.

In Figure 3.21, the experimental measurements of the frequency response of the transfer function G_{YU} is compared with the experimentally identified model. The phase changes are well captured by the identified model. The frequency response plots of different experimentally identified transfer functions are further provided in Appendix III.

4. Control Approaches

In this chapter, the two zero spillover feedforward schemes developed for a ASAC system are discussed. The objective of each of these schemes is to attenuate narrowband and broadband three-dimensional sound fields. As mentioned in Chapter 1, spillover is said to occur at a frequency ω , if the closed-loop transfer function magnitude is greater than the open-loop transfer function magnitude. The zero spillover control schemes presented here attempt to keep the acoustic pressure, and hence the acoustic potential energy, of the controlled system below that of the uncontrolled system over and beyond the frequency range of interest.

The control systems considered here are Single-Input Single-Output (SISO) systems, where the PZT pair patch B2 shown in Figure 2.2 is used as control actuator and the microphone Mic.1 shown in Figure 2.3 is used as the error microphone. The other PZT patches and microphones shown in these figures are used as performance sensors. The nomenclature used in Chapter 3 for the system states and transfer functions is also used here. The system dynamics at both reference and error microphones can be expressed as follows

$$\dot{\mathbf{x}}(t) = \mathbf{A} \mathbf{x}(t) + B_w w(t) + B_U u(t) \quad (4.1a)$$

$$z(t) = \mathbf{C}_p \mathbf{x}(t) \quad (4.1b)$$

$$y(t) = \mathbf{C}_r \mathbf{x}(t) + D_{rW} w(t) + D_{rU} u(t) \quad (4.1c)$$

$$\mathbf{x}(t) = \{\boldsymbol{\eta}(t) \quad \mathbf{q}(t) \quad \dot{\boldsymbol{\eta}}(t) \quad \dot{\mathbf{q}}(t)\}^T, \quad (4.1d)$$

where $u(t)$ is the voltage input to the PZT patch pair B2, $\boldsymbol{\eta}(t)$ and $\mathbf{q}(t)$ are panel and enclosure modal coordinates, respectively, $z(t)$ and $y(t)$ are the pressure fields measured at the error microphone and the reference microphone, respectively, and $w(t)$ is the acceleration of the speaker diaphragm $a_s(t)$. Equations (4.1a) can be transformed in the Laplace domain to the following:

$$\begin{pmatrix} Z(s) \\ Y(s) \end{pmatrix} = \mathbf{G}(s) \begin{pmatrix} W(s) \\ U(s) \end{pmatrix}, \quad (4.2a)$$

where

$$G(s) = \begin{bmatrix} G_{ZW}(s) & G_{ZU}(s) \\ G_{YW}(s) & G_{YU}(s) \end{bmatrix}. \quad (4.2b)$$

In Eqs. (4.2), s is the Laplace variable and $G_{kl}(s)$ is the transfer function between the input l and the output k . Further, the transfer function G_{YW} can be divided into two parts: $G_{YW1}(s)$ and $G_{YW2}(s)$, which are related to the pressure components $P_{op1}(s)$ and $P_{op2}(s)$ at the reference microphone through the following relations:

$$P_{op1}(s) = G_{YW1}(s) W(s) \quad (4.3a)$$

and

$$\begin{aligned} P_{op2}(s) &= G_{YW2}(s) W(s) + G_{YU}(s) U(s) \\ &= G_{Y\eta} \boldsymbol{\eta}(s) \end{aligned} \quad (4.3b)$$

For ANC systems that do not contain reflective surfaces, the first term in Eq. (4.3b) does not exist, and the inherent acoustic feedback is defined only through the second term. However, in ASAC systems, the inherent acoustic feedback contains both of the terms shown in Eq. (4.3b). Thus, there could be either constructive interference or destructive interference between the two components. This can be advantageous for system stability, since the reference microphone can be located at a region of destructive interference, at which the effect of the inherent acoustic feedback is minimal. In this work, as discussed in Section 5.3, the location of the reference microphone is chosen based on experimental observations.

The control action is constructed in the form

$$U(s) = G_C(s) Y(s) \quad (4.4)$$

where G_C is the controller transfer function. Equations (4.2) and (4.4) satisfy the general ANC block diagram shown in Figure 4.1 where the summation points represent the acoustic signals measured by the reference and error microphones.

Eliminating $U(s)$ from (4.2) and (4.4), the closed-loop transfer function becomes [Roure, 1985]

$$\bar{G}_{ZW}(s) = \frac{Z(s)}{W(s)} = F(s)S(s) \quad (4.5)$$

where $\bar{G}_{ZW}(s)$ is the transfer function between the noise source and the error microphone in the controlled case. In this equation, $F(s)$ is called *spillover function*, which depends on the physical arrangement of the measurement, control, and disturbance, and the function $S(s)$ is called *sensitivity function*, which depends on the loop transfer function $L(s)$. The expressions for these functions are as follows:

$$S(s) = \frac{1}{1-L(s)} \quad (4.6a)$$

$$F(s) = G_{ZW}(s)[1-L(s)] + G_{ZU}(s)G_C(s)G_{YW}(s) \quad (4.6b)$$

and

$$L(s) = G_{YU}(s)G_C(s). \quad (4.6c)$$

A zero spillover controller must guarantee that $|\bar{G}_{ZW}(s)| \leq |G_{ZW}(s)|$ in the frequency span

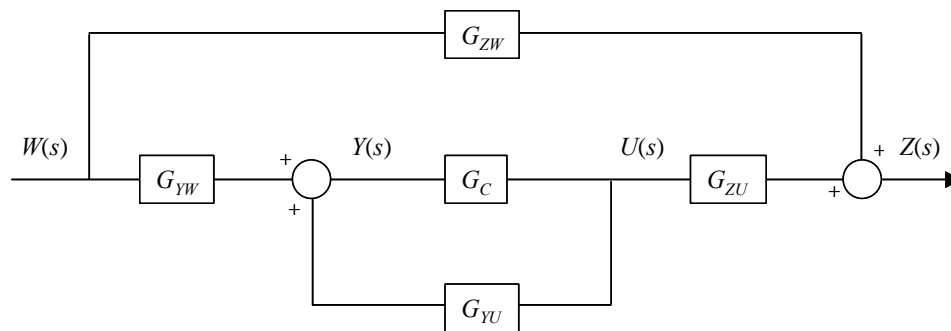


Figure 4.1. Typical ANC block diagram.

of interest. Two different approaches are conducted to satisfy this condition. The first approach is to solve for $F(s) = 0$ and get a controller transfer function that results in perfect quiet zones. This approach is an extension of the work carried out by Hong and Bernstein (1998). The novelty in the current work in the following: 1) the zero spillover control scheme is applied for controlling three-dimensional sound fields and 2) the zero spillover control scheme is integrated with active structural-acoustic control systems, where the control actuators are piezoelectric patches bonded to a flexible side of the enclosure. The controller that results from this approach will be labeled here as *Perfect Quiet Zone* (PQZ) controller.

The second approach is to relax the control constraints so as to get a reasonable reduction in noise over the frequency range of interest, while ensuring that spillover will not occur outside that frequency range. This controller will be labeled here as *Relaxed Zero Spillover* (RZS) Controller. To the best of the author's knowledge, this is the first time such a ASAC control scheme is reported in the literature. The design of both approaches will be detailed in the following two chapters, where simulation and experimental results are also presented.

5. Control Design and Implementation: PQZ Controller

In this chapter, the design of the Perfect Quiet Zone control scheme is described and details of the experimental implementation are presented. The implementation is based on the analytical model and the experimentally identified model discussed in Chapter 3. The frequency range used for the controller based on the experimentally identified model is limited to $100 \leq f \leq 200$ Hz, due to the large number of states needed for the model and the difficulty of running real time experiments with a large model. The controller based on the analytical model could be examined in real time over the wider frequency span of $30 \leq f \leq 230$ Hz; this is due to the reduced order of the analytical model and the explicit phase delay representations used in this model. System simulations using both controllers are presented later in this chapter along with the experimental results.

5.1. PQZ Control Design

As mentioned in Chapter 4, perfect quiet zones can result from setting the spillover function equal to zero. Revisiting Eq. (4.6b), the following expression can be obtained for the controller

$$G_{PQZ}(s) = \frac{G_{ZW}(s)}{G_{ZW}(s)G_{YU}(s) - G_{ZU}(s)G_{YW}(s)} \quad (5.1)$$

The above equation can also be obtained by requiring $Z(s) = 0$ in the block diagram shown in Figure 4.1. By examining equation (5.1), one can ascertain that the zero spillover controller cannot be realized if the denominator approaches zero. One case at which the denominator approaches zero is when either one of the following conditions is satisfied: 1) the disturbance source and the noise source are collocated, for which $G_{ZW}(s) = G_{ZU}(s)$ and $G_{YW}(s) = G_{YU}(s)$ and 2) the reference microphone and the error microphone are collocated, in which case $G_{ZW}(s) = G_{YW}(s)$ and $G_{YU}(s) = G_{ZU}(s)$. This leads to the two conditions set forth by Hong and Bernstein (1998) and discussed in Section 1.1 of this dissertation. Relocation and/or choice of actuators and sensors can be used to avoid this problem to a certain extent. To illustrate this point, the following two cases are considered: a) in this case, the external noise source is identified and a non-acoustical reference signal measured directly from that source (such as a voltage signal from a tachometer that measures the RPM speed of an engine) is used and b) in this case, an acoustical sensor is used to measure the noise signal and the setup of the acoustical source is chosen in such a way that the influence of the secondary source on it is negligible. In both of these cases, G_{YU} is equal to (or nearly equal to) zero. Such cases may be represented by the block diagram shown in Figure 5.1. The resulting simplified control transfer function is

$$G_{PQZ1}(s) = -\frac{G_{ZW}(s)}{G_{ZU}(s)G_{YW}(s)} \quad (5.2)$$

that can always exist (the control signal is expected to be bounded over the frequency

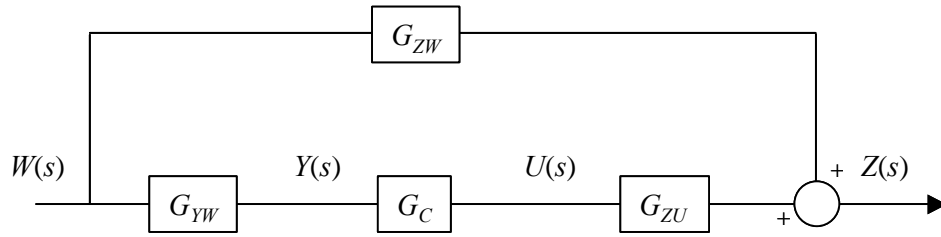


Figure 5.1. Simplified ANC block diagram where inherent feedback is zero (or negligible).

range of interest). If G_{ZU} and G_{YW} do not contain any nonminimum-phase zeros, this simplified control transfer function stabilizes the system. As stated previously, the locations of the actuators and sensors can be used to tailor the zero locations.

In some cases, for practical purposes, it is convenient to rewrite equation (5.2) as

$$G_{PQZ1}(s) = -\frac{G_{ZW}(s)/G_{YW}(s)}{G_{ZU}(s)} = -\frac{G_{ZY}(s)}{G_{ZU}(s)} \quad (5.3)$$

where G_{ZY} is the transfer function mapping from the reference microphone signal transform $Y(s)$ to the error microphone signal transform $Z(s)$, when subjected to the noise $W(s)$. This mapping can be constructed as long as the following two conditions are valid: (1) the acoustic path from the noise source to the reference microphone is shorter than that from the noise source to the flexible panel and (2) the pressure field component at the reference microphone due to the waves reflected back from the flexible panel is negligible. These two conditions simply ensure that the dynamics of G_{YW} is contained in G_{ZW} . In one-dimensional ANC systems such as ducts, only the first condition is needed to realize Eq. (5.3), which is always true given that the system involves reflective

boundaries. In the ASAC system of interest, this equation should be validated through the minimization of the inherent acoustic feedback, which will be addressed later in Section 5.2.1.

Now, in the context of active structural-acoustic control (ASAC) systems, the quantity $U(s)$ corresponds to the vibrations experienced by the structure as a result of actuators (secondary sources) bonded directly to that structure. If a near-located microphone is then installed inside the enclosure in the vicinity of the actuator, $U(s)$ can be mapped to the corresponding acoustic signal transform $M(s)$ through the transfer function from $U(s)$

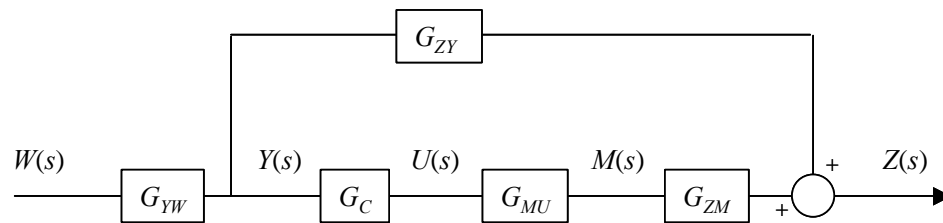


Figure 5.2. Block diagram for ASAC system with near-located microphone while the IAF is neglected.

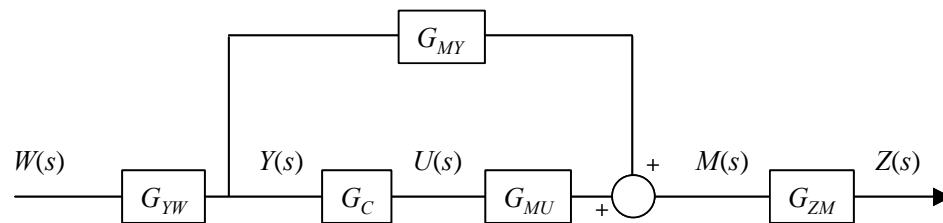


Figure 5.3. Simplified block diagram of ASAC system with near-located microphone.

to $M(s)$. In Figure 5.2, a block diagram is illustrated for this case, where all signal transforms correspond to acoustic pressure measurements at different locations, except $U(s)$ that corresponds to structural vibrations (e.g., surface acceleration).

Assuming that the influence of the system nonlinearities and the effects of three-dimensional wave propagation can be minimized, the primary path transfer function now can be constructed as a cascade given by

$$G_{ZY}(s) \cong G_{ZM}(s) G_{MY}(s) \quad (5.4)$$

So, the block diagram for the system under study can be simplified to the situation shown in Figure 5.3. From Eqs. (5.3) and (5.4), thus, in order to cancel out the noise at the error microphone, a controller transfer function of the form

$$G_{PQZ1}(s) = -\frac{G_{ZM}(s)G_{MY}(s)}{G_{ZU}(s)} = -\frac{G_{MY}(s)}{G_{MU}(s)} \quad (5.5)$$

suffices to realize zero spillover under the assumed conditions. In state-space realization, the controller transfer function has the form [Sánchez-Peña and Sznaier, 1998]

$$G_{PQZ1}(s) = \left[\begin{array}{cc|c} A & 0 & B_{MY} \\ -B_{MU}D_{MU}^{-1}C_{MY} & A - B_{MU}D_{MU}^{-1}C_{MU} & -B_{MU}D_{MU}^{-1}D_{MY} \\ \hline D_{MU}^{-1}C_{MY} & D_{MU}^{-1}C_{MU} & D_{MU}^{-1}D_{MY} \end{array} \right]. \quad (5.6)$$

To summarize, let us consider the system described by the block diagram shown in Figure 5.4. In the reconstruction shown in this figure, the pressure field at the reference microphone is defined as the superposition of two pressure fields, namely $Y_1(s)$ and $Y_2(s)$, and the transfer function G_{ZW} is composed in the form

$$G_{ZW}(s) = \bar{G}_{ZM}(s) G_{MY}(s) \bar{G}_{YW}(s) \quad (5.7)$$

and the following three assumptions are made:

1. Magnitude of G_{YU} is “small” so that

$$U(s) \cong Y_1(s), \quad (5.8a)$$

$$\bar{G}_{YW}(s) \cong G_{YW}(s), \quad (5.8b)$$

and

$$\bar{G}_{ZM}(s) \cong G_{ZM}(s) \quad (5.8c)$$

With the abovementioned assumptions, the zero spillover controller (5.1) reduces to (5.5).

It is mentioned here that this controller cannot stabilize the system unless the transfer

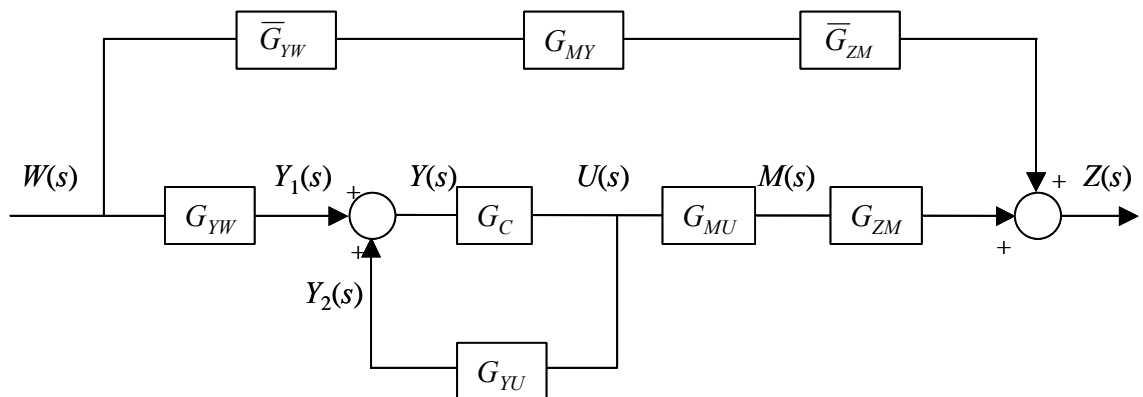


Figure 5.4. Reconstructed zero spillover controller for ASAC system.

function G_{MU} is minimum phase (i.e., there are no poles or zeros in the right-half plane of the s -domain). It is clear from equation (5.5) that the eigenvalues of $[A - B_{MU}D_{MU}^{-1}C_{MU}]$ must be stable for the entire system to be stable. In order to achieve this, the near-located microphones should be close to the actuators. If the spatial separation between an actuator and the corresponding collocated microphone is “small enough” that the propagating phase delay between them is “small”, the transfer function G_{MU} is most likely minimum phase. However, one has to ensure that the microphone does not spatially interfere with the structure’s vibrations.

Next, it will be shown how the assumptions (5.8) can be justified through analytical investigations into the inherent acoustic feedback and system stability and performance. Analytical and experimental justification of the PQZ controller will be discussed next, followed by simulation and experimental results.

5.2. PQZ Controller Justifications

In Section 5.1, it was discussed as to how the sensor locations can be chosen to satisfy the assumptions made during the controller development. From an analytical standpoint, the controller defined in Eq. (5.5) is supposed to give perfect cancellation of noise under the stated assumptions. However, since the model transfer functions do not always capture all of the system characteristics, and since the effects of the inherent feedback may not be of a negligible order over the entire frequency range of interest, perfect cancellation may not be realizable in an experimental setting.

There are typically two different sources of errors and effects that affect the experimental results: (1) errors from the amplitude mismatch and the phase mismatch between the

actual setup and the model and (2) errors from neglecting the inherent acoustic feedback. The impact of the different errors on the stability and performance of the controlled system is investigated in this section.

5.2.1. Analysis of Inherent Acoustic Feedback

In this section, a sufficient condition to justify Eq. (5.8a) is provided. It is shown from Eqs. (3.68) and (4.2) that the pressure field at the reference microphone can be expressed in terms of the primary noise source $W(s)$ and the flexible panel modal coordinates $\eta_i(t)$ as

$$Y(s) = G_{YW1} W(s) + \mathbf{G}_{Y\eta} \boldsymbol{\eta}(s). \quad (5.9)$$

In this equation, and throughout the rest of the analysis, the term \mathbf{G}_{η^*} is used to represent the transfer function matrix between the input (*) and the panel modal coordinates $\boldsymbol{\eta}$ while the term $\mathbf{G}_{*\eta}$ is used to represent the transfer function matrix between the panel modal coordinates $\boldsymbol{\eta}$ and the output (*). In Eq. (5.9), the first term represents p_{op1} while the second term represents the inherent acoustic feedback pressure field p_{op2} due to the inherent acoustic feedback. Thus, minimizing p_{op2} with respect to p_{op1} will ensure that the inherent acoustic feedback effect is minimal, and hence, the condition (5.8a) can be satisfied.

Theorem: Given that

$$\left\| \frac{\mathbf{G}_{Y\eta} \mathbf{G}_{\eta W}}{G_{YW}} \right\|_{\infty} < 1, \quad (5.10)$$

the effect of the inherent acoustic feedback is negligible, if the magnitude of the

control transfer function's upper bound satisfies the following inequality:

$$\|G_c\|_\infty \ll \frac{1 - \left\| \frac{\mathbf{G}_{Y\eta} \mathbf{G}_{\eta W}}{G_{YW}} \right\|_\infty}{2 \left\| \mathbf{G}_{Y\eta} \mathbf{G}_{\eta U} \right\|_\infty}. \quad (5.11)$$

Proof:

The ratio of the pressure components P_{op1} and P_{op2} is

$$\frac{P_{op2}}{P_{op1}} = \frac{\mathbf{G}_{Y\eta} \boldsymbol{\eta}}{G_{YW} W}, \quad (5.12)$$

where the panel modal acceleration vector is given by

$$\boldsymbol{\eta} = \mathbf{G}_{\eta W} W + \mathbf{G}_{\eta U} U. \quad (5.13)$$

After substituting Eq. (5.13) into Eq. (5.12), the result is

$$\begin{aligned} \frac{P_{op2}}{P_{op1}} &= \frac{\mathbf{G}_{Y\eta}}{G_{YW}} \left\{ \mathbf{G}_{\eta W} + \mathbf{G}_{\eta U} \frac{U}{W} \right\} \\ &= \frac{\mathbf{G}_{Y\eta}}{G_{YW}} \left\{ \mathbf{G}_{\eta W} + \mathbf{G}_{\eta U} \frac{U}{P_{op1}} G_{YW} \right\} \\ &= \frac{\mathbf{G}_{Y\eta}}{G_{YW}} \left\{ \mathbf{G}_{\eta W} + \mathbf{G}_{\eta U} \frac{U}{Y} \frac{Y}{P_{op1}} G_{YW} \right\} \end{aligned} \quad (5.14)$$

Introducing $Y(s) = P_{op1}(s) + P_{op2}(s)$ into Eq. (5.14), the pressure ratio becomes

$$\frac{P_{op2}}{P_{op1}} = \frac{\mathbf{G}_{Y\eta}}{G_{YW}} \left\{ \mathbf{G}_{\eta W} + \mathbf{G}_{\eta U} \frac{U}{Y} \left(1 + \frac{P_{op2}}{P_{op1}} \right) G_{YW} \right\} \quad (5.15)$$

Since $G_c(\omega) = U(\omega) / Y(\omega)$, rearranging the above equation leads to

$$\frac{P_{op2}}{P_{op1}} = \frac{\mathbf{G}_{y\eta}}{G_{YW}} \frac{[\mathbf{G}_{\eta W} + \mathbf{G}_{\eta U} G_c G_{YW}]}{\left(1 - \frac{\mathbf{G}_{y\eta}}{G_{YW}} \mathbf{G}_{\eta U} G_c G_{YW}\right)} \quad (5.16)$$

To ensure that the IAF can be neglected, the magnitude of this ratio should be much less than unity over the frequency span. This implies that

$$\left| \frac{\mathbf{G}_{y\eta}}{G_{YW}} \frac{[\mathbf{G}_{\eta W} + \mathbf{G}_{\eta U} G_c G_{YW}]}{\left(1 - \frac{\mathbf{G}_{y\eta}}{G_{YW}} \mathbf{G}_{\eta U} G_c G_{YW}\right)} \right| \ll 1 \quad \forall \omega \quad (5.17)$$

From triangle inequalities, the following two inequalities follow:

$$\left| \frac{\mathbf{G}_{y\eta}}{G_{YW}} \mathbf{G}_{\eta W} + \mathbf{G}_{y\eta} \mathbf{G}_{\eta U} G_c \right| \leq \left| \frac{\mathbf{G}_{y\eta}}{G_{YW}} \mathbf{G}_{\eta W} \right| + \left| \mathbf{G}_{y\eta} \mathbf{G}_{\eta U} \right| |G_c| \quad \forall \omega, \quad (5.18a)$$

and

$$1 - \left| \mathbf{G}_{y\eta} \mathbf{G}_{\eta U} \right| |G_c| \leq \left| 1 - \mathbf{G}_{y\eta} \mathbf{G}_{\eta U} G_c \right| \quad \forall \omega. \quad (5.18b)$$

Thus, the condition in Eq. (5.17) is satisfied if the following inequality is met.

$$\frac{\left| \frac{\mathbf{G}_{y\eta}}{G_{YW}} \mathbf{G}_{\eta W} \right| + \left| \mathbf{G}_{y\eta} \mathbf{G}_{\eta U} \right| |G_c|}{1 - \left| \mathbf{G}_{y\eta} \mathbf{G}_{\eta U} \right| |G_c|} \ll 1 \quad \forall \omega \quad (5.19)$$

From Eq. (5.19), it follows that

$$\left| \frac{\mathbf{G}_{Y\eta}}{G_{YW}} \mathbf{G}_{\eta W} \right| + \left| \mathbf{G}_{Y\eta} \mathbf{G}_{\eta U} \right| \|G_c\| \ll 1 - \left| \mathbf{G}_{Y\eta} \mathbf{G}_{\eta U} \right| \|G_c\| \quad \forall \omega \quad (5.20)$$

After rearranging Eq. (5.20), an upper bound for the control action can be determined as

$$\|G_c\| \ll \frac{1 - \left| \frac{\mathbf{G}_{Y\eta}}{G_{YW}} \mathbf{G}_{\eta W} \right|}{2 \left| \mathbf{G}_{Y\eta} \mathbf{G}_{\eta U} \right|} \quad \forall \omega \quad (5.21)$$

After introducing the ∞ -norm; that is, $\|G(j\omega)\|_\infty := \sup_\omega |G(j\omega)|$, it is noted that the

following two inequalities apply:

$$\|G_c\| \leq \|G_c\|_\infty \quad \forall \omega, \quad (5.22)$$

and

$$\frac{1 - \left\| \frac{\mathbf{G}_{Y\eta}}{G_{YW}} \mathbf{G}_{\eta W} \right\|_\infty}{\left\| \mathbf{G}_{Y\eta} \mathbf{G}_{\eta U} \right\|_\infty} \leq \frac{1 - \left| \frac{\mathbf{G}_{Y\eta}}{G_{YW}} \mathbf{G}_{\eta W} \right|}{2 \left| \mathbf{G}_{Y\eta} \mathbf{G}_{\eta U} \right|} \quad \forall \omega$$

From which Eq. (5.11) follows. ■■■

Starting from Eq. (5.21), it can be ensured that the right-hand side (RHS) of Eq. (5.20) is always positive. It is mentioned that the condition (5.11) is a sufficient condition and that the upper bound defined in Eq. (5.11) is more conservative than that given by Eq. (5.21).

5.2.2. Analysis of Stability and Performance

In Figure 5.5(a), the block diagram representation of Figure 5.4 is modified with the insertion of two new complex functions, namely $\delta(s)$, representing the error in the primary direct path associated with implementing assumptions (5.8b) and (5.8c), and $\xi(s)$, representing the errors associated with implementing the control transfer function (5.5), including the assumption (5.8a) of neglecting the inherent acoustic feedback. In the nominal case, both $\delta(s)$ and $\xi(s)$ are each equal to unity. It is noted that the amplitude and phase mismatch errors can be directly related to $\delta(s)$ and partly related to $\xi(s)$, while

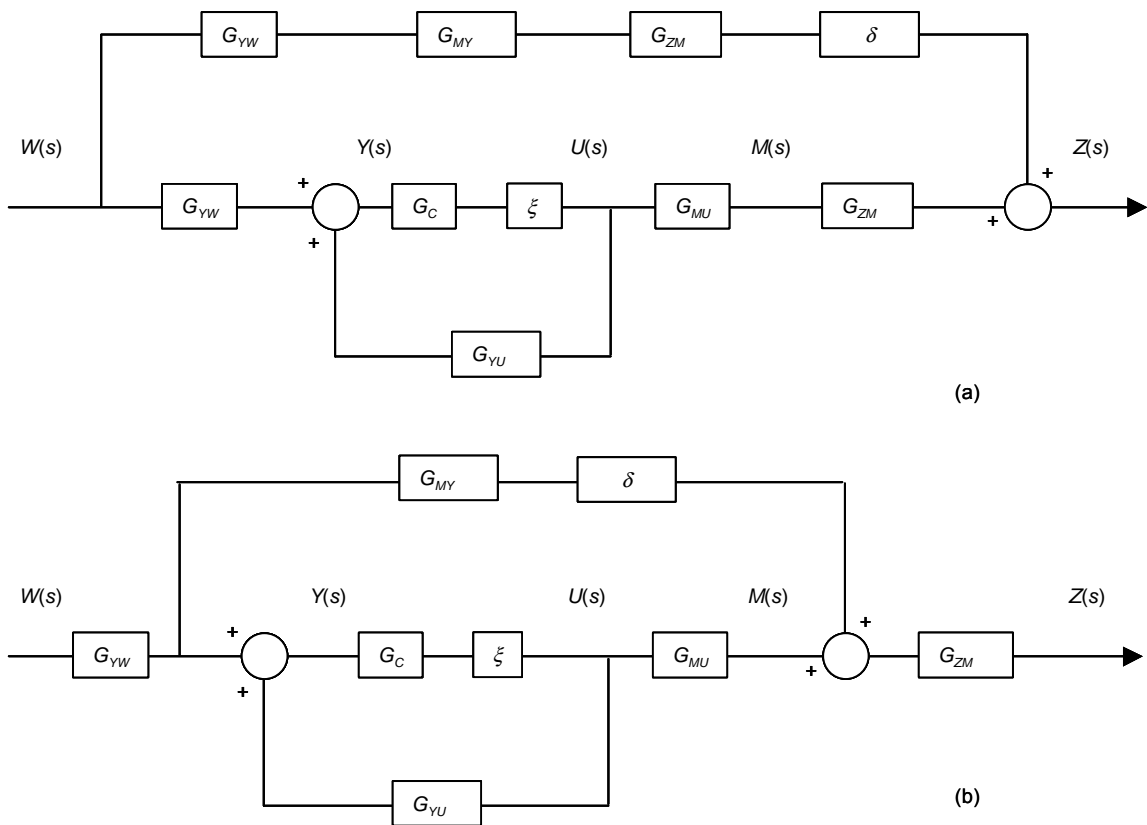


Figure 5.5. (a) Reconstructed zero spillover controller for ASAC system for stability and performance analysis and (b) simplified version.

the errors associated with neglecting the inherent acoustic feedback is directly related to $\xi(s)$. In Figure 5.5(b), a possible simplification for the block diagram is shown.

Now, the primary noise path, or the *uncontrolled* sound response at the error microphone, is given by

$$Z = G_{ZM} G_{MY} \delta G_{YW} W, \quad (5.23)$$

where the argument “s” of the functions is not shown explicitly for simplicity. After substituting for G_{PQZ1} from Eq. (5.5), the *controlled* sound response at the error microphone becomes

$$\bar{Z} = G_{ZM} G_{MY} \delta \left[\frac{(1 - \frac{\xi}{\delta}) + \xi G_{MY} \frac{G_{YU}}{G_{MU}}}{1 + \xi G_{MY} \frac{G_{YU}}{G_{MU}}} \right] G_{YW} W. \quad (5.24)$$

From Eqs. (5.23) and (5.24), the following attenuation ratio is determined:

$$\frac{\bar{G}_{ZW}}{G_{ZW}} = \frac{\left[(1 - \frac{\xi}{\delta}) + \xi G_{MY} \frac{G_{YU}}{G_{MU}} \right]}{\left[1 + \xi G_{MY} \frac{G_{YU}}{G_{MU}} \right]} = 1 - \frac{\frac{\xi}{\delta}}{1 + \xi G_{MY} \frac{G_{YU}}{G_{MU}}}. \quad (5.25)$$

From this expression, it is clear that the terms $[1 + \xi G_{MY} G_{YU} / G_{MU}]$ and $[\xi / \delta]$ are very significant. As the inherent acoustic feedback approaches zero (e.g., if a non-acoustic reference sensor was used), the stability of the system would depend only on δ being minimum phase, and the attenuation achieved by the controller would be

$$\frac{\overline{G}_{ZW}}{G_{ZW}} = 1 - \frac{\xi}{\delta}, \quad (5.26)$$

and therefore, the ratio $[\xi / \delta]$ is labeled here as the *attenuation index*. The term $[1 + \xi G_{MY} G_{YU} / G_{MU}]$, which does not depend on δ , is also important for the stability of the control system and it is labeled here as the *critical characteristic polynomial*. Furthermore, if the sensitivity of the collocated microphone is equal to or larger than the sensitivity of the reference microphone, the term G_{YU} / G_{MU} is expected to be always less than unity, since the collocated microphone is much closer to the actuator than the reference microphone. The second term in Eq. (5.25) represents a *single input, single output* (SISO) feedback system; hence, stability bounds on ξ can be obtained from any classical SISO algorithm that tests the associated open loop transfer function $[\xi G_{MY} G_{YU} / G_{MU}]$ (for example, the root-locus method). Since the uncontrolled system transfer functions are stable, ξ and δ must also be stable. However, δ should not have any nonminimum phase zeros that can cause a system instability.

Here, for further analysis, both δ and ξ will be assumed to be real values around +1.0. This is consistent with the results of the experiments, since both analytical and experimental models capture the phase information well, as seen in the results presented in Chapter 3. Although the analysis is valid for complex values of δ and ξ , to simplify results only real values of δ and ξ are considered here. Equation (5.25) is represented graphically in Figure 5.6 at a single frequency ω , where x is the second term of Eq. (5.25) and α is the attenuation achieved by the controller. For $|\overline{G}_{ZW}|$ to be less than $|G_{ZW}|$, which is the condition for zero spillover, the vector x must lie inside a unit circle

centered at (+1). Thus, the stability and performance analysis for the system can be summarized in the following two steps:

- i. The open loop transfer function

$$\left[\xi G_{MY} \frac{G_{YU}}{G_{MU}} \right]$$

is plotted in the Nyquist plane and both gain margin and phase margin are noted for the maximum bounding value of ξ . This step tests the stability of the system to identification errors, and hence, it is noted as the “*stability test*”. Root-locus analysis is among many other classical techniques that can also be used for the same purpose.

- ii. The closed loop transfer function

$$\frac{\xi}{\delta} \left/ \left[1 + \xi G_{MY} \frac{G_{YU}}{G_{MU}} \right] \right.$$

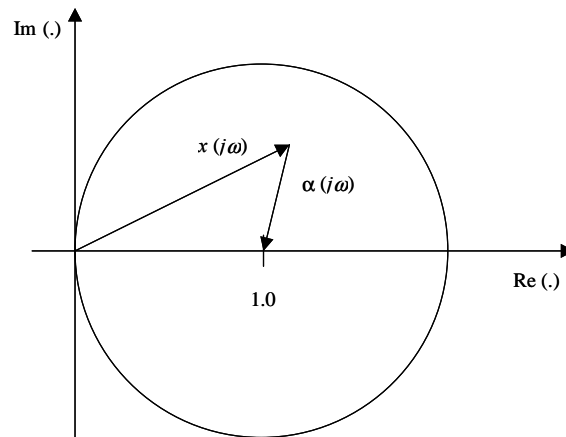


Figure 5.6. Performance test: Graphical representation of Eq. (5.25).

is plotted in the complex plane and it is checked to see if it lies within the unit circle for different values of δ and ξ to ensure zero spillover. The farther the plot is from the unit circle circumference, the larger is the noise attenuation. Therefore, this step is noted as the “*performance test*”.

5.3. Experimental Implementation of Control Scheme

The main purpose of this section is to examine whether the nonminimum phase condition for the transfer function G_{MU} and the inherent acoustic feedback condition can be experimentally realized. For this sake, the near-located microphones were added and

Table 5.1. Characteristics of near-located microphones.

Model Number	Size	Sensitivity	Frequency Range	Dynamic Range
Panasonic WM-54B	4.5 mm	-44±3 dB (6.31 mV/Pa)	40 Hz – 10 kHz	n/a [♦]

[♦]n/a: Not available.

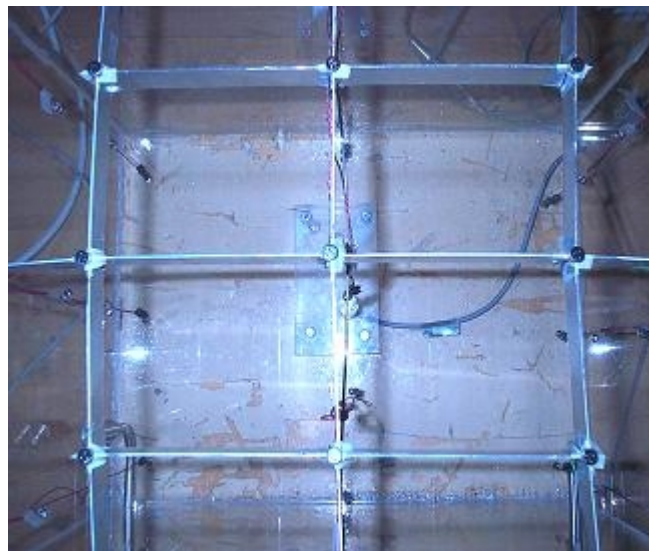


Figure 5.7. Photograph showing near-located microphones.

their positions were adjusted, the position and orientation of the reference microphone was adjusted, and many experimental runs were conducted while the transfer function identification was carried out by using the acquired data; this is explained later.

To realize the mapping of the actuation signal $U(s)$ to an acoustic signal $M(s)$, a mesh of near-located microphones was installed underneath the flexible panel in a manner so that each microphone is exactly underneath the center of a corresponding PZT actuator pair (please refer to Figure 2.3 for the locations of the microphones). They are labeled in columns {M-A, M-B, M-C}, and rows {1, 2, 3} (the prefix M representing a microphone). Characteristics of the near-located microphones are tabulated in Table

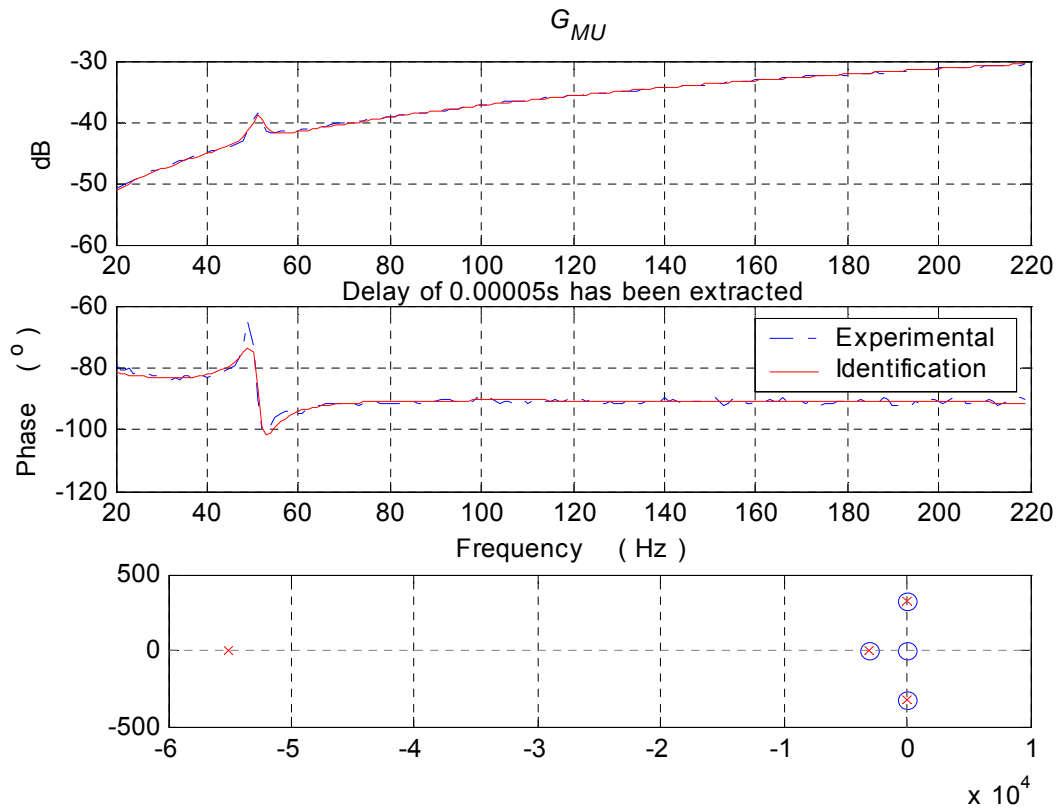


Figure 5.8. Experimental identification of the transfer function G_{MU} .

5.1 and a photograph of the mesh setup inside the enclosure is shown in Figure 5.7. The separation distances between the PZT patches and the near-collocated microphones were varied and the different transfer functions were experimentally identified and checked for any nonminimum-phase zeros in G_{MU} . It was noted that a separation distance equal to or less than 10.0 mm gives reasonable results, and, therefore, this distance was fixed at 10.0 mm.

In Figure 5.8, the frequency response of the identified transfer function G_{MU} is compared with the experimentally identified system frequency response. The experimental transfer function identification technique is used in this step to ensure that the response captures all of the system characteristics that cannot be captured by the analytical model. Also, it is shown from the pole-zero map of the identified transfer function G_{MU} that this function is minimum phase. (In order to generate this figure, a phase delay of 5×10^{-5} seconds was

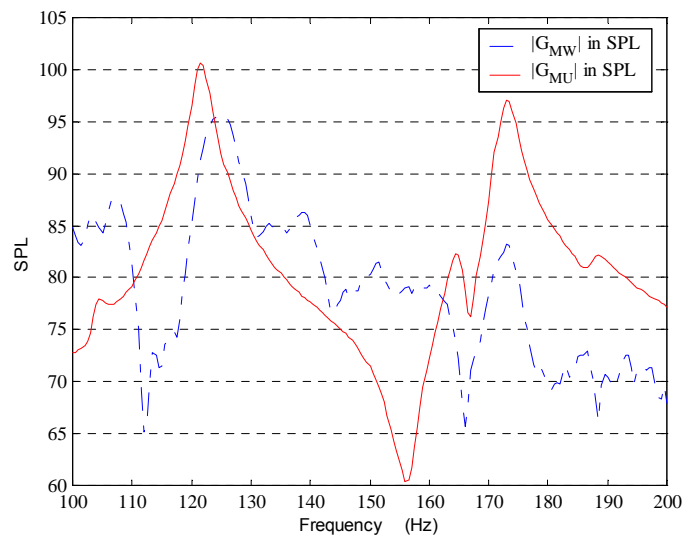


Figure 5.9. Sound pressure level measured at the collocated microphone when individually excited by noise source and piezo patch.

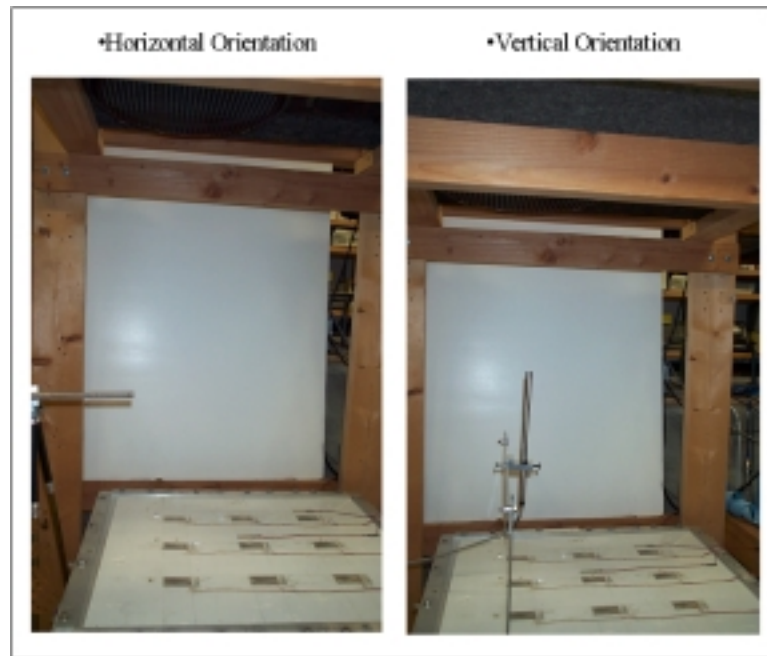


Figure 5.10. Photograph showing the reference microphone in horizontal and vertical arrangements.

extracted from the measurements. It is believed that this phase delay is due to the acoustic chamber of the collocated microphone as well as the electrical circuitry.)

Next, the influences of the location, orientation, and directivity effects of the reference microphone on G_{YW} and G_{YU} is examined. This test is also needed to ascertain if G_{YU} can be neglected in the control design, as indicated in assumption (5.8a). Since the control excitation is required to generate an acoustic potential energy at the collocated microphones that is comparable to that of the noise source, the input values for the piezoceramic patch pair B2 and the loudspeaker were adjusted so that the average SPL at the collocated microphone M-B2 when individually excited by each one is about the same. In Figure 5.9, the magnitudes of G_{MW} and G_{MU} are shown over the frequency span of $100 \leq f \leq 200$ Hz for white noise excitations. In this experiment, the piezoceramic

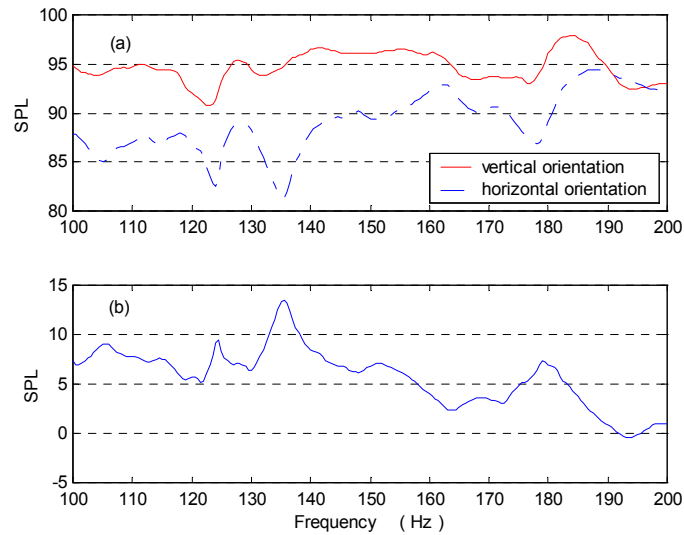


Figure 5.11. Amplitude of the pressure component $Y_1(\omega)$: (a) vertical versus horizontal orientations and (b) magnitude difference.

input gain was set to 50 and the gain for the speaker voltage input was set to 0.4. Both transfer functions are shown to have about the same SPL average for these selected values.

With these values, many experiments were conducted by providing voltage inputs to the noise source and piezoceramic patch pair B2, individually, and measuring the corresponding *sound pressure levels* (SPLs) at the reference microphone. In each run, the reference microphone was set at a point on a virtual circle in the xz plane centered at 35.56 cm (14") above the mid point of the flexible panel and with a radius of 15.24 cm (6"). The orientation of the microphone was also set at different angles ranging from 0° , for the horizontal orientation, to 90° , for the vertical orientation. In Figure 5.10, a photograph of the experimental arrangement with the reference microphone alignment in the horizontal and vertical orientations is shown. In Figure 5.11, the amplitudes of the

pressure component $Y_1(\omega)$ of the noise generated by the loudspeaker and picked up by the reference microphone are plotted over the frequency span $100 \leq f \leq 200$ Hz for two different orientations, namely, horizontal and upright vertical positions. It is clear from Figure 5.11(b) that the vertical orientation results in pressure amplitudes higher than that obtained with the horizontal orientation at almost all frequencies in the chosen span.

Similarly, in Figure 5.12, the amplitude of the pressure component $Y_2(\omega)$ of the noise generated by the control source (PZT pair patch B2) and sensed by the reference microphone in the same horizontal and upright vertical orientations are shown. It is clear from Figure 5.12(b) that the vertical orientation results in pressure amplitudes lower than that obtained with the horizontal orientation at almost all frequencies in the chosen span.

Next, the magnitude of $P_1(\omega)$ is compared with the magnitude of $P_2(\omega)$, when the

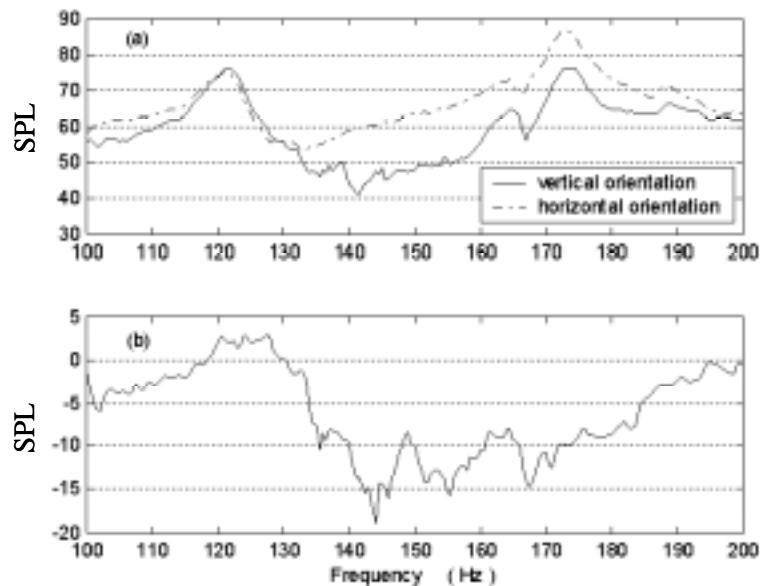


Figure 5.12. Amplitude of the pressure component $Y_2(\omega)$: (a) vertical versus horizontal orientations and (b) magnitude difference.

reference microphone is set in the upright vertical position. Both pressure magnitudes are plotted in Figure 5.13 over the same frequency span. There is an SPL difference of at least 15 dB between the magnitudes of G_{YU} and G_{YW} throughout the frequency range (in

fact, $\max_{100 \leq f \text{ (Hz)} \leq 200} \frac{G_{YU}}{G_{YW}} \cong 18\%$). This observation partly supports the argument that the

feedback effect due to the piezoceramic actuation can be neglected at the reference microphone by comparison to the effect of loudspeaker, which is directly related to the assumption in equation (5.8a).

When conducting the inherent acoustic feedback test described in Section 5.2.1 with the

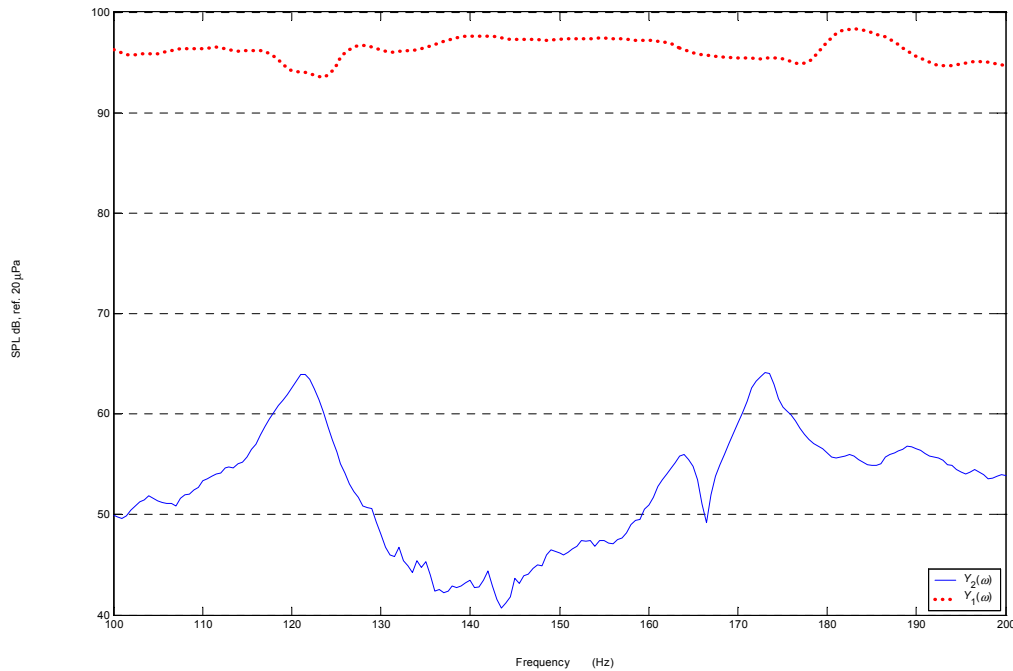


Figure 5.13. Amplitudes of the pressure components $Y_1(\omega)$ and $Y_2(\omega)$ measured at the reference microphone when individually excited by the noise source and piezo patch.

analytical model after accounting for the adjusted locations of the collocated and reference microphones over the frequency span of $0 \leq f \leq 400$ Hz, the right-hand side (RHS) of Eq. (5.11) is 92 dB while $\|G_C\|_\infty = 98$ dB. However, when Eq. (5.21) is evaluated at different frequencies, the control action magnitude is less than the value of RHS over the whole frequency span, except in a narrow band in the vicinity of 41 Hz, as shown in Figure 5.14. This ensures that the experimental adjustments satisfy the assumption (5.8a) of neglecting the inherent acoustic feedback.

To examine the assumption in equation (5.8b), the experimental data of G_{MW} versus (G_{YW} G_{MY}) are plotted and shown in Figure 5.15, where it is clear that this assumption is met with an error less than 3 dB over the entire frequency range.

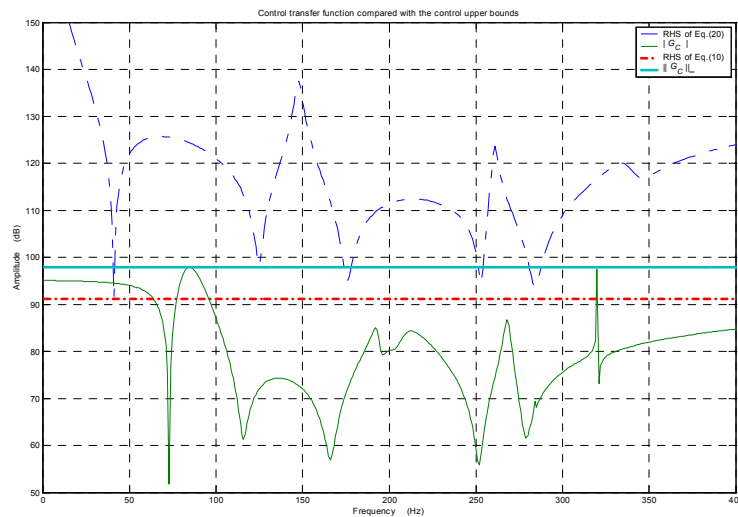


Figure 5.14. Magnitude of the PQZ controller frequency-response function along with the magnitudes determined from Eqs. (5.11) and (5.21). The bounds given by (5.11) and (5.21) are shown by broken lines.

Furthermore, in Figure 5.16, G_{ZW} versus $(G_{YW} G_{MY} G_{ZM})$ are plotted to examine the assumption made in equation (5.8c). It is shown here that there are considerable differences between the two cases, especially in the vicinity of the frequencies 118 Hz and 167 Hz. This difference goes as high as 30 dB at 167 Hz. This difference is expected because of the effects of the three-dimensional wave propagation and reflection inside the enclosure. The stability and performance tests are also checked for this case.

When applying the stability test to the experimentally identified system transfer functions, it turns out that the system is stable as long as $\eta \leq 1.1$. In Figure 5.17, the performance test is conducted for different values in the range $0.5 \leq \xi \leq 1.1$ and $0.5 \leq \delta \leq 2.0$. The performance test is run for the four extreme corners plus the pair (1.0,1.0), at which the attenuation index is unity, and (1.1,0.62), at which the attenuation index is 1.77. It is clear that as the attenuation index reaches unity, the attenuation in the

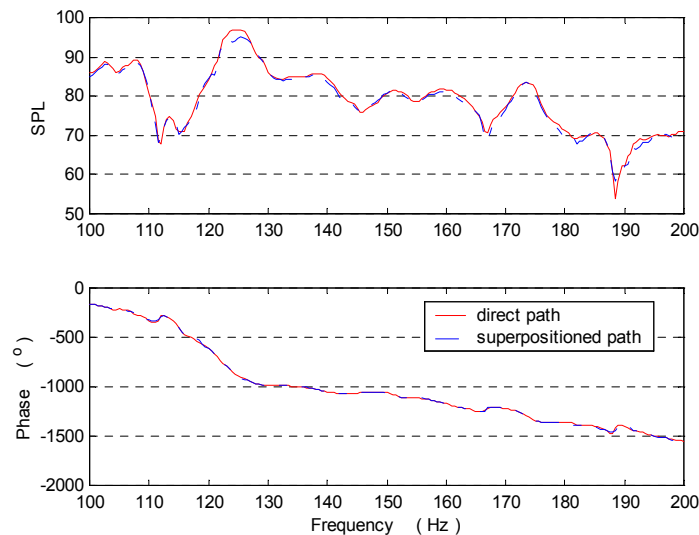


Figure 5.15. Acoustical path from the noise source to collocated microphone: G_{MW} versus $G_{MY} G_{YW}$.

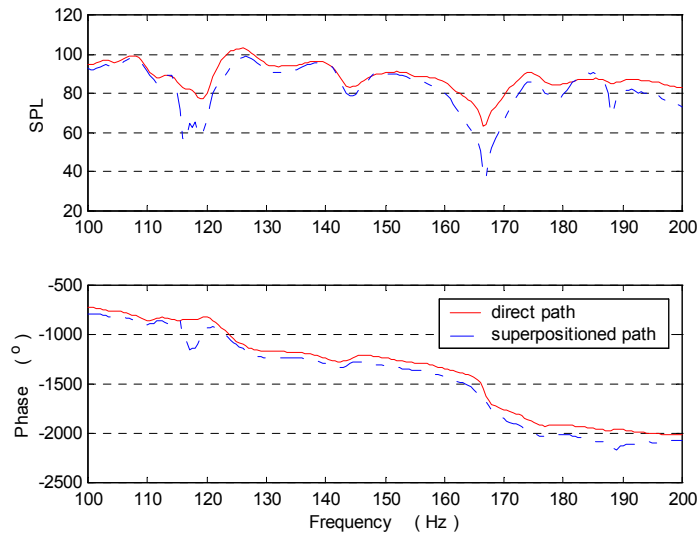


Figure 5.16. Acoustical path from noise source to error microphone: G_{ZW} versus G_{ZM} G_{MY} G_{YW} .

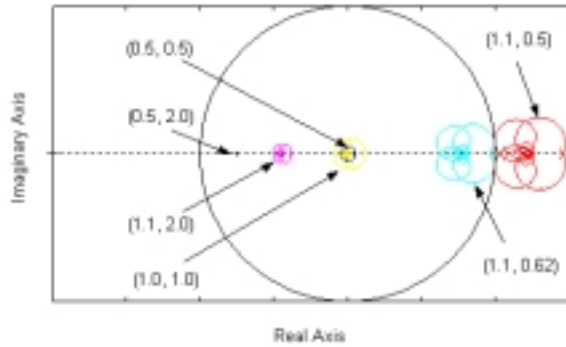


Figure 5.17. Performance test for different values of ξ (first argument) and δ (second argument).

noise signal increases significantly.

After applying the stability and performance tests to the experimental data and identified model, it has been found that $\xi = [0.8, 1.4]$ and $\delta = [0.6, 1.0]$. For this range of ξ , it has been found that further improvement in the model identification is necessary for the

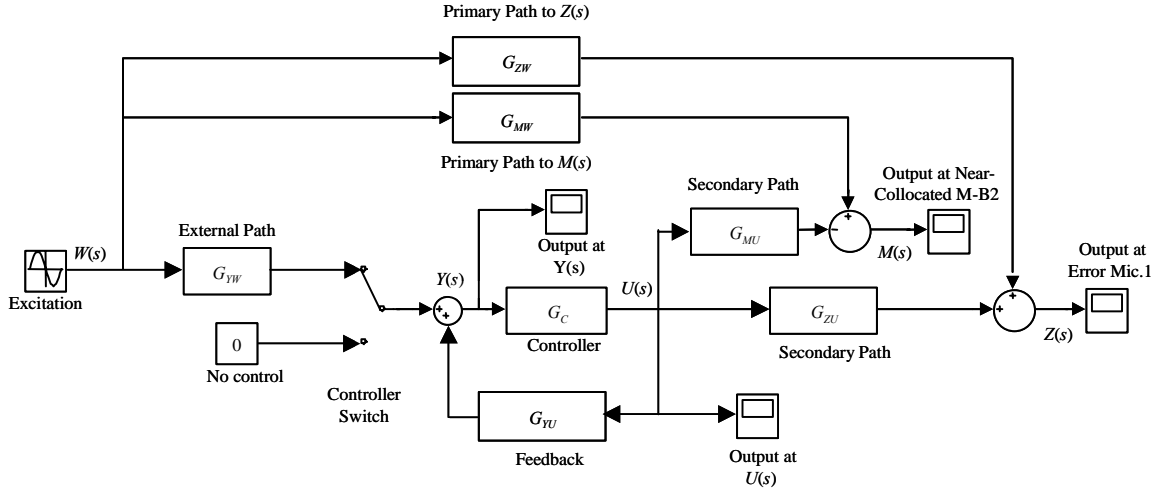


Figure 5.18. Simulation diagram used to simulate the loudspeaker-panel-enclosure model.

controlled system to be stable in the presence of acoustic reference sensing. This improvement in the model identification requires the model to have a great number of states, for which the real-time implementation of the control system cannot be realized.

However, if a non-acoustic sensor is used, then the system is still stable, and the controlled response varies from 14% to 133% of the uncontrolled one (i.e., it is also expected that spillover at some frequencies within the frequency band of interest will occur). These numbers are calculated by using the bounds given above for ξ and δ and Eq. (5.26). On a decibel scale, the controller is expected to produce from about 17 dB reduction to a 2.5 dB increase in the sound level. For example, at the frequency $f = 124$ Hz, which is close to plate's (3,1) modal frequency $f_{31} = 126$ Hz, $\xi = -1.0$ dB while $\delta = -3.0$ dB; thus the attenuation index is 1.26 and 11.7 dB attenuation is expected. Also, at $f = 174$ Hz, which is close to plate's (3,2) modal frequency $f_{32} = 172$ Hz, $\xi = 2.0$ dB while $\delta = -2.5$ dB; thus, the attenuation index is 1.68 and the expected attenuation is

about 3.4 dB.

5.4. Simulation and Experimental Results

In this section, the loud-speaker-panel-enclosure system is simulated by using both the experimentally identified model and the mechanics based model. For the purpose of this off-line simulation, MatLab/SimuLink software is used to construct the system model. The model is first simulated in the uncontrolled case, and then, in the controlled case by using the PQZ controller. The simulation diagram is shown in Figure 5.18. The controller switch shown in the diagram is used to switch between the uncontrolled and controlled cases.

5.4.1. Experimentally Identified Model Based PQZ Controller

When using the experimentally identified model for designing the PQZ controller, the direct transfer functions from the loudspeaker to the near-located microphone and to

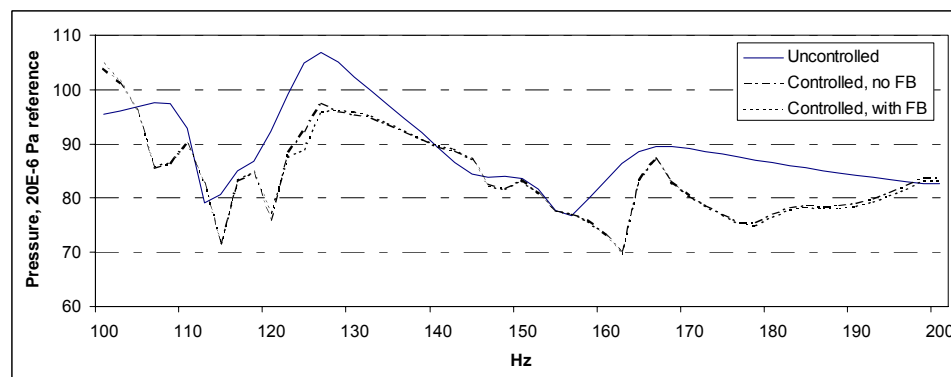


Figure 5.19. Simulation results: Pressure response at the error microphone Mic.1 obtained through simulations in the uncontrolled and controlled cases. In case (a), inherent feedback is neglected, and in case (b), this feedback is considered.

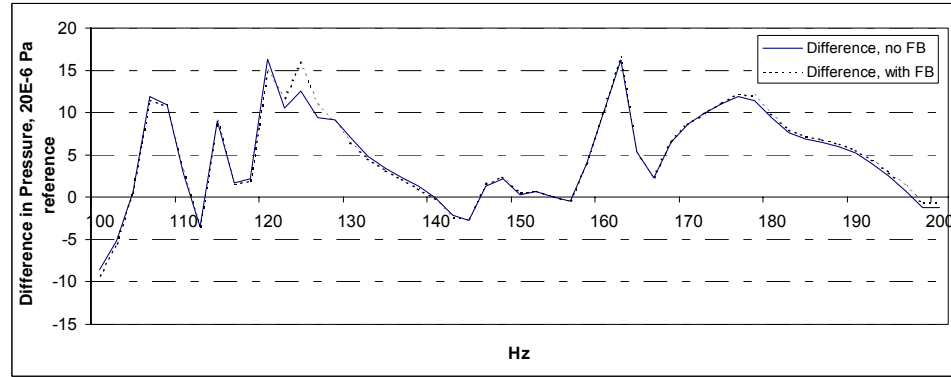


Figure 5.20. Simulation results: Differences between the pressure responses in the uncontrolled and controlled cases, at the error microphone location.

the error microphone (Mic.1) were used to simulate the real case and to account for the effects of the sound waves transmitted through the panel as well as the three-dimensional effects inside the enclosure. The simulated acoustic signals at the near-located microphone M-B2 and the error microphone Mic.1 were monitored along with the control signal. As was mentioned above, the frequency range used for the experimentally identified model is $100 \leq f \leq 200$ Hz.

In Figure 5.19, the noise (in SPL) of the uncontrolled system is compared with that of the controlled system at the error microphone Mic.1, and in Figure 5.20, the differences between the pressure values of the uncontrolled and controlled cases at Mic.1 are shown. It is seen that the simulated PQZ controller is effective for the considered model. In addition, the effect of the consideration of the inherent feedback is also illustrated in Figure 5.19, and as expected, this effect is negligible because of the proper choices of the sensor locations. It is also seen that the PQZ controller cannot eliminate the spillover completely. This is in agreement with the numerical results obtained through the stability

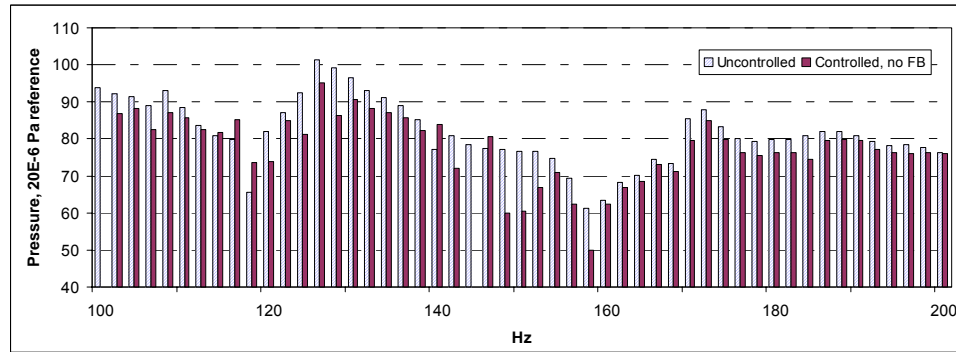


Figure 5.21. Experimental results: Pressure response, at the error microphone (Mic.1) location, measured experimentally in uncontrolled and controlled cases. Non-acoustic sensor was used as reference sensor.

and performance analysis described in Section 5.3. The high spillover values in the vicinity of 100 Hz and 200 Hz rise from the errors in the mathematical model, since it does not match the physical system outside the frequency range of interest.

However, when applying the controller to the experimental set up, instability was encountered at several tones making it difficult to record any results. As mentioned in the previous section, an instability is expected because of the high values encountered for ξ .

Experimental results have also been obtained for the case of a non-acoustic sensor. In this particular case, a voltage signal proportional to the noise signal was fed directly into the controller. The control voltage fed into each of the PZT patches was bounded to be less than ± 100 V in order to keep the PZT response as linear as possible (please refer to Section 3.3 for more details about the PZT response).

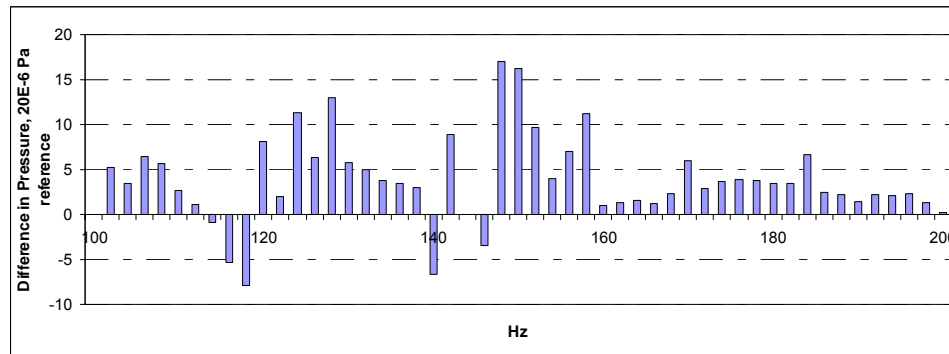


Figure 5.22. Experimental results: Differences between the pressure responses in the uncontrolled and controlled cases at the error microphone (Mic.1) location.

In Figure 5.21, the uncontrolled and controlled responses at the error microphone Mic.1 are shown, and in Figure 5.22, the corresponding differences are shown. To construct these figures, each experiment was run twice for the same tone, once with the controller off, and another with the controller on. By using a step size of 2.0 Hz and a total of 102 runs, these results have been generated. The experimental results are in agreement with the performance analysis presented in Section 5.3, where attenuation values up to 17 dB were achieved, and a spillover up to 7.9 dB occurred at some points. Furthermore, the experimental result agrees quantitatively with the simulation results shown in Figure 5.19 and Figure 5.20. It is noted that there is a shift in the high-frequency spikes to the right and the low-frequency spikes to the left. This is attributed to a band-pass filter, which was used to filter out the control signal in the experiments but not included in the system model. Also, the experiments of the controlled system were terminated at tones of 100 Hz and 144 Hz, as the control voltage values input to a PZT patch was higher than 100 V for each PZT patch, and this voltage threshold was used as the limiting value for the experiments. (The required control voltage values at these tones were 102.5 V and 102.4

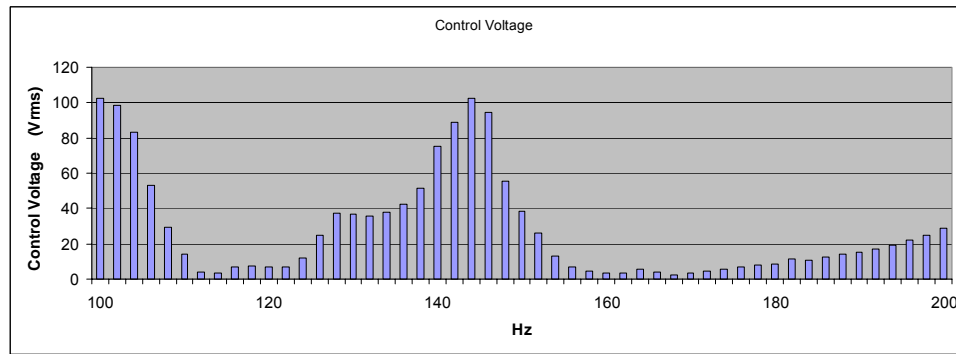


Figure 5.23. Control voltage inputs to the PZT pair B2 at different frequencies.

V, respectively.) The root mean square values of the control voltage into the chosen actuator at each frequency are plotted in Figure 5.23.

5.4.2. Analytical Model Based PQZ Controller

For obtaining the simulation and experimental results presented in this section, the system transfer functions derived from the analytical model developed in Section 3.1 are used in designing the PQZ controller. As in the previous section, the microphone Mic.1 was used as the error microphone, and, furthermore, the microphones Mic.2 and Mic.3 and the PZT pair patches A1 and B3 were used for performance measurements.

In the simulations, the system model was truncated to include the first seventeen vibration modes and three acoustic modes, whose modal frequencies were spread over the frequency range of $0 \leq f \leq 400$ Hz. Due to the location of the PZT actuator pair B2 and the error microphone Mic.1, the model does not allow for excitation or observation of vibration modes with even indices; for example, modes (2,1), (1,2), (2,2), and (3,2).

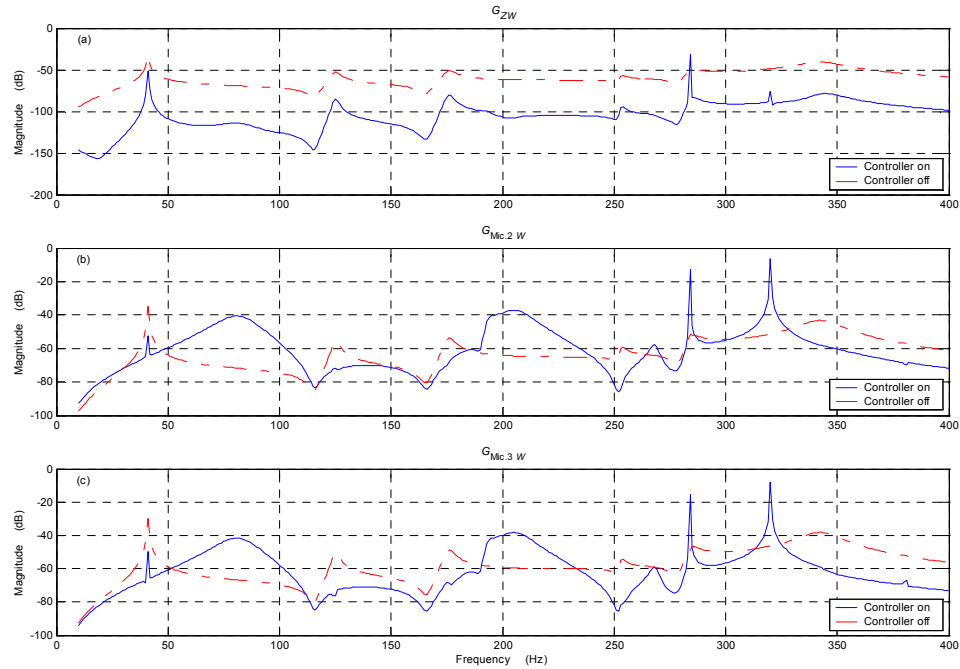


Figure 5.24. Simulation results for magnitudes of frequency-response functions in uncontrolled and controlled cases: (a) noise source, error microphone Mic.1, (b) noise source, performance microphone Mic.2, and (c) noise source, performance microphone Mic.3.

Hence, the net number of panel modes that play a role in the control transfer function is only five, namely the (1,1) mode with the modal frequency of 41.6 Hz, the (3,1) mode with the modal frequency of 124.9 Hz, the (1,3) mode with the modal frequency of 176.6 Hz, the (3,3) mode with the modal frequency of 252.6 Hz, and the (5,1) mode with the modal frequency of 284.7 Hz. Furthermore, the (0,1,0) acoustic mode with the modal frequency of 281.3 Hz is barely observed as well. This is because

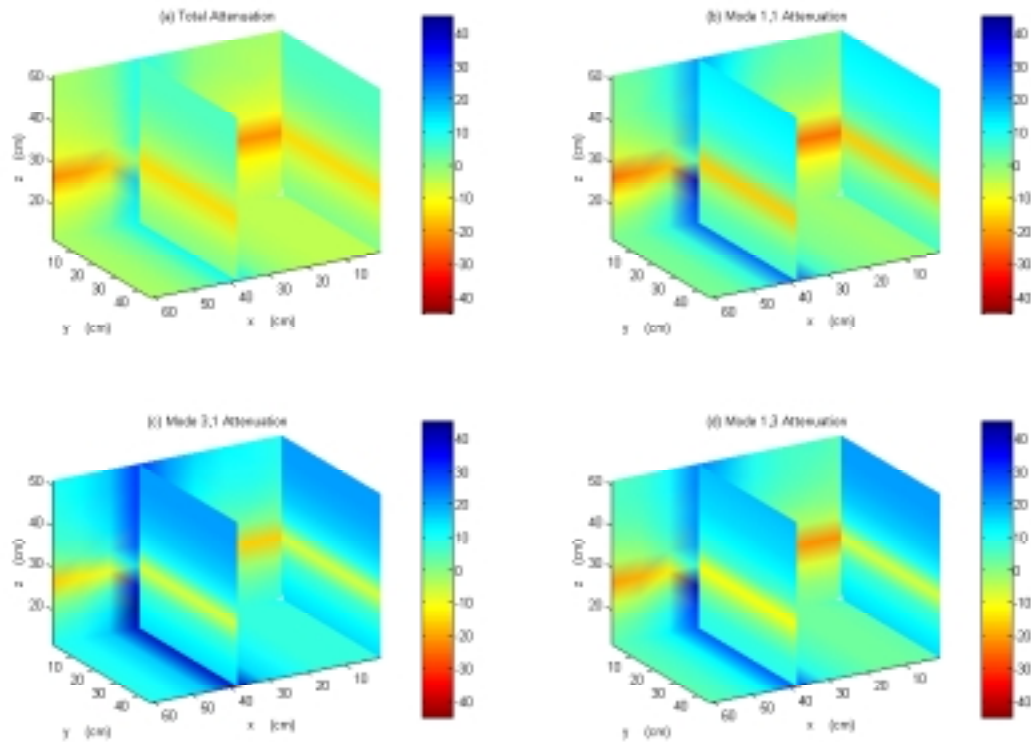


Figure 5.25. Simulation results for pressure attenuation inside the enclosure: (a) broadband excitation, (b) tonal excitation at modal frequency of (1,1) mode, (c) tonal excitation at modal frequency of (3,1) mode, and (d) tonal excitation at modal frequency of (1,3) mode.

the error microphone is located 1.25 cm in the x -direction away from the center of the enclosure. This small offset is not enough for a significant presence of the (1,0,0) acoustic mode. Thus, the acoustic mode (0,0,1) with the modal frequency of 337.6 Hz is the only mode that plays a role in the control transfer function. This reduces the number of modes used in designing the PQZ controller to only six (12 states), which is a significant reduction in the controller size compared to the experimentally identified

model-based controller that needed 34 states for a 75% shorter frequency span. Since the different phase delays are explicitly defined in the model, they do not add to the model total number of states, unlike the implicit inclusion via mathematical approximation techniques such as Padé approximation. However, modes that do not participate in the control transfer function are not controllable by the chosen actuator-sensor combination.

The simulation results are shown in Figure 5.24 and Figure 5.25. In Figure 5.24(a), the magnitude of the uncontrolled frequency response function G_{ZW} is compared with the magnitude of the controlled frequency response function \overline{G}_{ZW} . As shown in this figure, the zero-spillover condition is met and an overall attenuation of 17.5 dB is obtained over

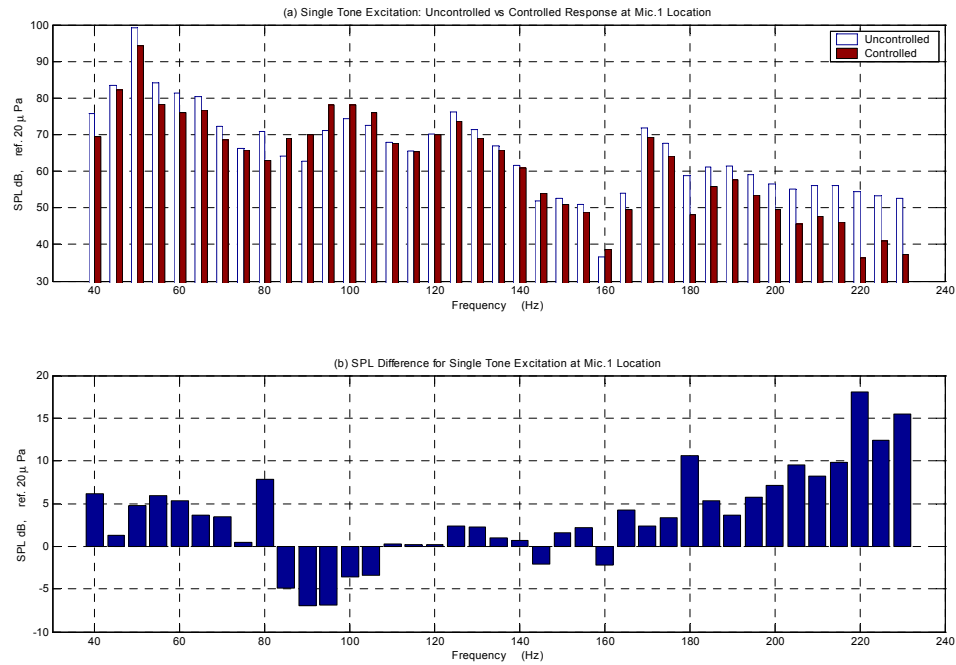


Figure 5.26. Tonal excitation: (a) SPL at error microphone (Mic.1) location measured in uncontrolled and controlled cases and (b) SPL difference.

the frequency range $0 \leq f \leq 400$ Hz. The spillover at 281.3 Hz is due to the uncontrolled acoustic mode (1,0,0). This means that any system dynamics that is not captured in the control transfer function, due to either unmodeled or unobserved modes may result in a spillover, as discussed later.

In Figure 5.24(b) and Figure 5.24(c), the frequency-response functions at the performance microphone locations Mic.2 and Mic.3 are shown, respectively. There is a significant attenuation in the vicinities of the resonance frequencies of the vibration modes (1,1), (3,1), (1,3), and (3,3). However, a high increase in the pressure levels is observed in the vicinities of the modal frequencies of modes with even indices; that is, mode (2,1) with the modal frequency of 73.7 Hz, mode (4,1) with the modal frequency of 196.1 Hz, and mode (2,3) with the modal frequency of 205.2 Hz, and at modal frequencies associated with the acoustic modes (1,0,0) and (0,1,0). The reason for the pressure increase is that these modes are neither observed by the error microphone nor targeted by the control action. This implies that the unobservable and/or uncontrolled system dynamics can result in an undesired pressure increase at locations other than the error microphone. In this particular case, there is an overall pressure increase of 7.2 dB and 2.7 dB in the pressure fields observed at the performance microphones Mic.2 and Mic.3, respectively.

In Figure 5.25, the pressure attenuation in the enclosure is plotted in the cases of broadband disturbance and tonal disturbances at frequencies close to the natural frequencies of the (1,1), (3,1), and (1,3) modes. This figure illustrates the spatial effectiveness of the control action. The plots show the attenuation values at two adjacent vertical planes 10.0 mm away from the vertical rigid walls, and a horizontal plane and a

vertical plane that intersect at the error-microphone location. It is seen that there is always a good attenuation in the vicinity of the location of the error microphone, as well as the near-located microphone. This reflects the area targeted by the PQZ controller. Second, as expected, in the case of a broadband disturbance, the control action results in a more localized attenuation compared to the cases of tonal (or narrowband) excitations. Third, there is always a significant pressure increase in the horizontal mid-plane area of the enclosure, which is not targeted by the control action.

Next, the experimental results obtained during the implementation of the PQZ controller are examined. Since the simulation results did not show good attenuations at frequencies

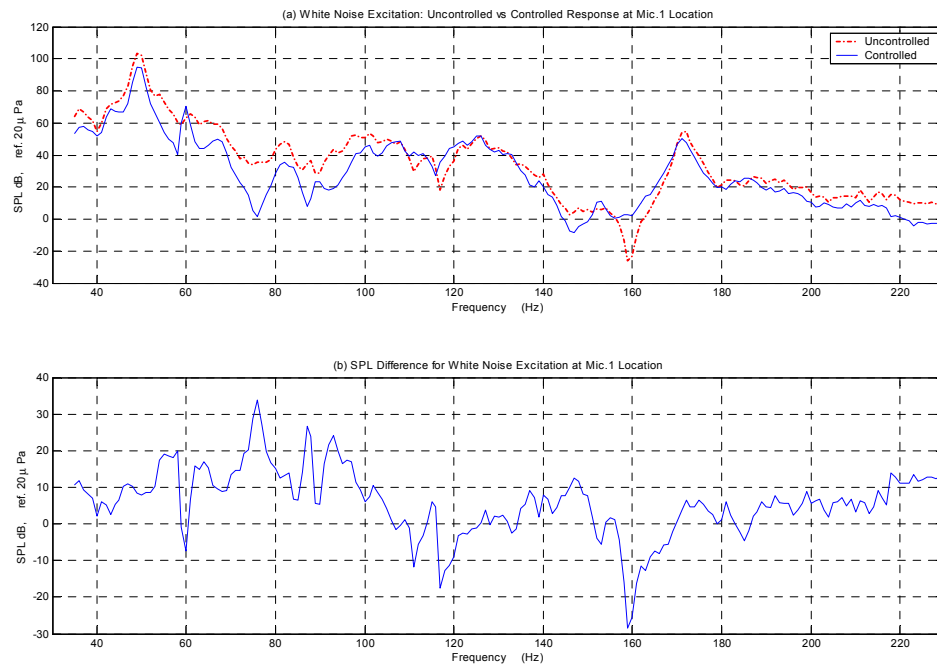


Figure 5.27. White noise excitation: (a) SPL at error microphone (Mic.1) location measured in uncontrolled and controlled cases and (b) SPL difference.

close to the modal frequencies of the acoustic modes, the control transfer function was constructed on the basis of only the first eight vibration modes and the first acoustic mode. This consideration of the modes is assumed to be reasonable for frequencies up to 230 Hz. In addition, for the PZT actuator pair B2 chosen, based on the location of this actuator, only the panel modes (1,1), (3,1), and (1,3) were used in the construction. However, since this actuator pair is not exactly centrally located on the panel, and since there are imperfections, excitations provided to this actuator pair have an effect on the other modes. Besides, and as was mentioned earlier, the resonance frequencies predicted by the model differ from the experimentally measured values. The good phase matching between the model predictions and the experimentally obtained values is expected to result in attenuation profiles similar to these obtained in the simulations.

In Figure 5.26, the *sound pressure level* (SPL) measurements obtained at Mic.1 in the controlled case are compared to the measurements obtained in the uncontrolled case. To carry out these measurements, the system was excited by the loudspeaker at different single tones, and for each single tone case, two experiments were carried out. In one case, the controller was on and, in the other case, the controller was off. By using a step size of 5.0 Hz and a total of 80 runs, the results shown in the frequency range 40.0 Hz to 230.0 Hz were generated. Experimental results at frequencies below 40 Hz could not be realized due to the limitations of the loudspeaker at low frequencies. An SPL attenuation up to 18.1 dB was achieved, and the spillover was about 7.0 dB at some frequencies. At the modal frequency of the (1,1), an SPL attenuation of 5.1 dB is observed, while the SPL attenuations observed at the natural frequencies of the (3,1) mode and (1,3) mode are 3.2 dB and 2.7 dB, respectively. There are several reasons for the increase in SPL in the

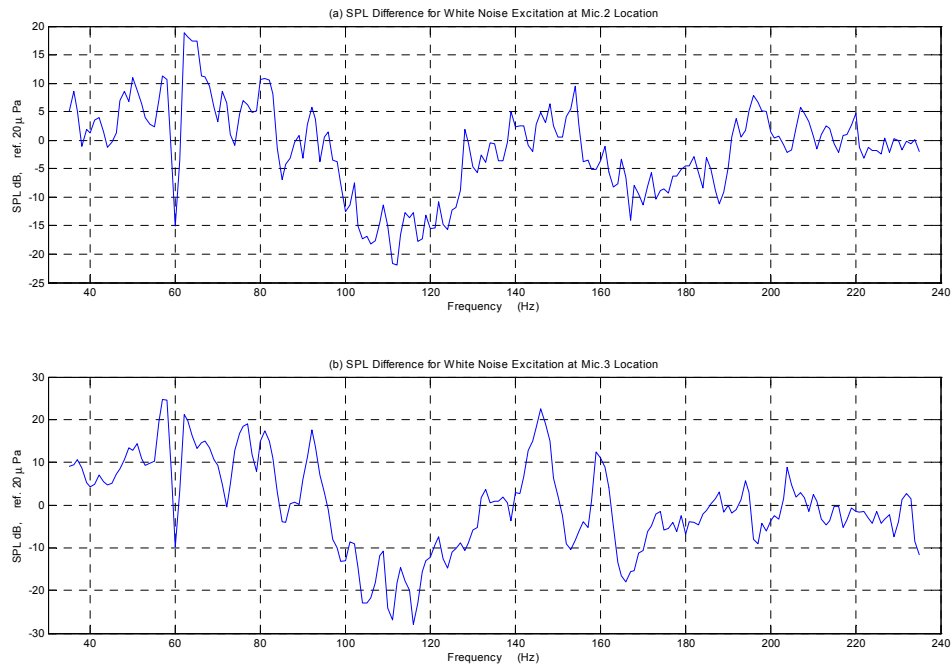


Figure 5.28. White noise excitation: SPL difference between the uncontrolled and controlled cases (a) at the performance microphone (Mic. 2) and (b) at the performance microphone (Mic.3).

vicinity of 95 Hz. The first reason is associated with the effect of the (1,2) vibration mode, which cannot be predicted by the model. The second reason is associated with the vibration mode (at 98 Hz) of the stand that holds the reference microphone. Compared to the simulation results, the insignificant SPL attenuation attained in the vicinity of 155 Hz is due to the effect of (2,1) mode. The spillover spots at 145 Hz and 160 Hz are believed to be due to the ambient noise at the reference microphone. At these frequencies, the noise generated by the loudspeaker has minimal effect at the error microphone location, but because of the ambient noise at the reference microphone, the controller continues to feed an incoherent control signal to the actuator, resulting in an increase in the SPL level.

In Figure 5.27, the results obtained for white noise excitation are shown. (Note that in Figure 5.27(a), a negative SPL value means a sound pressure level below the nominal value, and in Figure 5.27(b), a negative SPL means that the sound pressure level have increased in the controlled case.) An overall attenuation of 8.3 dB could be achieved, with attenuations of about 8.5 dB and 6.5 dB at modal frequencies of the (1,1) mode and (1,3) mode, respectively. The SPL increase at 60 Hz is due to line noise from the control hardware, which could not be eliminated. The spillover in the vicinity of 160 Hz may be explained, as before, in terms of ambient noise. The spillover observed around the frequencies of 112 Hz and 120 Hz is attributed to the difference between the predicted frequency and the exact resonance frequency of the (3,1) mode. This can be explained as a result of a slight shift in the location of a zero between the uncontrolled and controlled transfer functions; this results in the big increase in SPL. In Figure 5.28(a) and (b), the SPL differences at the microphones Mic.2 and Mic.3 are shown, respectively. Despite the SPL increase at 60 Hz, both graphs are qualitatively similar to the simulation results.

Since noise attenuation is carried out by using a feedforward scheme, a question that remains to be answered is where does the energy pumped into the system through the control action go? To answer this question, a measure of the panel vibration is obtained by measuring the strains at the locations of the PZT patches A1 and B3. In Figure 5.29, at these locations, the strain difference between the uncontrolled and controlled cases is shown. As shown here, the strain in the panel increases significantly in the controlled case. Both graphs of Figure 5.29 show a persistent strain increase along the frequency span. This increase is undesirable at the unobserved modes. Although the simulation results and measurements at performance microphones show SPL increases at some

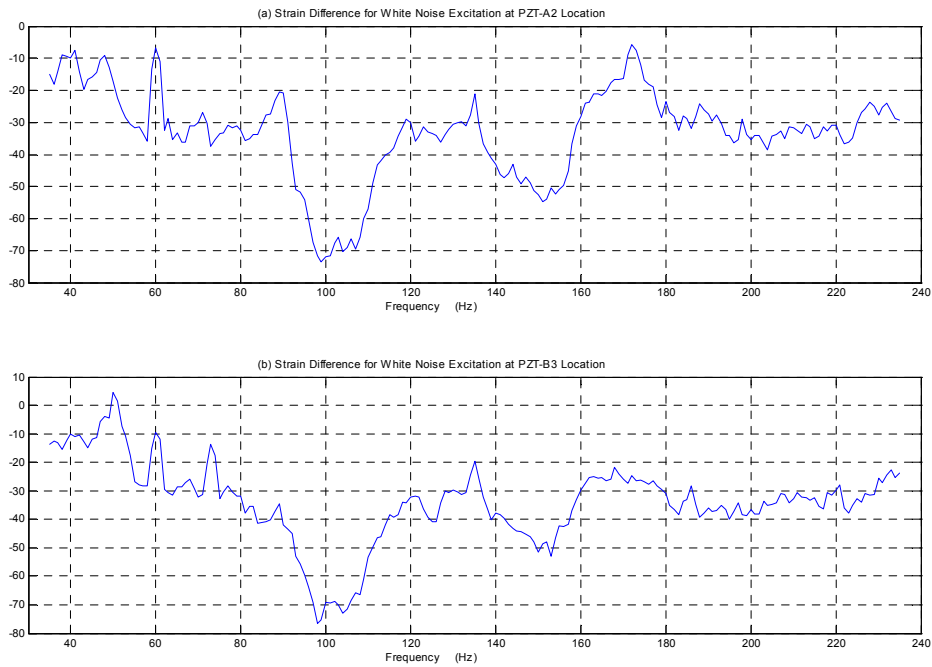


Figure 5.29. Difference between PZT patch strains in the uncontrolled and controlled cases for white noise excitation: (a) PZT patch A1 and (b) PZT patch B3.

frequencies and locations inside the enclosure, the results of Figure 5.29 provide an indication that that added energy, as well as the energy absorbed from the acoustic subsystem, is mainly transformed into high vibration levels of the flexible panel.

6. Control Design and Implementation: RZS Controller

In this chapter, analytical and experimental investigations into a *Relaxed Zero Spillover* (RZS) control scheme are presented. The qualifier “relaxed” is used here to mean that the controller is not restricted to perfectly cancel the noise but designed to maintain the controlled noise level bounded over a specific frequency region and to ensure that the energy spillover beyond this frequency region is also bounded. Spatially local attenuation of sound fields in the frequency range of 30 Hz to 90 Hz is studied here. This range includes the fundamental frequency of the system (51 Hz). The lower cutoff frequency is limited to 30 Hz because of the limitations on the loudspeaker at low frequencies. The frequency range extending up to 200 Hz is considered to show that the spillover outside the controlled region is within the prescribed bounds. The stability and sensitivity of the RZS scheme for a single input, single output case is discussed in the context of this chapter along with the other issues. In the next section, the controller development and construction is addressed, and subsequently, simulation results are presented and discussed.

6.1. RZS Control Design

With the aid of Eq. (5.23) and Eq. (5.24), the ratio of the controlled to the uncontrolled

signals can be derived in terms of the controller transfer function G_c as

$$\frac{\bar{G}_{ZW}}{G_{ZW}} = 1 + \frac{\eta \begin{bmatrix} G_{MU} \\ G_{MY} \end{bmatrix} G_C}{[1 - \eta G_{YU} G_C]} . \quad (6.1)$$

Let the control law be

$$G_C = -G_{RZS} . \quad (6.2)$$

Then, neglecting the effect of the acoustic feedback, Eq. (6.1) becomes

$$\frac{\bar{G}_{ZW}}{G_{ZW}} = 1 - \frac{\eta \begin{bmatrix} G_{MU} \\ G_{MY} \end{bmatrix} G_{RZS}}{G_{RZS}} . \quad (6.3)$$

This equation implies that, for the ratio of the controlled noise to the uncontrolled noise at the error microphone to be within an error ball of radius Δr_c in a specific frequency domain f_c and to be within an error ball of radius Δr_u beyond this region, the controller can be designed based on the following criterion:

$$TF := \frac{\eta \begin{bmatrix} G_{MU} \\ G_{MY} \end{bmatrix} G_{RZS}}{G_{RZS}} \in \begin{cases} D_c(r, \theta) \mid |r-1| \leq \Delta r_c, |\theta| \leq \sin^{-1} \frac{\Delta r_c}{\sqrt{2}} \end{cases}; & \forall f \in f_c \\ \in \{D_u(r) \mid |r| \leq \Delta r_u\}; & \forall f \notin f_c \end{cases} \quad (6.4)$$

The control domain D_c is represented schematically in Figure 6.1. It should be mentioned that D_c is still conservative, as it does not contain all of the possible points that satisfy the design requirements. This criterion can be satisfied if TF is chosen to match the transfer function of an elliptic or Chebyshev band pass filter, with a frequency bandwidth f_c , ripple Δr_c , and attenuation Δr_u [Helszajn, 1990]. This is equivalent to adding a filter to the controller in the sense of feedback control systems. Adding a filter to a feedforward

control scheme is not a straightforward procedure due to the phase effects of the filter on the system response. The Chebyshev filter has been used here because of its linear phase characteristics that can be modeled as a pure phase delay over the frequency bandwidth f_c , and hence, subtracted from the overall phase delay associated with the primary noise path. It is quite possible in designing a Chebyshev filter that the phase difference $|\theta|$ between the actual phase and the approximated phase delay is small over the filter bandwidth, except at the cutoff frequencies, and it should lie within the bounds given in Eq. (6.4) in order to achieve the control objective. The order of the filter is a design parameter that depends on the accepted ripple tolerance and the steepness of the filter frequency response at the cutoff frequencies.

6.2. Simulation and Experimental Results

In this section, off-line simulation results are provided. Here, an experimental approach is used to develop the system model. Experimental data are acquired and conditioned and then used as a basis to carry out the state space realization. Similar to the procedure used

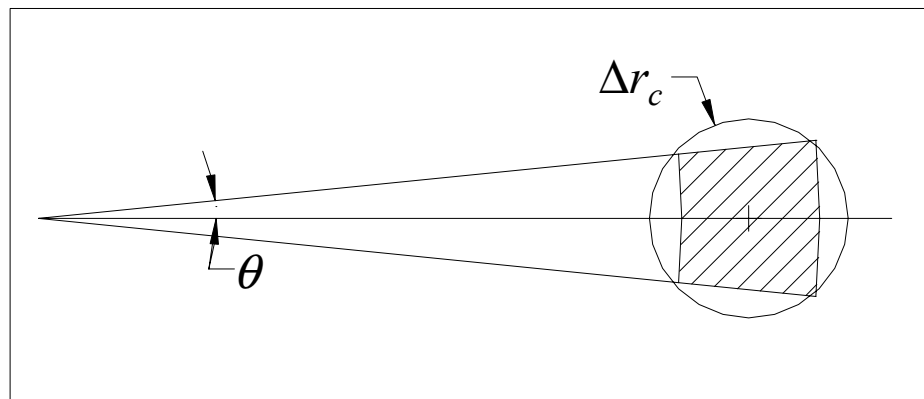


Figure 6.1. Representation of the control domain D_c .

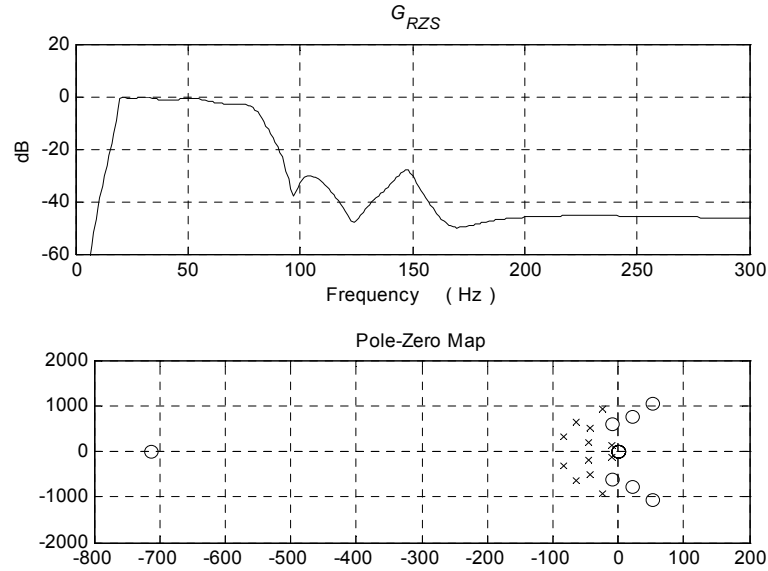


Figure 6.2. Frequency response and pole zero map of RZSC.

in the analytical model, the phase delays apparent in the acquired data were extracted during the conditioning procedure. Then, all of the phase delays of the different transfer functions were explicitly added and accounted for in the design of the controller. This eliminates the nonminimum phase zeros and the unnecessary number of poles that arise from the mathematical approximations of the phase delay. The objectives of the control design are the following: (1) attenuate the noise at the fundamental frequency by 70 % and (2) limit the spillover to a maximum of 5 % increase. For this reason, the frequency range $30 \text{ Hz} \leq f \leq 90 \text{ Hz}$ was chosen for constructing the RZS controller. By using these control design objectives along with Eq. (6.4), the controller is developed by considering the transfer function of a Chebyshev filter of order 5 with cutoff frequencies at 30 Hz and 90 Hz, a ripple of 1.0 dB, and an attenuation factor of 40 dB. This corresponds roughly to $\Delta r_c = 0.06$ and $\Delta r_u = 0.01$. These values are more conservative than those defined by the control design objectives, so as to account for the different approximations considered in

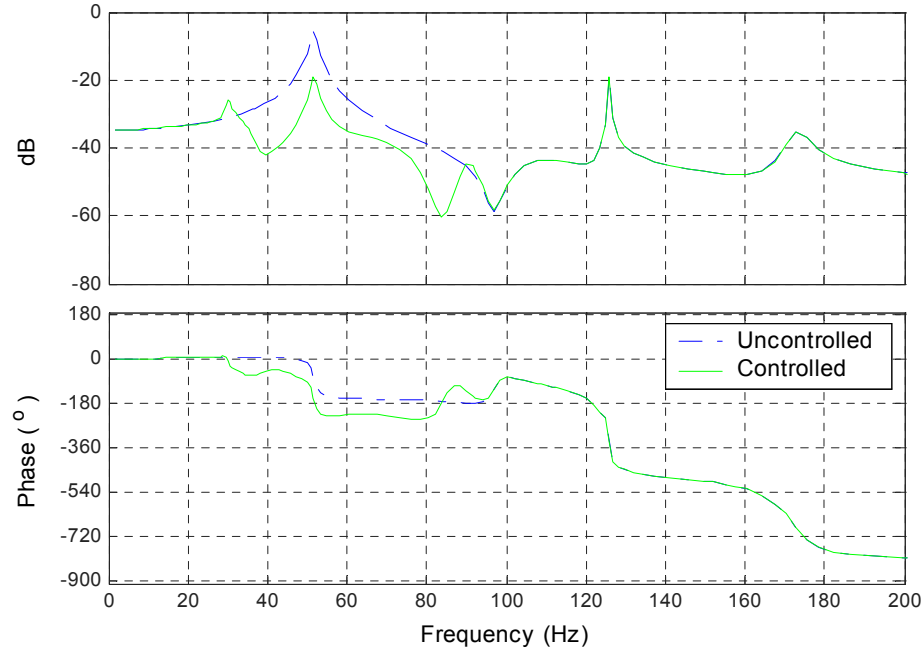


Figure 6.3. Comparison of frequency responses from the controlled and uncontrolled cases. Identified transfer functions are used.

the controller design, such as neglect of the IAF and errors associated with the experimental identification algorithm. The magnitude frequency response and pole zero map of the RZSC are shown in Figure 6.2.

In Figure 6.3, the frequency response of the uncontrolled system is compared with that of the controlled system at the location of microphone Mic.1 and by using the identified transfer functions. An attenuation of 14.0 dB is observed at the fundamental frequency while an attenuation of up to 20.0 dB is observed in the bandwidth of 35 Hz to 85 Hz. It is shown here that, in spite of neglecting the acoustic feedback in the controller design, the controller is able to produce considerable attenuation in the control bandwidth and ensure that the spillover is bounded over the frequency span. The spillover in the vicinity of the cutoff frequencies (30 Hz and 90Hz) is due to the mismatch between the phase

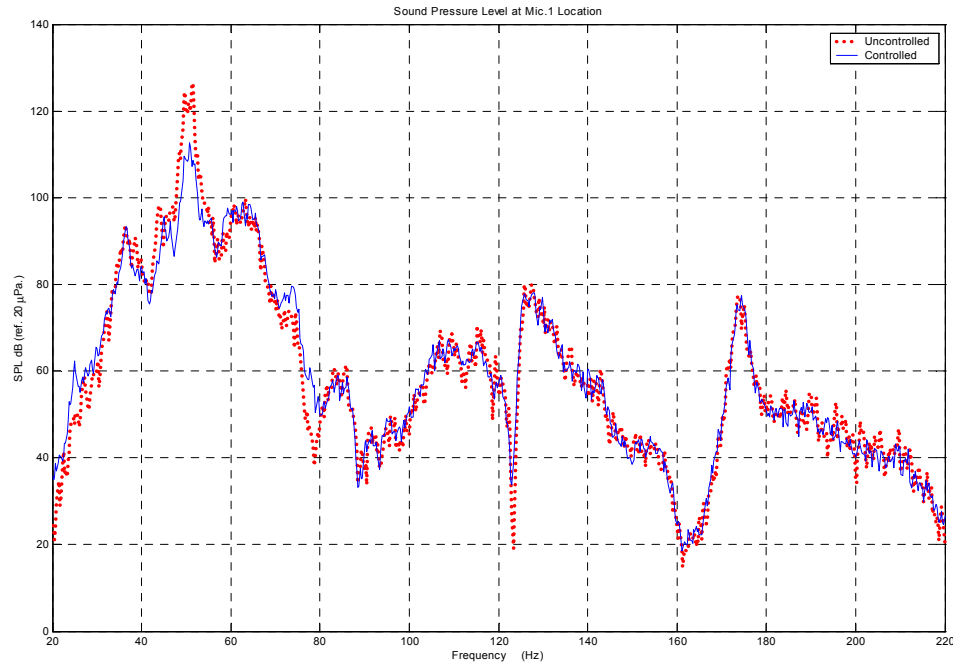


Figure 6.4. Sound pressure levels at the microphone Mic.1 location in uncontrolled (dotted line) and controlled (continuous line) cases.

response of the Chebyshev filter response and the approximated phase delay pattern in these regions.

Next, the RZS controller has been studied in the experimental setup of Chapter 2 and the SPL levels at the location of the microphone Mic.1 in the controlled and uncontrolled cases are shown in Figure 6.4. To generate this result, a band-limited white noise signal, with a bandwidth defined as $20 \text{ Hz} \leq f \leq 220 \text{ Hz}$, was fed into the loudspeaker and the microphone output signal was averaged 28 times. The experimental results are in qualitative agreement with the simulation results. The attenuation at the fundamental frequency is observed to be 14 dB and an overall attenuation of 5.56 dB is observed over the frequency range $20 \text{ Hz} \leq f \leq 220 \text{ Hz}$.

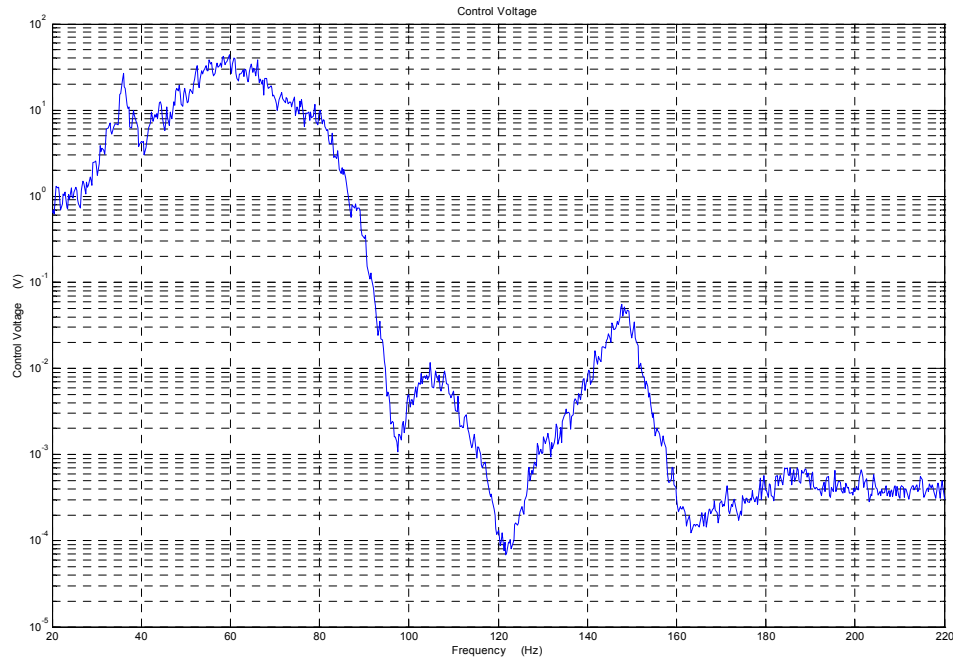


Figure 6.5. Control voltage signal fed to the PZT pair B2.

It is noticed here that the attenuation over the frequency range $20 \text{ Hz} \leq f \leq 100 \text{ Hz}$ is 5.70 dB; this is an indication that the spillover beyond the controlled frequency range is small. As mentioned above, the spillover in the vicinity of 25 Hz and 80 Hz are expected due to the filter cutoff frequencies. It is also noticed that the spillover beyond the controlled region is within the error limits defined by the controller design. The control voltage does not exceed 35.0V and feeds almost no energy into the system at frequencies beyond the frequency range of interest; this can be discerned from Figure 6.5, where the control signal gradually vanishes beyond the control bandwidth. These are important advantages over the PQZ controller, where the control voltage exceeds 100.0V and the unmodeled dynamics outside the frequency range of interest may result in an energy spillover.

6.3. Sensitivity Analysis

In this section, a numerical analysis has been conducted to investigate the sensitivity of the controlled response to changes in the magnitude and phase mismatches. The magnitude mismatch can arise from the magnitude errors in the identified transfer functions (lumped into ξ/δ), while the phase mismatch errors may arise from the incorrect identification of the pure delay values, bad choice of the controller parameters, bad phase equalization, or delay mismatch between the primary noise and the secondary noise paths. In Figure 6.6, it is shown as to how the attenuation at the fundamental

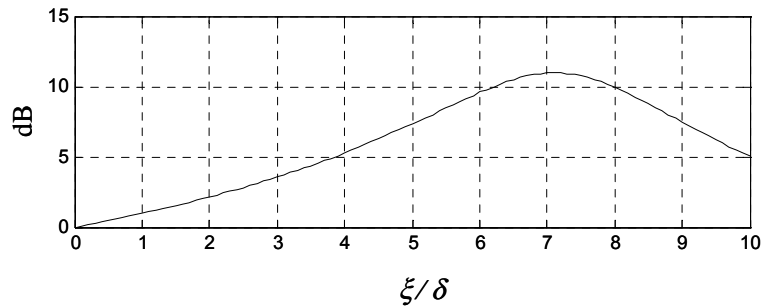


Figure 6.6. Changes in noise attenuation at the fundamental frequency with variations in ξ/δ .

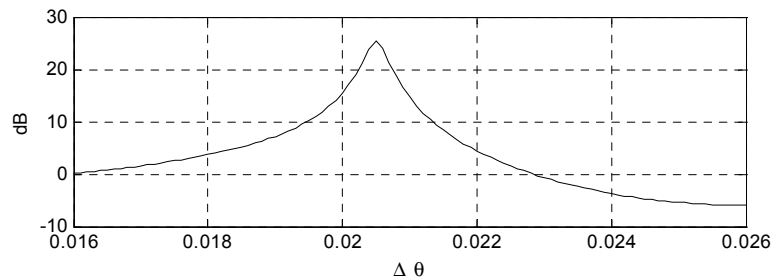


Figure 6.7. Changes in noise attenuation at the fundamental frequency with variations in phase delay.

frequency changes with the magnitude mismatch, and in Figure 6.7, it is shown as to how the attenuation at the fundamental frequency changes with the phase mismatch. To generate both figures, the experimental frequency-response data has been used and ξ / δ as well as the phase delay have been varied. It is illustrated here as to how the phase mismatch not only severely affects the attenuation, but may also increase the noise magnitudes as well.

7. Conclusions and Suggestions for Future Work

In this dissertation, model based zero-spillover schemes have been developed for an active structural-acoustic control (ASAC) application and these schemes have been studied for broadband reduction of the noise transmitted into a rectangular enclosure. It has been demonstrated that “appropriate” choices of the controller design parameters can result in significant attenuation in the control bandwidth without generating energy spillover beyond this frequency region. This effort is believed to be the first demonstration of a zero spillover structural-acoustic control scheme.

A comprehensive mechanics-based analytical model has been developed to predict the structural-acoustic interactions in the case of a rectangular three-dimensional enclosure with a flexible panel, which is placed in the near field of a noise source. Piezoelectric patches, which are bonded symmetrically to the top and bottom surfaces of the panel, are used as actuators, and microphone sensors located inside and outside the enclosure are used for acoustic pressure measurements. The developed model has the following advantages over the existing models:

i) It is capable of predicting external pressure fields due to both the noise source and structural-acoustic interactions and takes into account the general case of spherical wave propagation

and

ii) It takes into account explicitly defined system time delays; this technique reduces the model dimensionality without affecting its accuracy.

The numerical results from the analysis are found to be in good agreement with the corresponding experimental observations, especially in capturing the phase changes in the system. Even for the simple experimental setup used in this dissertation work, unlike the analytical model, techniques that use plane wave analysis were not successful in predicting the system dynamics. It has been noticed that the developed model has some limitations; these limitations are detailed in Section 3.3.

Two zero spillover control schemes, namely *Perfect Quiet Zone (PQZ)* and *Relaxed Zero Spillover (RZS)* control schemes, have been developed through this work. Both schemes can be applied to a variety of active structural-acoustic systems. Numerical and experimental results have shown that attenuations ranging up to 18.1 dB for narrowband disturbances and an attenuation of 8.3 dB for broadband excitation are realizable by the PQZ controller in the frequency range of $40 \text{ Hz} \leq f \leq 230 \text{ Hz}$. Simulations also predicted that the controlled zone is large, even when a single actuator pair is used; this point has been verified by measuring pressure fields at performance microphones far from the error microphone. It has been noticed that the PQZ controller cannot eliminate spillover at the frequencies corresponding to unmodeled dynamics. An increase of up to 7.0 dB in the

sound pressure level has been observed at some frequencies when applying tonal excitations. Simulations also show that the RZS controller can result in predefined attenuation levels over the entire frequency spectrum; the idea of predefined the attenuation levels in the controller design has not been introduced before. It has been shown that the RZS control scheme reduces the design efforts of the control transfer function to a design of a band-pass filter, which is simpler and straightforward. An overall attenuation of 5.56 dB has been realized in the frequency range of $20 \text{ Hz} \leq f \leq 220 \text{ Hz}$ with about 14 dB attenuation in the sound pressure level at the fundamental frequency. Spillover spots have been noticed at the cutoff frequencies of the filter transfer function. More investigations into the filter design can eliminate this problem. For general ASAC systems, analyses have also been developed for studying the stability and performance as well as the effect of inherent acoustic feedback. These analyses have been applied for the ASAC experimental setup used in this effort.

Since high attenuation values could be obtained by a single actuator pair when using either PQZ or RZS control schemes, it is suggested that these schemes be extended to multi-input, multi-output control schemes, starting with a 2-input 2-output scheme. Although this may not significantly increase the attenuation levels, if carefully designed, it may be able to spatially enlarge the controlled region. In addition, based on the promising results of the RZS control scheme, it is also suggested that it be implemented on other ASAC systems. It has been pointed out that the control bandwidth is limited by the total phase delay of the system. Thus, a suggestion for future work is to expand the controlled frequency span by collecting multiple actuators into groups, where each of them is designed to address a specific frequency span. The interconnections among the

various actuator groups will need to be studied. Furthermore, it is suggested that Eq. (5.21) be used as a basis to design the controller in concert with Eq. (5.5); this approach will be equivalent to the approach used here for developing the RZS controller. Besides, it is suggested that the inclusion of acoustic energy sensing and vibration sensing in the control scheme will result in simultaneously controlling the structural vibrations and the noise levels over a larger space. These suggestions for future work will pave the way to the ultimate goal, which is implementation of these schemes in large-scale structural-acoustic systems, such as helicopter cabins and automobile cabins.

Appendix I. Numerical Values of Constants, Parameters, and Dimensions

In this appendix, the values of the different coefficients and parameters used in the model of Section 3.1 are presented. These values are used in generating the results shown in Chapter 3.

Air Medium

$$c_0 = 343 \text{ m/s}, \quad \rho_0 = 1.21 \text{ kg/m}^3$$

Enclosure Dimensions

$$L_{xc} = 24'', \quad L_{yc} = 18'', \quad L_{zc} = 20''$$

Plate Dimensions

$$L_{xp} = 26'', \quad L_{yp} = 20'', \quad h_p = 0.0625''$$

Aluminum Material Constants

$$E_p = 7.1 \times 10^{10} \text{ N/m}^2, \quad \rho_p = 2700 \text{ kg/m}^3, \quad \nu = 0.3$$

PZT Patch Dimensions

$$L_{xpzt} = 2'', \quad L_{ypzt} = 1'', \quad h_{pzt} = 0.0125''$$

PZT Constants

$$E_{pzt} = 10.5 \times 10^6 \text{ N/m}^2, \quad d_{31} = -247 \times 10^{-12} \text{ kg/m}^3$$

Data for Reference Microphone

$$x \text{ location} = L_{xc}/2, \quad y \text{ location} = L_{yc}/2, \quad z \text{ location} = L_{zc} + 20''$$

$$\text{Sensitivity} = 12.5 \times 10^{-3} \text{ V/Pa}$$

Speaker Data

$$x \text{ location} = 8.5'', \quad y \text{ location} = 10.0'', \quad z \text{ location} = 54.5''$$

$$\text{speaker diameter} = 14''$$

Other information, such as the sensitivities and locations of the reference and error microphones, are provided in Chapter 2.

Appendix II. Numerical Results

In this appendix, numerical results for the model developed in Section 3.1 are presented. (Please, refer to Eq. (3.70).) To generate these results, the number of the vibration modes is truncated to the first 17 modes, while number of the acoustic modes is truncated to the first three modes. The damping matrices are experimentally obtained.

$$\mathbf{M}_{cp} = \begin{bmatrix} 0 & 1.8502 & 0 \\ -1.2293 & 0 & 0 \\ 0 & 0 & -1.8014 \\ 0 & 0 & 0 \\ 0 & 0.8015 & 0 \\ 0 & 0 & -0.7804 \\ 0 & 0.7618 & 0 \\ -0.6324 & 0 & 0 \\ -0.5062 & 0 & 0 \\ 0 & 0 & 0 \\ 0 & 0.3300 & 0 \\ 0.0004 & 0.4948 & 0 \\ 0 & 0 & -0.8150 \\ 0 & 0 & 0 \\ -0.2604 & 0 & 0 \\ 0 & 0 & -0.4818 \\ 0 & 0 & -0.3530 \end{bmatrix}^T$$

$$\mathbf{K}_{pc} = \begin{bmatrix} 0 & -1.5291 & 0 \\ 1.0160 & 0 & 0 \\ 0 & 0 & 1.4888 \\ 0 & 0 & 0 \\ 0 & -0.6624 & 0 \\ 0 & 0 & 0.6499 \\ 0 & -0.6296 & 0 \\ 0.5226 & 0 & 0 \\ 0.4183 & 0 & 0 \\ 0 & 0 & 0 \\ 0 & -0.2727 & 0 \\ -0.0003 & -0.4090 & 0 \\ 0 & 0 & 0.6735 \\ 0 & 0 & 0 \\ 0.2152 & 0 & 0 \\ 0 & 0 & 0.3982 \\ 0 & 0 & 0.2918 \end{bmatrix}$$

$$\mathbf{K}_{pp} = \begin{bmatrix}
 0.293 & 0 & 0 & 0 & -0.005 & 0 & -0.005 & 0 \\
 0 & 0.092 & 0 & 0 & 0 & 0 & 0 & -0.088 \\
 0 & 0 & 0.153 & 0 & 0 & -0.019 & 0 & 0 \\
 0 & 0 & 0 & 0.263 & 0 & 0 & 0 & 0 \\
 -0.005 & 0 & 0 & 0 & 0.267 & 0 & 0.004 & 0 \\
 0 & 0 & -0.019 & 0 & 0 & 0.513 & 0 & 0 \\
 -0.005 & 0 & 0 & 0 & 0.004 & 0 & 0.528 & 0 \\
 0 & -0.088 & 0 & 0 & 0 & 0 & 0 & 0.651 \\
 0 & -0.019 & 0 & 0 & 0 & 0 & 0 & 0.007 \\
 0 & 0 & 0 & -0.033 & 0 & 0 & 0 & 0 \\
 0.004 & 0 & 0 & 0 & -0.040 & 0 & -0.040 & 0 \\
 -0.004 & 0 & 0 & 0 & -0.013 & 0 & 0.003 & 0 \\
 0 & 0 & -0.009 & 0 & 0 & 0.007 & 0 & 0 \\
 0 & 0 & 0 & -0.033 & 0 & 0 & 0 & 0 \\
 0 & 0.007 & 0 & 0 & 0 & 0 & 0 & -0.007 \\
 0 & 0 & -0.015 & 0 & 0 & -0.047 & 0 & 0 \\
 0 & 0 & 0.007 & 0 & 0 & -0.071 & 0 & 0 \\
 \\
 0 & 0 & 0.004 & -0.004 & 0 & 0 & 0 & 0 & 0 \\
 -0.019 & 0 & 0 & 0 & 0 & 0 & 0.007 & 0 & 0 \\
 0 & 0 & 0 & 0 & -0.009 & 0 & 0 & -0.015 & -0.007 \\
 0 & -0.033 & 0 & 0 & 0 & -0.033 & 0 & 0 & 0 \\
 0 & 0 & -0.040 & -0.0126 & 0 & 0 & 0 & 0 & 0 \\
 0 & 0 & 0 & 0 & 0.007 & 0 & 0 & -0.047 & -0.071 \\
 0 & 0 & -0.040 & 0.003 & 0 & 0 & 0 & 0 & 0 \\
 0.007 & 0 & 0 & 0 & 0 & 0 & -0.070 & 0 & 0 \\
 0.713 & 0 & 0 & 0 & 0 & 0 & -0.071 & 0 & 0 \\
 0 & 1.000 & 0 & 0 & 0 & 0.012 & 0 & 0 & 0 \\
 0 & 0 & 1.080 & 0.010 & 0 & 0 & 0 & 0 & 0 \\
 0 & 0 & 0.010 & 1.371 & 0 & 0 & 0 & 0 & 0 \\
 0 & 0 & 0 & 0 & 1.3789 & 0 & 0 & 0.006 & -0.070 \\
 0 & 0.012 & 0 & 0 & 0 & 1.6669 & 0 & 0 & 0 \\
 -0.071 & 0 & 0 & 0 & 0 & 0 & 1.728 & 0 & 0 \\
 0 & 0 & 0 & 0 & 0.006 & 0 & 0 & 1.851 & 0.018 \\
 0 & 0 & 0 & 0 & -0.070 & 0 & 0 & 0.018 & 2.195
 \end{bmatrix}$$

$$\mathbf{F}_V = \begin{bmatrix} 0.0034 & 0.0119 & 0.0034 & 0.0150 & 0.0382 & 0.0150 & 0.0034 \\ 0.0249 & 0 & -0.0249 & 0.0604 & 0 & -0.0604 & 0.0249 \\ 0.0355 & 0.0747 & 0.0355 & 0 & 0 & 0 & -0.0355 \\ 0.0909 & 0 & -0.0909 & 0 & 0 & 0 & -0.0909 \\ 0.0473 & -0.0539 & 0.0473 & 0.1006 & -0.1131 & 0.1006 & 0.0473 \\ 0.1250 & -0.1371 & 0.1250 & 0 & 0 & 0 & -0.1250 \\ 0.0710 & 0.1394 & 0.0710 & -0.0812 & -0.1582 & -0.0812 & 0.0710 \\ 0.0307 & 0 & -0.0307 & 0.0620 & 0 & -0.0620 & 0.0307 \\ 0.1479 & 0 & -0.1479 & -0.1655 & 0 & 0.1655 & 0.1479 \\ 0.0700 & 0 & -0.0700 & 0 & 0 & 0 & -0.0700 \\ 0.1761 & -0.1888 & 0.1761 & -0.1934 & 0.2067 & -0.1934 & 0.1761 \\ -0.0480 & 0.1220 & -0.0480 & -0.0932 & 0.2377 & -0.0932 & -0.0480 \\ 0.0474 & 0.0908 & 0.0474 & 0 & 0 & 0 & -0.0474 \\ 0.0911 & 0 & -0.0911 & 0 & 0 & 0 & -0.0911 \\ 0.0898 & 0 & -0.0898 & -0.0973 & 0 & 0.0973 & 0.0898 \\ -0.0969 & 0.2489 & -0.0969 & 0 & 0 & 0 & 0.0969 \\ 0.1007 & -0.1066 & 0.1007 & 0 & 0 & 0 & -0.1007 \end{bmatrix}$$

$$\begin{bmatrix} 0.0034 & 0.0119 & 0.0034 \\ 0.0249 & 0 & -0.0249 \\ -0.0355 & -0.0747 & -0.0355 \\ -0.0909 & 0 & 0.0909 \\ 0.0473 & -0.0539 & 0.0473 \\ -0.1250 & 0.1371 & -0.1250 \\ 0.0710 & 0.1394 & 0.0710 \\ 0.0307 & 0 & -0.0307 \\ 0.1479 & 0 & -0.1479 \\ -0.0700 & 0 & 0.0700 \\ 0.1761 & -0.1888 & 0.1761 \\ -0.0480 & 0.1220 & -0.0480 \\ -0.0474 & -0.0908 & -0.0474 \\ -0.0911 & 0 & 0.0911 \\ 0.0898 & 0 & -0.0898 \\ 0.0969 & -0.2489 & 0.0969 \\ -0.1007 & 0.1066 & -0.1007 \end{bmatrix}$$

$$\mathbf{M}_{pp} = \text{diag} (4.2862)_{17 \times 17}$$

$$\mathbf{M}_{cc} = \text{diag} (8.4999)_{3 \times 3}$$

$$\mathbf{K}_{cc} = \text{diag} (26.5589)_{3 \times 3}$$

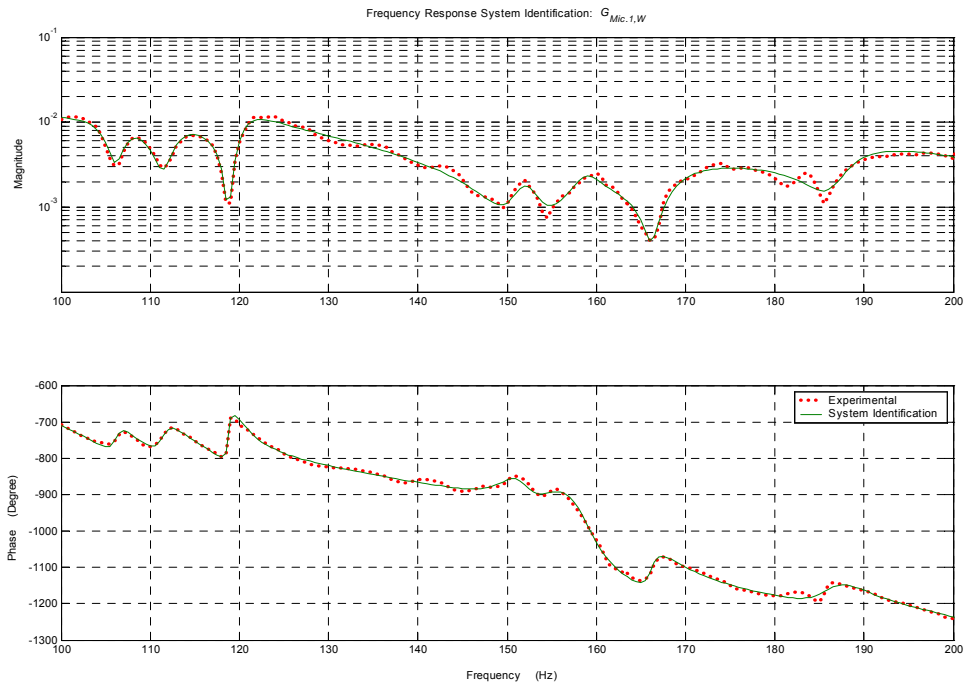
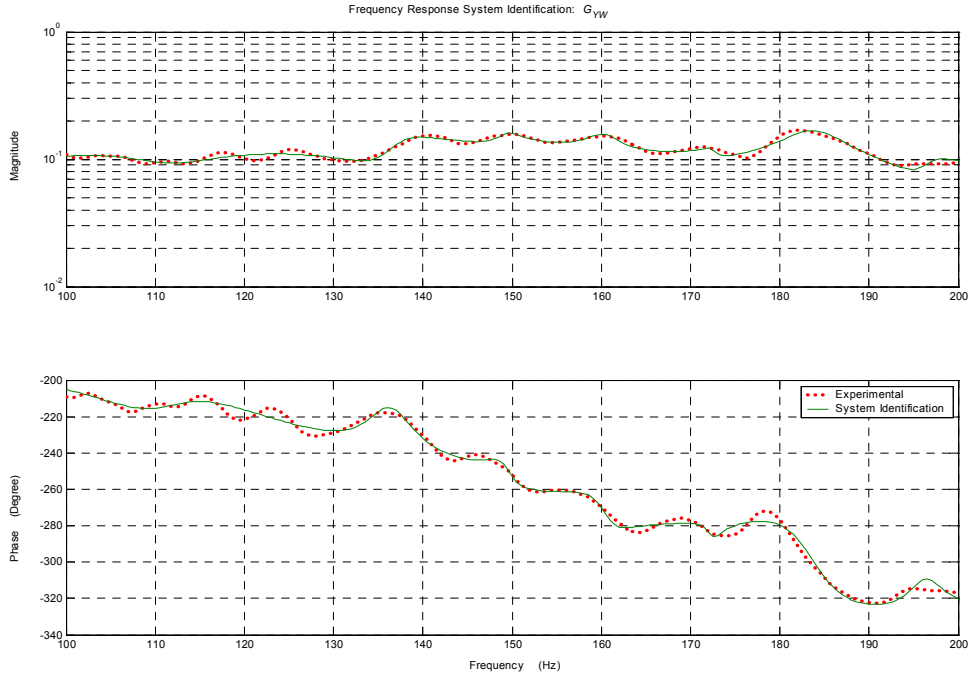
$$\mathbf{D}_{pp} = \text{diag} (\begin{matrix} 0.022 & 0.001 & 0.001 & 0.001 & 0.050 & 0.030 & 0.050 & 0.050 & 0.100 \\ & 0.050 & 0.050 & 0.040 & 0.001 & 0.001 & 0.001 & 0.001 & 0.001 \end{matrix})_{17 \times 17}$$

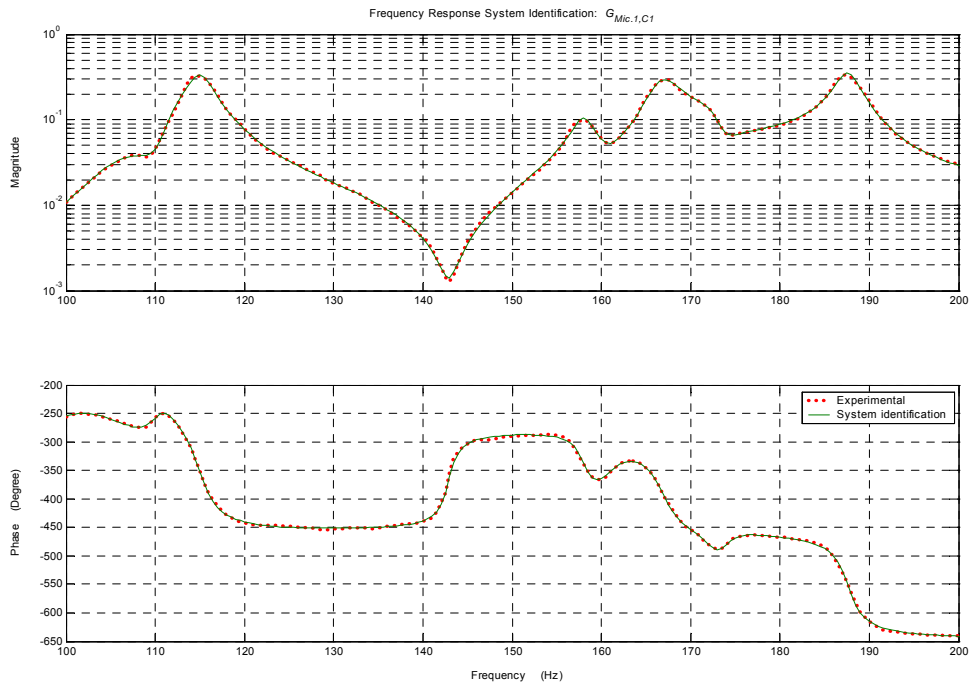
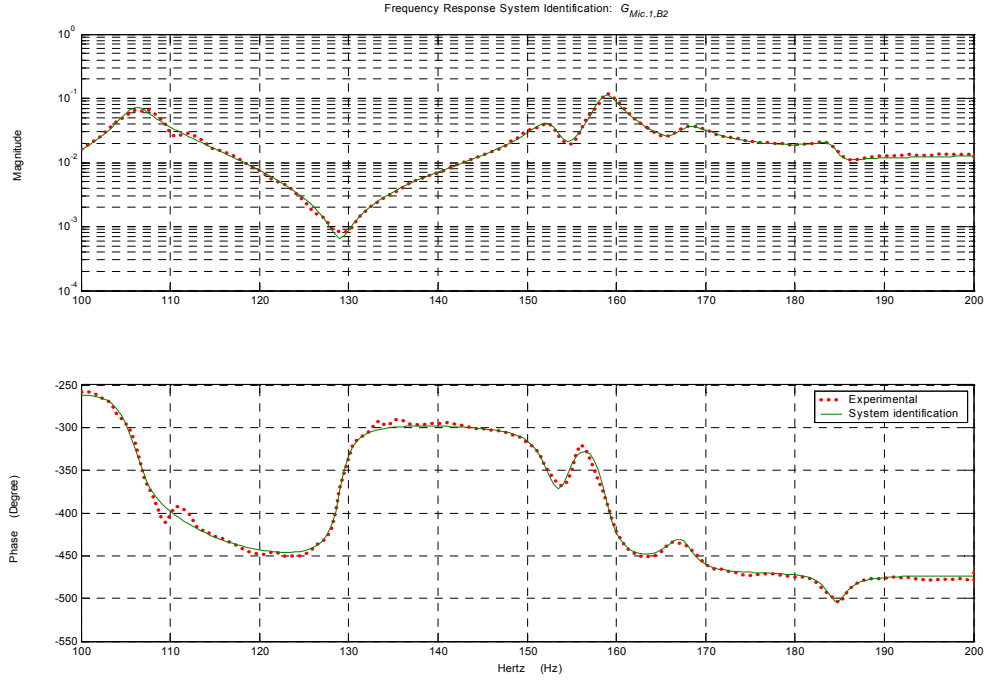
$$\mathbf{D}_{cc} = \text{diag} (0.001 \quad 0.200 \quad 0.006)_{3 \times 3}$$

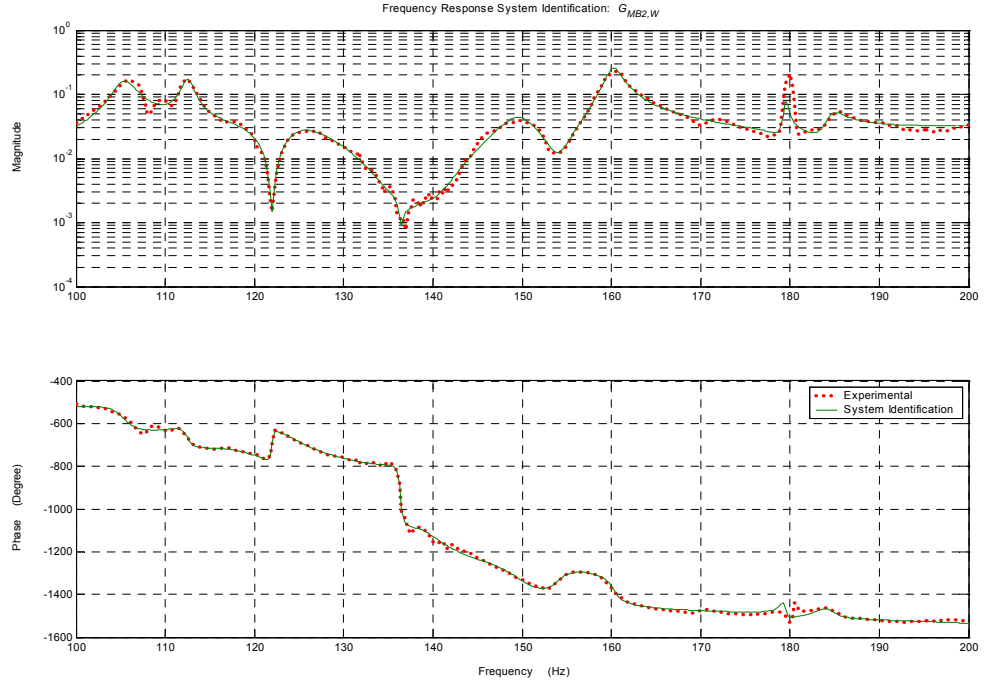
Appendix III. Frequency-Response Function

Comparisons

In this appendix, experimental frequency response measurements between the different actuators and sensors are compared with the predicted results of the experimentally identified model. For completeness, please refer to Figure 3.21 and Figure 5.8. The plots presented here and in these other two figures have a special importance, since they are directly related to the control efforts shown in Section 5.4.1.





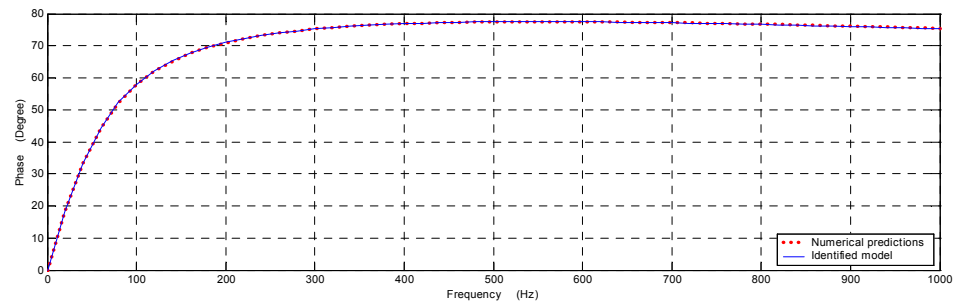
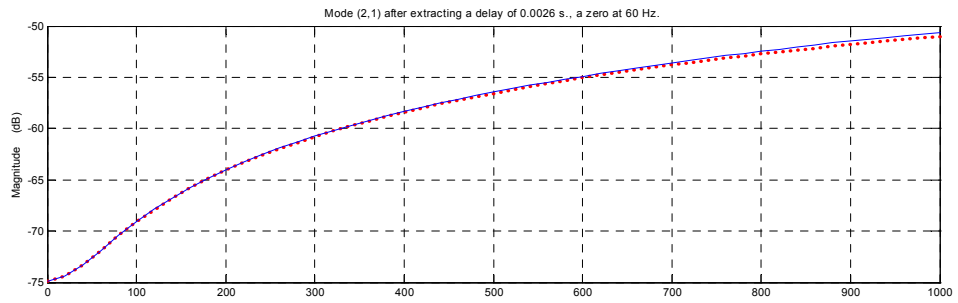
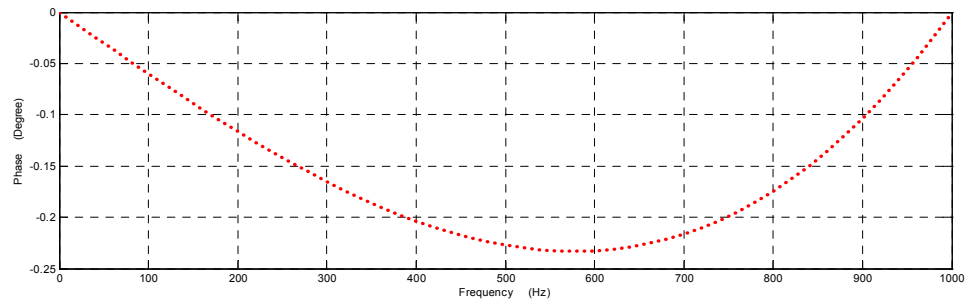
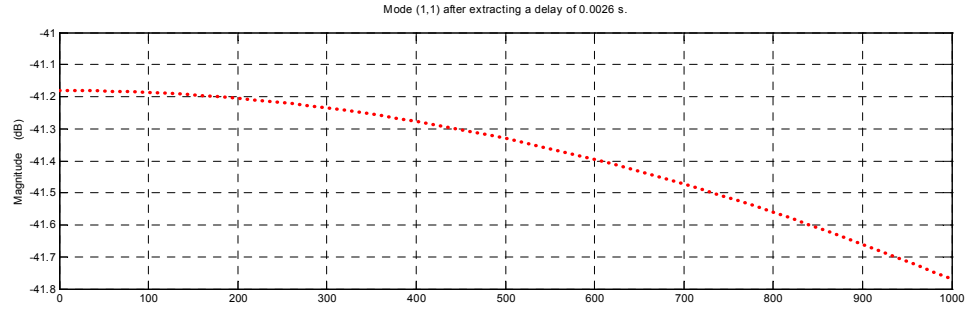


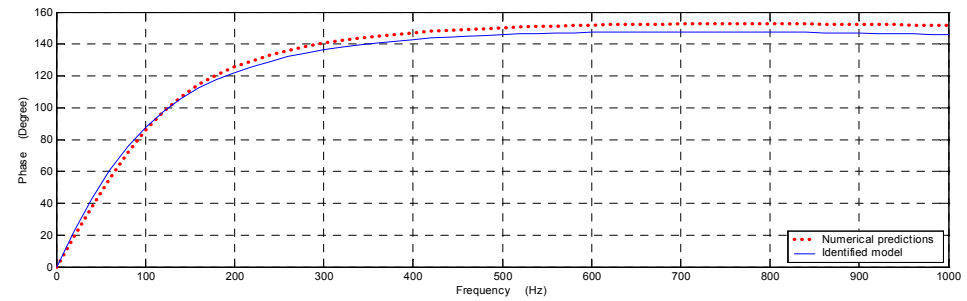
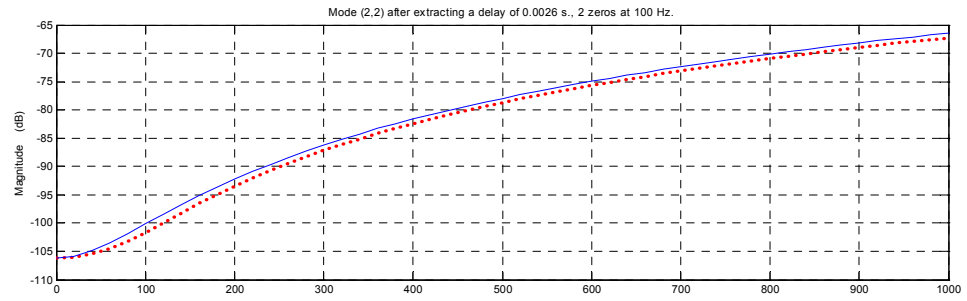
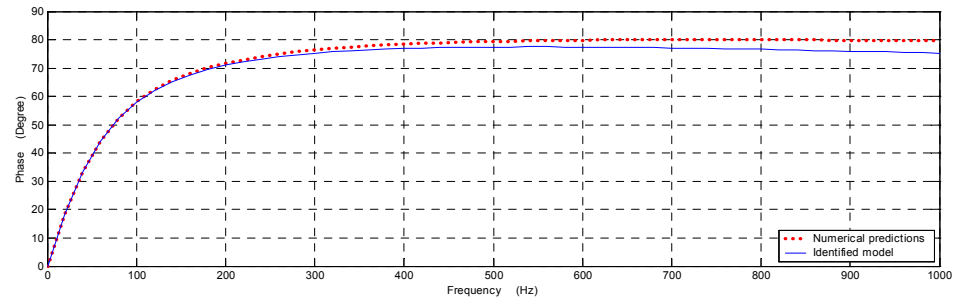
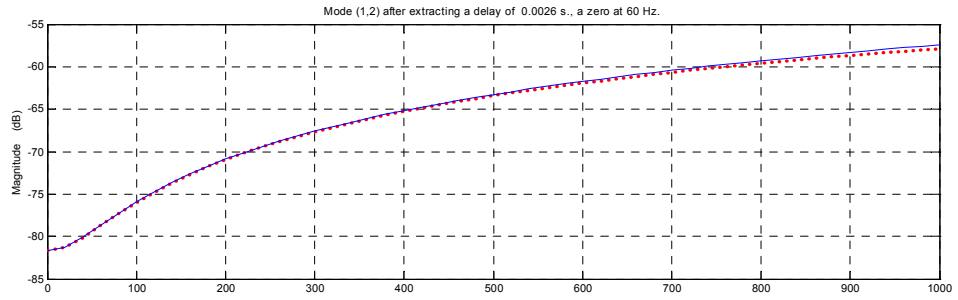
Appendix IV. Entries of \mathbf{F}_a

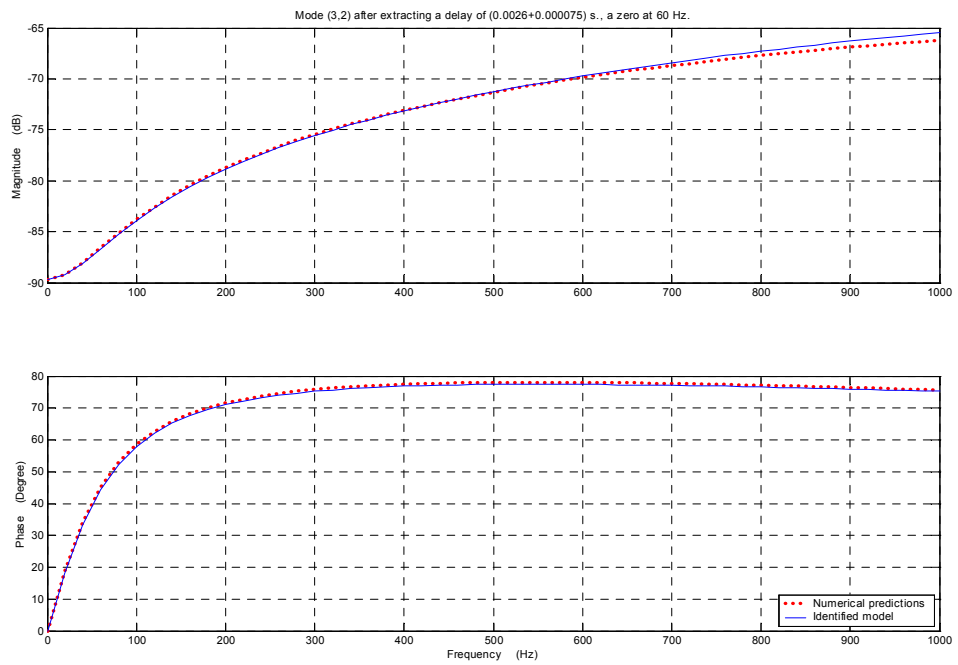
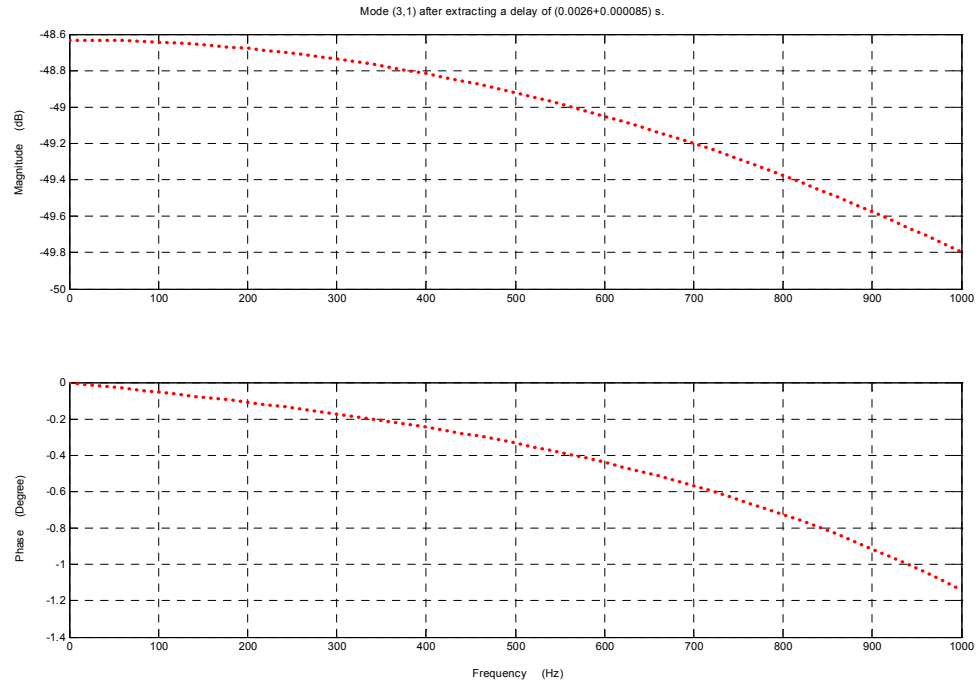
In this appendix, the frequency-dependent entries of the excitation vector matrix \mathbf{F}_a (please refer to Eq. (3.71)) that correspond to the first 17 vibration modes, compared with the analytically identified ones, are graphically presented. A pure time delay is first extracted from the phase response shown in each plot. The value of this time delay is indicated in the title of each figure. Besides, the title of each figure also shows the corresponding vibration mode and the pole(s) of the high-pass filter, if any.

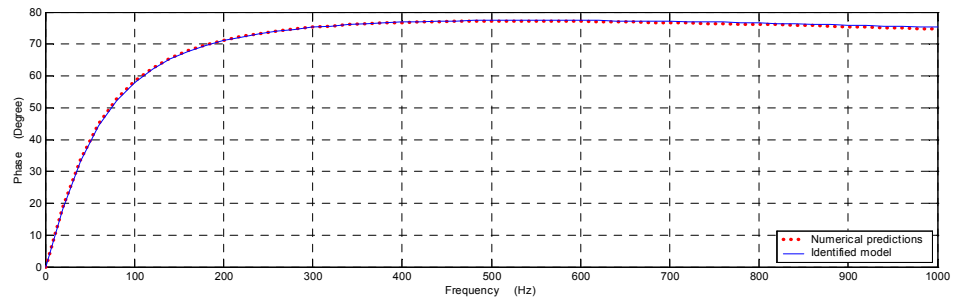
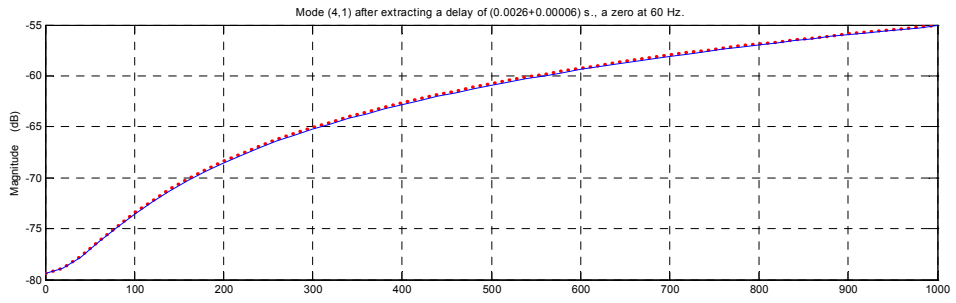
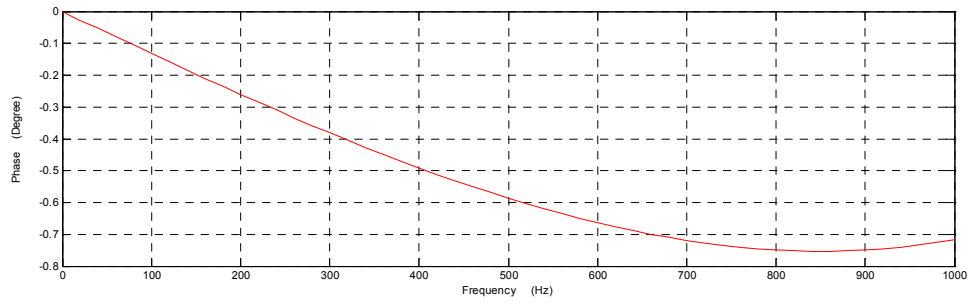
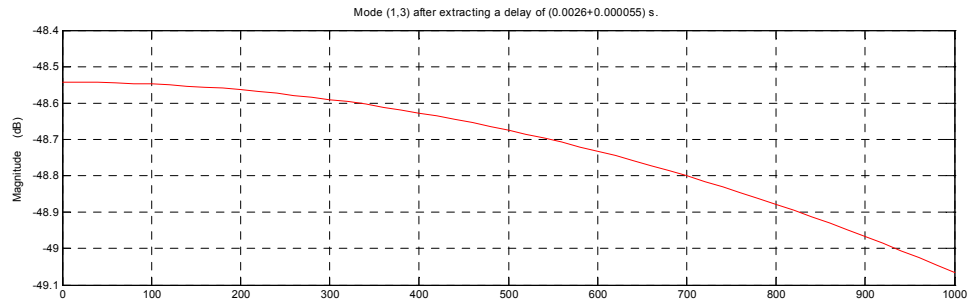
The following points are made based on the figures:

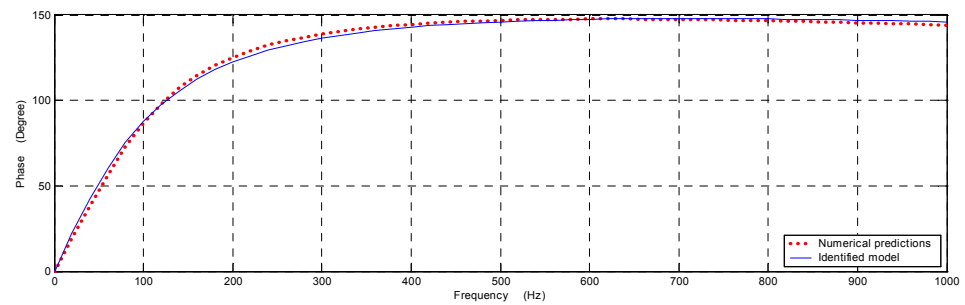
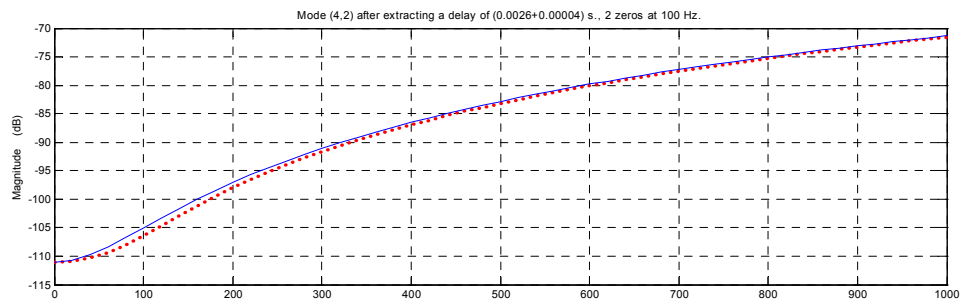
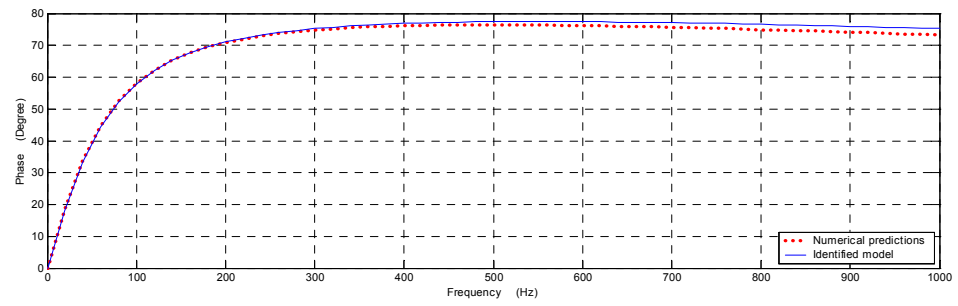
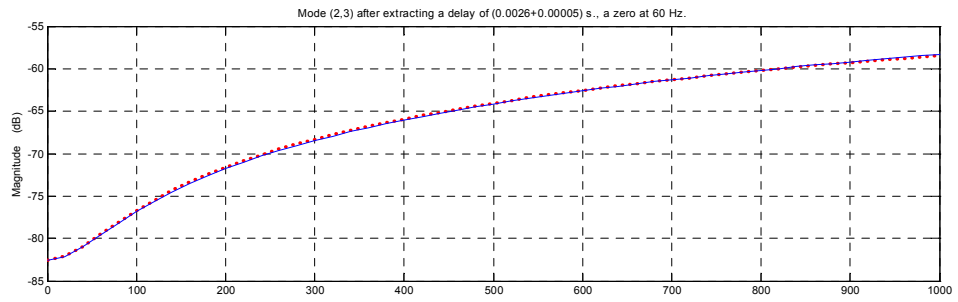
- For the low-frequency modes (up to the fourth mode), the phase delay does not change. For higher modes, the phase delay increases.
- For the odd \times odd modes, the corresponding entries of \mathbf{F}_a consist of pure delays. For odd \times even and even \times odd modes, first-order high pass filters are added, and for even \times even modes, second-order high pass filters are added.

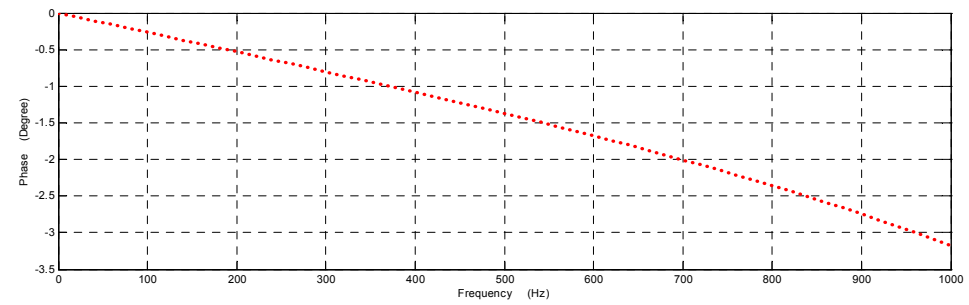
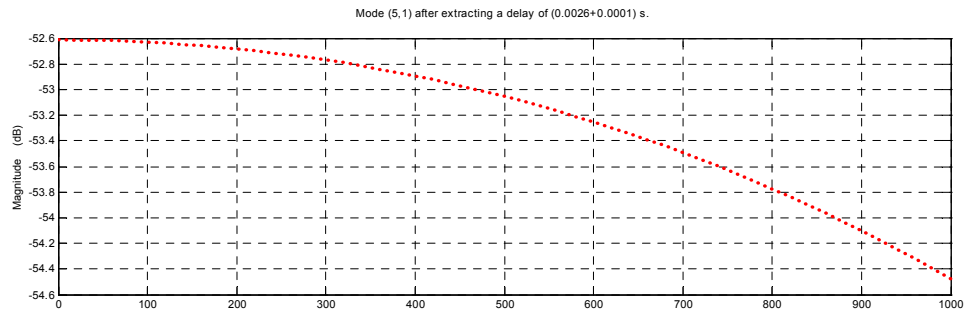
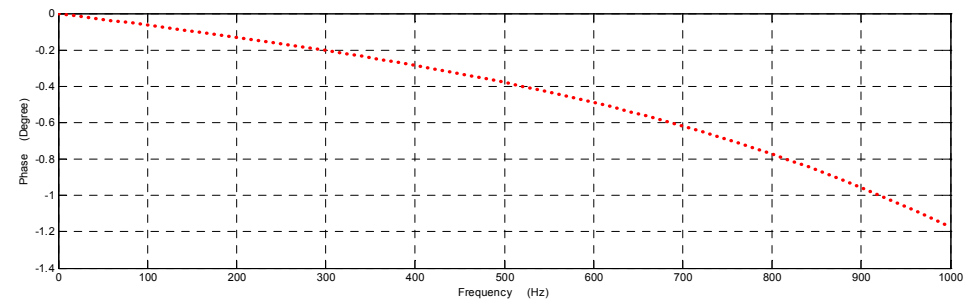
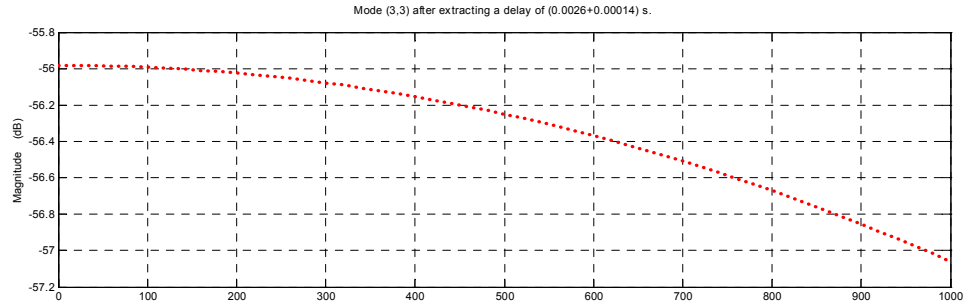


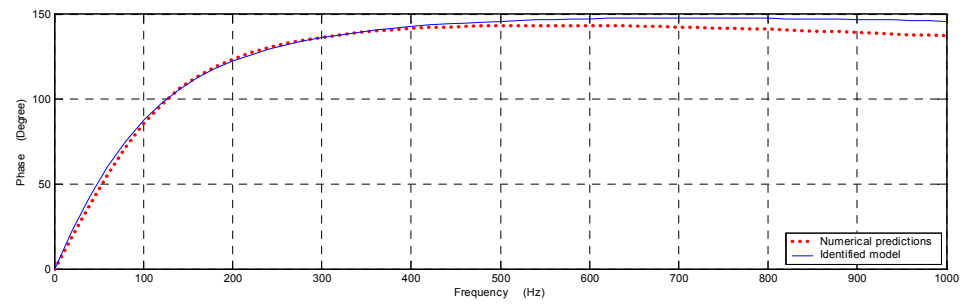
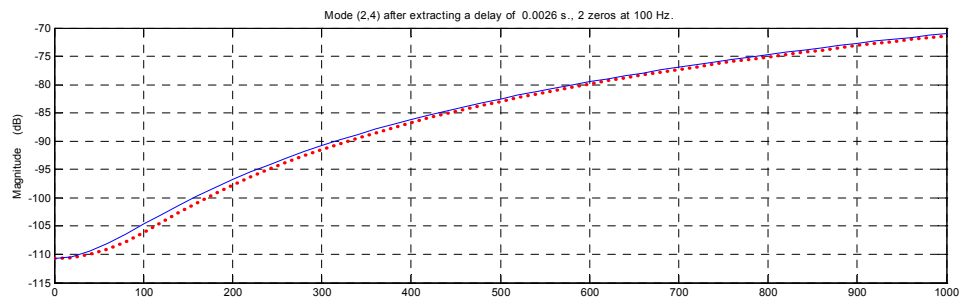
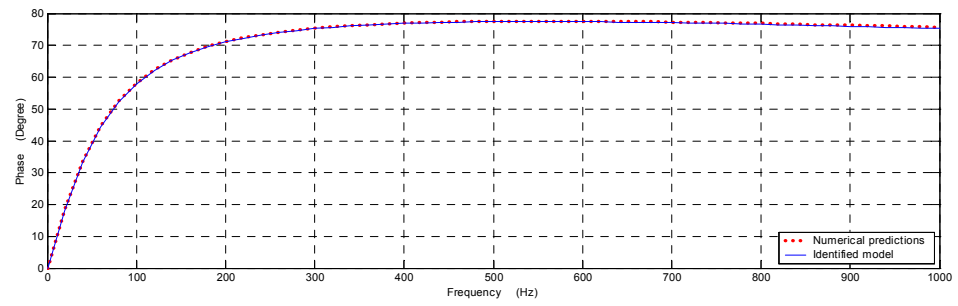
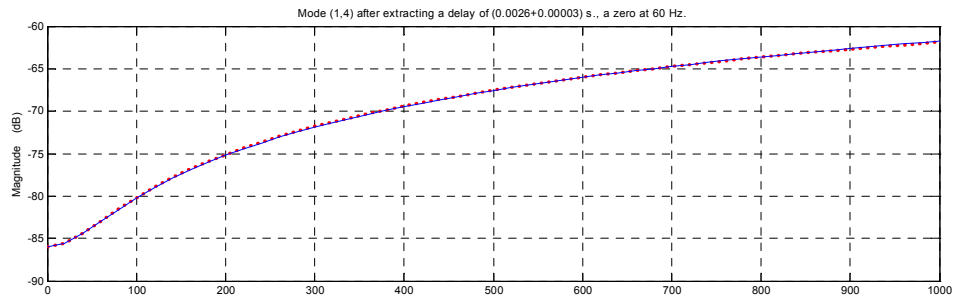


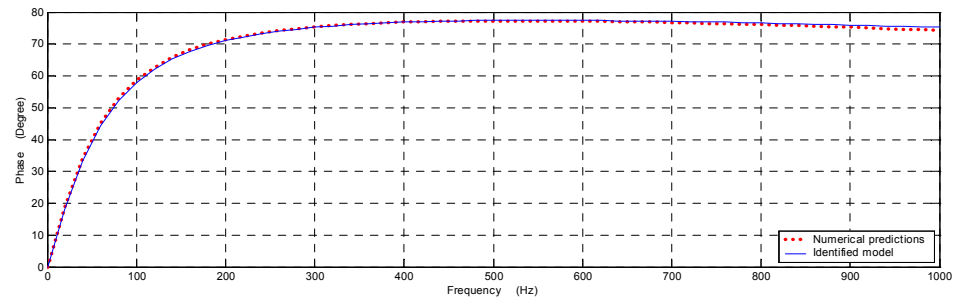
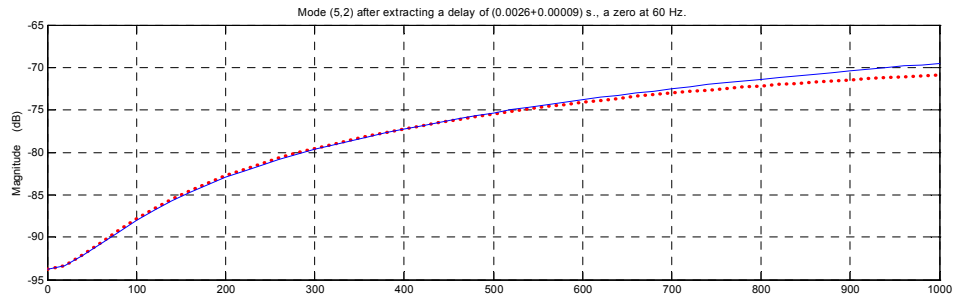
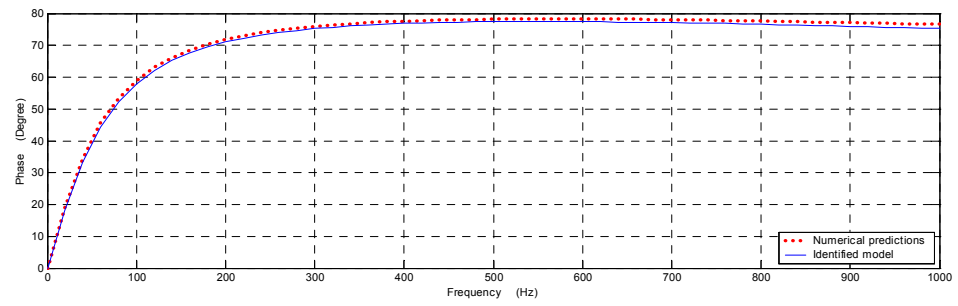
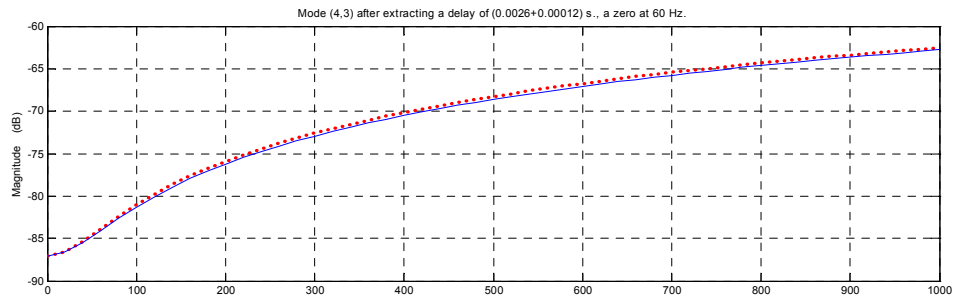


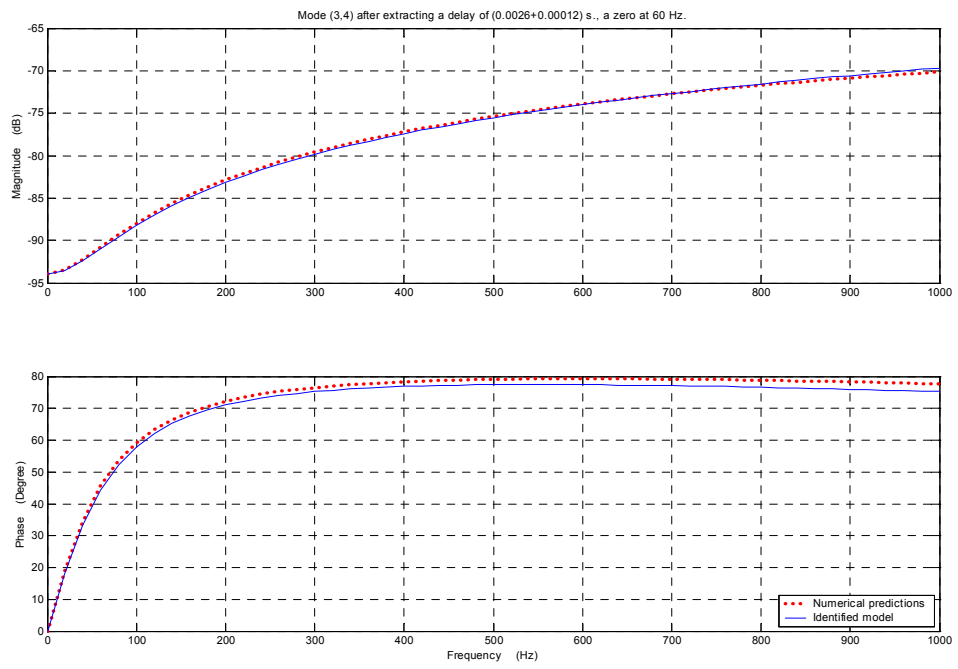












Appendix V. Experimental Results of PZT strain

In this appendix, the experimental results for the strain measurements of a PZT patch are tabulated. In these experiments, a strain gage was bonded to the surface of a free PZT patch to measure the surface strain while a DC voltage was input to the PZT patch quasi-statically from +0 to +120V and then from -0 to -120V. Analytical predictions are also tabulated in the following tables. Please, refer to Figure 3.10 for a picture showing the PZT patch with the strain sensor, and to Figure 3.11 for a graphical representation of the following tables.

Table V.1. Applied Positive (DC) Voltage and PZT free strain: Analytical predictions and experimental measurements.

<i>Positive Voltage</i>			
<i>Applied Voltage</i> (V)	<i>Bridge Output</i> (V)	<i>Experimental Strain</i> (in micro-strain)	<i>Analytical Predictions</i> (in micro-strain)
10.0	0.011	4.211	10.777
20.1	0.041	15.694	21.650
30.3	0.074	28.325	32.632
39.8	0.108	41.338	42.934
49.8	0.145	55.499	53.721
59.9	0.184	70.425	64.617
70.0	0.226	86.499	75.512
80.4	0.271	103.721	86.731
90.2	0.317	121.324	97.302
100.2	0.364	139.310	108.090
110.1	0.413	158.060	118.770
120.1	0.463	177.192	129.560

Table V.2. Applied Negative (DC) Voltage and PZT free strain:
Analytical predictions and experimental measurements.

<i>Negative Voltage</i>			
<i>Applied Voltage</i> (V)	<i>Bridge Output</i> (V)	<i>Experimental Strain</i> (in micro-strain)	<i>Analytical Predictions</i> (in micro-strain)
-10.3	-0.025	-9.56947	-11.12
-20.1	-0.051	-19.5219	-21.73
-30.0	-0.081	-31.0058	-32.38
-40.3	-0.113	-4.32555	-43.47
-50.2	-0.145	-55.5056	-54.15
-60.2	-0.18	-68.9045	-64.94
-70.0	-0.219	-83.8351	-75.51
-80.2	-0.26	-99.5319	-86.51
-90.0	-0.302	-115.612	-97.09
-100.0	-0.349	-133.607	-107.90
-110.3	-0.395	-151.220	-119.00
-120.0	-0.45	-172.280	-129.40

Appendix VI. Matlab Program Codes

In this appendix, matlab codes for panel and enclosure mode shapes and matrices and presented.

Enclosure.m

```
function [enclosuref,si,fi,gama,Mc,Kc]=enclosure(input_file,NPlots);
```

%This code calculates the mode shapes, natural frequencies, and stiffness and mass matrices of a CCCCCC rectangular enclosure. All data should be given in 'input_file.m'. Syntax is

```
% [enclosuref,si,fi,gama,Mp,Cp]=enclosure('input_file')
```

%where enclosuref is Nx7 symblic matrix whose 1st 3 columns are modal indices, 4rd column is resonance frequencies, and 5th thru 7th columns are mode shapes in x, y & z directions, respectively. N is the total number of modes, based on data given in 'input_file'. si, fi, and gama are (enclosureN,1) vector arrays whose entries are the x, y, and z functions of the enclosure mode shapes, respectively, where enclosureN is the

```

enclosuref = sorting(enclosuref);

enclosuref = enclosuref(2:size(enclosuref,1),:); %used to eliminate the rigid body mode

enclosuref = [enclosuref(:,1:3) - 1 , enclosuref(:,4)]; %corrects the indices to reflect the
                                                    zero indices

% * * * * * Mode Shapes * * * * *
temp = [0:enclosureN]'; %used for epselon

si = sqrt((sign(temp)+1)/Lxc).*cos(temp(:)*pi*x/Lxc);
fi = sqrt((sign(temp)+1)/Lyc).*cos(temp(:)*pi*y/Lyc);
gama = sqrt((sign(temp)+1)/Lzc).*cos(temp(:)*pi*z/Lzc);

%Now, the matrix enclosuref will also include [si,fi,gama] at columns [5,6,7]

enclosuref= [enclosuref si(enclosuref(:,1)+1) fi(enclosuref(:,2)+1)
gama(enclosuref(:,3)+1)];

% * * * * * Mode Shape Plots * * * * *

if NPlots > size(enclosuref,1)

    error('Number of plots > number of modes')

end

if NPlots ~= 0 & ~isempty(NPlots) & NPlots <= size(enclosuref,1)

    mode_plots(enclosuref,[5 6 7],NPlots,[Lxc Lyc Lzc]);

end

% * * * * * Mass & Stiffness Matrices * * * * *

Mc = 1/cair^2 * eye(size(enclosuref,1));

Kc = diag((subs(enclosuref(:,1))*pi/Lxc).^2 + ...

```

```
(subs(enclosuref(:,2))*pi/Lyc).^2 + ...
(subs(enclosuref(:,3))*pi/Lzc).^2);

% ***** End *****
```

Panel.m

```
function [panelf,alfa,beta,Mp,Kp]=panel(input_file,NPlots);

%This code calculates the mode shapes, natural frequencies, and stiffness and mass matrices of a
CCCC rectangular plate. All data should be given in 'input_file.m'. Syntax is

% [panelf,alfa,beta,Mp,Kp]=panel('input_file')

%where panelf is Nx5 symblic matrix whose 1st 2 columns are modal indices, 3rd column is
resonance frequencies, and 4th and 5th columns are mode shapes in x and y directions,
respectively. N is the total number of modes, based on data given in 'input_file'. alfa and beta
are (panelN,1) vector arrays whose entries are the x and y functions of the panel mode shapes,
respectively, where panelN is the number of modes in x and y directions as given in 'input_file'.
NPlots are the number of modes to be plotted. This number should be <= total number of
modes given in 'input_file'. It can be zero or [] to omit plotting. Mp and Kp are the mass and
stiffness matrices of the panel.

%For the values given in the section "Constants", please refer to Blevins, 1979, Formulas for
Natural Frequency and Mode Shapes.

%This code is made as part of Moustafa Al-Bassiyouni's PhD work at the Mechanical
Engineering, Univeristy of Maryland.

%Copyright © Moustafa Al-Bassiyouni, 1999-2004
```

```

eval(input_file);      %%calls the file of input data.

% ***** Initialization *****

alfa = [];   beta = [];

panelf = [];

syms x y

% ***** Constants *****

D = Ep * hp^3 / (12 * (1 - nu^2));

lamda1 = [4.73004074 7.85320462 10.9956079 14.1371655 17.2787597
          (2*[6:panelN^2]+1)*pi/2];

lamda2 = [0.982502215 1.000777312 0.99996645 1.000001450 0.999999937 ones(1,panelN^2-
          5)];

temp = [4:panelN^2];

G = [1.506 2.5 3.5 temp+0.5];

H = [1.248 4.658 10.02 (temp+0.5).^2.*(1-2./pi./(temp+0.5))];

lamda1 = lamda1(1:panelN);

lamda2 = lamda2(1:panelN);

G = G(1:panelN);

H = H(1:panelN);

% ***** Natural Frequencies *****

panelf = pi/2 * sqrt(D/(roh*hp))*(G'.^4 * ones(1,panelN) / Lxp^4 + ones(panelN,1)*G.^4 /
          Lyp^4 + 2 * H' * H / (Lxp^2 * Lyp^2));

%This matrix "panelf" contains the panel natural frequencies corresponding to the indices (i,j),
e.g. mode (3,2) has a natural frequency of panelf(3,2) Hz. Now, these frequencies are sorted

```

and rearranged in column vector, along with 2 other columns for x- and y- indices, for further use. For this reason, the code "sorting.m" is used.

```

panelf = sorting(panelf);

% * * * * * Mode Shapes * * * * *
alfa = ((cosh(lamda1/Lxp*x)-cos(lamda1/Lxp*x))/sqrt(Lxp) - lamda2.*(sinh(lamda1/Lxp*x)-
    sin(lamda1/Lxp*x))/sqrt(Lxp)).';

beta = ((cosh(lamda1/Lyp*y)-cos(lamda1/Lyp*y))/sqrt(Lyp) - lamda2.*(sinh(lamda1/Lyp*y)-
    sin(lamda1/Lyp*y))/sqrt(Lyp)).';

%Now, the matrix panelf will also include [alfa, beta] at columns [4,5]
panelf = [panelf  alfa(panelf(:,1))  beta(panelf(:,2))];

% * * * * * Mode Shape Plots * * * * *
if NPlots > size(panelf,1)
    error('Number of plots > number of modes')
end

if NPlots ~= 0 & ~isempty(NPlots) & NPlots <= size(panelf,1)
    mode_plots(panelf,[4 5],NPlots,[Lxp Lyp])
end

% * * * * * Mass & Stiffness Matrices * * * * *
Ix = diag((lamda1/Lxp).^4);
Iy = diag((lamda1/Lyp).^4);
temp1 = (2*lamda1.^2/Lxp^(2.5) .* (cos(lamda1.*x/Lxp) - ...
    lamda2.*sin(lamda1.*x/Lxp))).' * alfa.';
temp2 = (2*lamda1.^2/Lyp^(2.5) .* (cos(lamda1.*y/Lyp) - ...

```

```

lamda2.*sin(lamda1.*y/Lyp)).' * beta.>';
Ixx = symmetric(sqrt(Ix) + integrate(temp1,0,Lxp,Lxp/50));
Iyy = symmetric(sqrt(Iy) + integrate(temp2,0,Lyp,Lyp/50));

Mp = rohp * hp * eye(size(panelf,1));
Kp = 2*D * Ixx(subs(panelf(:,1)),subs(panelf(:,1))) * Iyy(subs(panelf(:,2)),subs(panelf(:,2))) + D
    * (diag(lamda1(subs(panelf(:,1))))/Lxp).^4 + diag(lamda1(subs(panelf(:,2))))/Lyp).^4);

% ***** End *****

```

Sorting.m

```
function f1=sorting(f);
```

%This code generates an array f1 whose dimensions are $M^N \times (N+1)$ where M and N are size and dimension of the square or cubic matrix f, respectively. The last column in f1 contains the entries of f sorted in accending order whereas the entries of the first N columns are the corresponding indices obtained from f.

%This code is made as part of Moustafa Al-Bassyiouni's PhD work at the Mechanical Engineering, Univeristy of Maryland.

%Copyright © Moustafa Al-Bassyiouni, 1999-2004

```
L = size(f);
```

```
N = length(L);
```

```
M = L(1);      %since f is square, all entries of L are equal.
```

```
switch N
case 1
    temp = [1:M]';
case 2
    temp = [repmat([1:M]',M,1) , reshape(repmat([1:M],M,1),M^2,1)];
case 3
    temp = [repmat([1:M]',M^2,1) , ...
            repmat(reshape(repmat([1:M],M,1),M^2,1),M,1) , ...
            reshape(repmat([1:M],M^2,1),M^3,1)];
otherwise
    error('This function handles only up to 3D systems')
end
f1 = [temp,reshape(f,M^N,1)];
f1 = sortrows(f1,N+1);

% ***** End *****
```

References

- M. Ahmadian, K. Jeric, and D. Inman, “An experimental evaluation of smart damping materials for reducing structural noise and vibrations,” *Transactions of the ASME Journal of Vibration and Acoustics*, Vol. 123, No. 4, pp. 533-535, October 2001.
- M. Arafa, *Vibration and Noise Control using Active Piezoelectric Damping Composites*, Ph.D. Dissertation, University of Maryland, College Park, 2002.
- M. Bai and Z. Lin, “Active noise cancellation for a three-dimensional enclosure by using multiple-channel adaptive control and H_∞ control,” *Transactions of the ASME Journal of Vibration and Acoustics*, Vol. 120, No. 4, pp. 958-964, October 1998.
- M. Al-Bassyouni and B. Balachandran, “Zero spillover control of enclosed sound fields,” *SPIE's 8th Annual International Symposium on Smart Structures and Materials*, Newport Beach, CA., March 4-8, Vol. 4362, Paper No. 4326-7, 2001.

References

- M. Al-Bassyiouni and B. Balachandran, “Experimental Studies of Zero Spillover Scheme for Active Structural-acoustic Control Systems,” Proceedings of the 12th International Conference on Adaptive Structures and Technologies (ICAST), University of Maryland, College Park, MD., October 15-17, 2001.
- M. Al-Bassyiouni and B. Balachandran, “Sound transmission through a flexible panel into an enclosure: structural-acoustics model,” submitted to the *Journal of Sound and Vibration*, 2003.
- M. Al-Bassyiouni and B. Balachandran, “Control of enclosed sound fields using zero spillover schemes,” submitted to the *Journal of the Acoustical Society of America*, 2004.
- M. Al-Bassyiouni, *Studies in Modeling and Control of a Flexible Robot Arm*, Masters thesis, Cairo University, Giza, Egypt, 1998
- B. Balachandran, A. Sampath, and J. Park, “Active control of interior noise in a three-dimensional enclosure,” *Smart Materials and Structures*, Vol. 5, pp. 89-97, 1996.
- B. Balachandran and M.- X. Zhao, “Actuator nonlinearities in interior acoustics control,” *Proceedings of the SPIE 2000 Symposium on Smart Structures and Materials*, Newport Beach, CA, March 5-9, Vol. 3984, Paper No. 3984-13, 2000.
- T. Beauvilain, J. Bolton, and B. Gardner, “Sound cancellation by the use of secondary multipoles: Experiments,” the *Journal of the Acoustical Society of America*, Vol. 107, No. 3, pp. 1189-1202, March 2000.

References

- J. Blevins, *Formulas for Natural Frequency and Mode Shapes*, Van Nostrand Reinhold Company, 1979, Section 11.3, pp. 252-274.
- L. Beranek, *Acoustics*, 5th Edition, the Acoustical Society of America, New York, 1996.
- D.-M. Chiang and W.-H. Chen, “A combined FEM an BEM approach for sound radiation with finite flange,” *Journal of Vibration and Control*, Vol. 6, pp. 571-587, 2000.
- L. Chang and J. Nicolas, “Radiation of sound into a cylindrical enclosure from a point-driven end plate with general boundary conditions,” *Journal of the Acoustical Society of America*, Vol. 91, pp. 1504–1513, 1992.
- B. Chapnik and I. Currie, “Noise reduction using finite-length flexible segments,” *ASME Journal of Vibration and Acoustics*, Vol. 122, No. 2, pp 94-108, April 2000.
- I. Chopra, *Smart Structures Theory*, ENAE651 class notes, University of Maryland, Sept. 2000.
- E. Dowell and H. Voss, “The effect of a cavity on panel vibration,” *AIAA*, Vol. 1, pp. 476-477, 1963.
- S. J. Elliott, “Down with noise: practical control systems for combatting audible noise show up in aerospace, general aviation, and military roles,” *IEEE spectrum*, pp. 54-61, June 1999

References

- C. R. Fuller and A. H. Von Flotow, "Active control of sound and vibration," *IEEE Control systems*, pp. 9-19, Dec. 1995.
- H. Geng, Z. Roa, and Z. Han, "New modeling method and mechanism analyses for active control of interior noise in an irregular enclosure using piezoelectric actuators," *Journal of the Acoustical Society of America*, Vol. 113, pp. 1439-1454, 2003.
- G. Gibbs, R. Clark, D. Cox, and J. Vipperman, "Radiation model expansion" Application to active structural acoustic control," *Journal of the Acoustical Society of America*, Vol. 107, No. 1, pp. 332-339, 2000.
- R. Guy, "The steady state transmission of sound at normal and oblique incidence through a thin panel backed by a rectangular room – A multi-modal analysis," *Acustica*, Vol. 43, pp. 295-304, 1979.
- L. Heck, J. Olkin, and K. Naghshineh, "Transducer placement for broadband active vibration control using a novel multidimensional QR factorization," *Transactions of the ASME, Journal of Vibration and Acoustics*, Vol. 120, No. 3, pp. 663-670, July 1998.
- I. Helszajn, *Synthesis of Lumped Element, Distributed and Planar Filters*, McGraw-Hill, London, Cambridge, 1990.
- M. Hernandez, *Advances in Acoustics Technology*, Wiley, New York, 1995.

References

- J. Hong and D. S. Bernstein, “Bode integral constraints, colocation, and spillover in active noise and vibration control,” *IEEE Transaction on Control Systems Technology*, Vol. 6, No. 1, January 1998.
- J.-S. Hong, K. Shin, C.-H. Lee, and J.-E. Oh, “Active control of radiated sound from a vibrating plate,” *Proceedings of ASME DETC’01*, Pittsburgh, PA, September 9-12, 2001.
- Y. Huang and C. Fuller, “Vibration and noise control of the fuselage via dynamic absorbers,” *Transactions of the ASME, Journal of Vibration and Acoustics*, Vol. 120, No. 2, pp. 496-502, April 1998.
- J. M. Jessel and G. A. Mangiante, “Active Sound Absorbers in an Air Duct,” *Journal of Sound and Vibration*, Vol. 27, no. 3, 1972.
- R. Jolly, D. J. Rossetti, and S. C. Southward “Actuator Redundancy in Adaptive Control Systems,” *Active Control of vibration and Noise*, Vol. 75, ASME 1994.
- C. D. Kestell, B. S. Cazzolato, and C. H. Hansen, “Active noise control in a free field with virtual sensors,” *Journal of the Acoustical Society of America*, Vol. 109, No. 1, pp. 232-243, January 2001.
- S.-M. Kim and M. J. Brennan, “A compact matrix formulation using the impedance and mobility approach for the analysis of structural-acoustic systems,” *Journal of Sound and Vibration*, Vol. 223, pp. 79–113, 1999.

References

- S.-M. Kim and M. J. Brennan, “Active control of harmonic sound transmission into an acoustic enclosure using both structural and acoustic actuators,” *Journal of the Acoustical Society of America*, Vol. 107, pp. 2523–2534, 2000.
- S.-M. Kim and Y.-H. Kim, “Structural-acoustic coupling in a partially opened plate-cavity system: Experimental observation by using nearfield acoustic holography,” *Journal of the Acoustical Society of America*, Vol. 109, pp. 65-74, 2001.
- L. E. Kinsler and A. R. Frey, *Fundamentals of Acoustics*, Second Edition, John Wiley & Sons, Inc., New York, 1962.
- H. Kuttruff, *Room Acoustics*, 2nd Edition, New York, 1981.
- S. K. Lau and S. K. Tang, “Impacts of structural–acoustic coupling on the performance of energy density-based active sound transmission control,” *Journal of Sound and Vibration*, Vol. 266, pp. 147-170, 2003.
- P. Lueg, “Process of silencing sound oscillations,” US. Patent No. 2,043,416, 1936.
- R. Lyon, “New reduction of rectangular enclosures with one flexible wall,” *Journal of the Acoustical Society of America*, Vol. 35, pp. 1791-1797, 1963.
- Morgan Electro Ceramics, Inc., Bedford, Ohio,
www.morganelectroceramics.com.
- L. Munjal, *Acoustics of Ducts and Mufflers*, Wiley, New York, 1987.

References

- A. Nashif, D. Jones, and J. Henderson, *Vibration damping*, John Wiley & Sons, Inc., New York, 1985.
- D. Nefske, J. Wolf, and L. Howell, “Structural-acoustic finite element analysis of the automobile passenger compartment: A review of current practice,” *Journal of Sound and Vibration*, Vol. 80, pp. 247-266, 1982.
- A. Nelson and S. J. Elliott, *Active Control of Sound*, Academic Press, London, 1992.
- H. Olson and E. May, “Electronic sound absorber,” *Journal of the Acoustical Society of America*, Vol. 25, pp. 1130-1136, 1953.
- J. Parkins, *Active Minimization of Energy Density in a Three-Dimensional Enclosure*, Ph.D. Dissertation, Pennsylvania State university, 1998.
- J. Parkins, S. Sommerfeldt, and J. Tichy, “Narrowband and broadband active control in an enclosure using the acoustic energy density,” *Journal of the Acoustical Society of America*, Vol. 108, No. 1, pp. 192-203, July 2000.
- D. Pierce, *Acoustics: an Introduction to its Physical Principles and Applications*, Acoustical Society of America, Woodbury, New York, 1989.
- J. Ro and A. Baz, “Control of Sound Radiation from a Plate into an Acoustic Cavity using Active Constrained Layer Damping,” *Smart Materials and Structures*, Vol. 8, 1999.

References

- A. Roure, “Self-adaptive broadband active sound control systems,” *Journal of Sound and Vibration*, Vol. 101, pp. 429-441, 1985.
- A. Sampath, *Schemes for Noise Control in Three-Dimensional Enclosures*, Ph.D. thesis, University of Maryland, College Park, MD, 1997.
- A. Sampath and B. Balachandran, “Active interior acoustics control of bandlimited disturbances,” *Proceedings of the SPIE 1997 North American Conference on Smart Structures and Material*, San Diego, California, March 3-6, 1997.
- A. Sampath and B. Balachandran, “Active control of multiple tones in an enclosure,” *Journal of the Acoustical Society of America*, Vol. 106, No. 1, pp. 211-225, July 1999.
- R. Sánchez-Peña and M. Sznaier, *Robust System: Theory and Applications*, John Wiley & Sons, Inc., NY. 1998
- W. Soedel, *Vibrations of Shells and Plates*, Marcel Dekker, Inc., New York and Basel, 1981.
- J. Sun and S. Hirsch, “Numerical Studies of Acoustic Boundary Control for Interior Sound Suppression,” *Journal of the Acoustical Society of America*, Vol. 104, No. 4, October 1998.
- United States Patent and Trademark Office, <http://www.uspto.gov>.

References

- D. Wang and M. Vidyasagar, "Transfer functions for a single flexible link," *IEEE International Conference of Robotics and Automation*, Scottsdale, AZ, 1989.
- D.-B. Yoon and Y.-H. Kim, "Control performance and robustness of an active noise control system for uncertain primary sound fields," *Journal of the Acoustical Society of America*, Vol. 107, No. 6, pp. 3226-3234, June 2000.
- J. Yuan, "A relaxed condition for perfect cancellation of broadband noise in 3D enclosures," *Journal of the Acoustical Society of America*, Vol. 107, No. 6, pp. 3235-3244, June 2000.
- S. Yi, S. Ling, and M. Ying, "Time-domain analysis of acoustics-structure interactions for piezoelectric transducers," *Journal of the Acoustical Society of America*, Vol. 109, No. 6, pp.2762-2770, June 2001.

